Thèse n° 8008

Computational Modeling of the Oxygen Evolution Reaction at Semiconductor-Water Interfaces: A Path Towards Breaking Linear Scaling Relationships

Présentée le 2 octobre 2020

à la Faculté des sciences de base
Chaire de simulation à l’échelle atomique
Programme doctoral en physique

pour l’obtention du grade de Docteur ès Sciences

par

Patrick GONO

Acceptée sur proposition du jury

Prof. F. Mila, président du jury
Prof. A. Pasquarello, directeur de thèse
Prof. C. Di Valentin, rapporteuse
Prof. K. Laasonen, rapporteur
Prof. C. Corminboeuf, rapporteuse

École
polytechnique
fédérale
de Lausanne

2020

Acknowledgements

I must begin by thanking my supervisor, Alfredo Pasquarello, for giving me this opportunity in the first place, and for offering guidance and support along the way. He is one of the finest scientists I've had the luck to work with, and his immense attention to detail, as well as his untiring pursuit of understanding, were instrumental on my journey of becoming a researcher of my own.

In the same breath, I need to acknowledge my colleagues and my friends, who have in immeasurably many ways shaped the last four years of my life. Some of them have supported me since before my time at EPFL, some I've only had the pleasure to meet here. Some friendships will hopefully stand the test of the time. Nothing is truly permanent; and yet, I will always treasure the good times spent in the company of every single one of you.

Last but not least, I must express the infinite gratitude I feel towards my parents, and my brother and sister, who have stood by me since the very beginning. Without them, all this would have no meaning. If there is a single word from this work I'd like them to read, it is this: Ďakujem.

Lausanne, May 2020 Patrick Gono

Abstract

Photoelectrochemical water splitting is a promising source of clean, renewable fuel in the form of hydrogen. Despite extensive research endeavors, the widespread adoption of this technology is impeded due to suboptimal catalysts for the oxygen evolution reaction (OER) taking place on the anode. Studies have shown that linear scaling relationships exist between the binding energies of the OER intermediates. These relationships are responsible for the emergence of an overpotential which limits the catalytic efficiency of electrochemical cells. This work is devoted to the study of the OER, the emergence of linear scaling relationships, and possible avenues for overcoming them. We employ a selection of *ab-initio* computational free energy methods based on density functional theory in order to investigate the OER at atomistic model semiconductor interfaces.

An approach based on thermodynamic integration and *ab-initio* molecular dynamics simulations is used to isolate the effect of the solvent on the OER free energy steps. The observed effect is twofold. First, the presence of explicit water affects the equilibrium configurations of the reaction intermediates. Second, explicit water modifies the OER free energy steps by up to 0.5 eV. This effect is rationalized in terms of electrostatic interactions at the interface. Next, we verify the existence of the linear scaling relationships across a set of semiconductor and metal interfaces. We establish the robustness of the scaling relationships with respect to the adopted energy functional. Two potential approaches of breaking the linear scaling are considered.

First, a bifunctional mechanism that involves two close but functionally different active sites is investigated. The performance of the proposed mechanism is studied on a set of model interfaces, and the results indicate that specific combinations of catalysts may overcome the limitations imposed by the linear scaling relationship. We were able to establish general trends governing the efficiency of the bifunctional mechanism. In particular, a correlation between the valence band maximum and the hydrogen binding energy may be used as a descriptor in future searches for suitable hydrogen acceptors within the bifunctional scheme. Next, a detailed study of NiOOH/FeOOH catalysts identifies features most favorable to the bifunctional mechanism. Overpotentials as low as 0.13 eV are found for specific configurations. These results support the bifunctional mechanism as a means to break the linear scaling relationships.

Second, hole polarons at the TiO_2 surface induced by electronegative adsorbates in the OER intermediates are studied. The computational hydrogen electrode method in conjunction with a hybrid density functional is employed to quantify the effect of the surface polarons on the OER free energy steps. We find that the hole bipolarons reduce the overpotential of the reaction-determining step leading to good agreement with experiment. The stability of the polarons is further confirmed at the hydrated surface through a free energy study involving the explicit treatment of the solvent. Finally, the polaron energy level is aligned with respect to the redox levels in water to better understand the role of the polarons in the OER. Since the occurrence of surface hole polarons is unrelated to the scaling relationships, it offers an additional handle in the search for improved catalysts.

Key words: oxygen evolution reaction, OER, bifunctional mechanism, free energy, overpotential, linear scaling relationships, polarons, solvent effect

Zusammenfassung

Die photoelektrochemische Wasserspaltung ist eine vielversprechende Quelle für saubere, erneuerbare Brennstoffe in Form von Wasserstoff. Trotz umfangreicher Forschungsanstrengungen wird die breite Anwendung dieser Technologie durch suboptimale Katalysatoren für die an der Anode stattfindende Reaktion zur Sauerstofferzeugung (engl. „oxygen evolution reaction", OER) behindert. Studien haben gezeigt, dass lineare Skalierungsbeziehungen zwischen den Bindungsenergien der OER-Zwischenprodukte bestehen. Diese Beziehungen sind für das Entstehen eines Überpotentials verantwortlich, das die katalytische Effizienz der elektrochemischen Zellen begrenzt. Diese Arbeit widmet sich der Untersuchung der OER, der Entstehung von linearen Skalierungsbeziehungen und möglichen Wegen zu deren Überwindung. Wir verwenden eine Auswahl von ab-initio Computermethoden basierend auf Dichtefunktionaltheorie basierenden, um die OER an atomistischen Modell-Halbleitergrenzflächen zu untersuchen.

Ein Ansatz, der auf thermodynamischer Integration und ab-initio Molekulardynamiksimulationen basiert, wird verwendet, um die Wirkung des Lösungsmittels auf die Gibbs-Energie-Differenzen der OER zu isolieren. Wir beobachten hierbei zwei Effekte. Erstens beeinflusst das Wasser die Konfigurationen der Reaktionszwischenprodukte. Zweitens modifiziert explizites Wasser die Gibbs-Energie-Differenzen der OER um bis zu 0,5 eV. Dieser Effekt wird im Hinblick auf elektrostatische Wechselwirkungen an der Grenzfläche rationalisiert. Als nächstes verifizieren wir die Existenz der linearen Skalierungsbeziehungen über einen Satz von Halbleiter- und Metalloberflächen. Wir stellen die Robustheit der Skalierungsbeziehungen in Bezug auf das angenommene Energiefunktional fest. Es werden zwei mögliche Ansätze zum Aufbrechen der linearen Skalierung betrachtet.

Erstens wird ein bifunktionaler Reaktionsmechanismus untersucht, der zwei nahe beieinander liegende, aber funktionell unterschiedliche aktive Zentren umfasst. Die Leistung des vorgeschlagenen Mechanismus wird an einer Reihe von Modelloberflächen untersucht. Die Ergebnisse deuten darauf hin, dass spezifische Kombinationen von Katalysatoren die durch die lineare Skalierungsbeziehung auferlegten Beschränkungen überwinden können. Wir konnten allgemeine Trends feststellen, die die Effizienz des bifunktionalen Mechanismus bestimmen. Insbesondere kann eine Korrelation zwischen dem Valenzbandmaximum und der Wasserstoffbindungsenergie als Deskriptor bei der zukünftigen Suche nach geeigneten Wasserstoffakzeptoren innerhalb des bifunktionalen Schemas verwendet werden. Als nächstes werden in einer detaillierten Studie über NiOOH/FeOOH-Katalysatoren die für den bifunktionellen Mechanismus günstigsten Merkmale identifiziert. Für bestimmte Konfigurationen werden Überpotentiale von nur 0,13 eV gefunden. Diese Ergebnisse unterstützen den bifunktionellen Mechanismus als Mittel zum Aufbrechen der linearen Skalierungsbeziehungen.

Zweitens werden Lochpolaronen an der TiO_2-Oberfläche untersucht, die durch elektronegative Adsorbate in den OER-Zwischenprodukten induziert werden. Die sogenannte CHE-Methode in Verbindung mit mit einem hybriden Dichtefunktional wird zur Quantifizierung der Wirkung der Oberflächenpolaronen auf die Gibbs-Energiedifferenzen der OER eingesetzt. Wir stellen fest, dass die Loch-Bipolaronen das Überpotential des reaktionsbestimmenden Schritts reduzieren, was zu einer guten Übereinstimmung mit dem Experiment führt. Die Stabilität der Polaronen wird an der hydratisierten Oberfläche durch eine Freie-Energie-Studie unter expliziter Behandlung des Lösungsmittels weiter bestätigt. Schließlich wird das Energieniveau der Polaronen in Bezug auf die Redoxniveaus in Wasser ausgerichtet, um die Rolle der Polaronen im OER besser zu verstehen. Da das Auftreten von Oberflächenlochpolaronen nicht mit den Skalierungsbeziehungen zusammenhängt, bietet es einen zusätzliche Alternative bei der Suche nach verbesserten Katalysatoren.

Stichwörter: Reaktion zur Sauerstofferzeugung, OER, bifunktionaler Reaktionsmechanismus, Gibbs-Energie, Überpotential, lineare Skalierungsbeziehungen, Polaronen, Lösungsmittelwirkung

Contents

Acknowledgements **i**

Abstract (English/Deutsch) **ii**

1 Introduction **1**

1.1 Oxygen Evolution Reaction Mechanisms and Linear Scaling Relationships . . . 4

1.2 Current Computational Modeling of the Oxygen Evolution Reaction 7

1.3 Effect of Polarons on the Oxygen Evolution Reaction . . . 9

1.4 Bifunctional Mechanism . . . 10

1.5 Thesis Outline . . . 11

2 Methodology **15**

2.1 Density Functional Theory . . . 16

2.1.1 Implementation of Density Functional Theory in CP2K . . . 18

2.1.2 Hybrid Density Functionals . . . 19

2.2 Geometry Optimization, Vibrational Analysis, and Molecular Dynamics 22

2.2.1 Geometry Optimization . . . 22

2.2.2 Vibrational Analysis . . . 23

2.2.3 Molecular Dynamics 26

2.3 Thermodynamic Integration 29

2.4 Blue Moon 31

3 Computational Hydrogen Electrode 33

3.1 Formulation of the Computational Hydrogen Electrode Method . . . 34

3.2 Linear Scaling Relationships 37

3.2.1 Computational Details 37

3.2.2 Results 38

3.3 Hybrid Functional Level of Theory 41

3.3.1 Computational Details 41

3.3.2 Results and Discussion 42

3.4 The OER Mechanism on the Platinum Electrode under Potential Bias 45

3.4.1 Observations from Constant Fermi Level Molecular Dynamics 45

3.4.2 Results and Discussion 46

3.5 Conclusion 49

4 Effect of Solvent on the Oxygen Evolution Reaction on TiO_2 51

4.1 OER Free Energies through Thermodynamic Integration 53

4.2 Computational Details 55

4.2.1 Computational Hydrogen Electrode 55

4.3 Results 57

4.4 Origin of the Solvent Effect 62

4.4.1 Structural Analysis 62

4.4.2 Electrostatic Analysis 63

4.5 Full Oxygen Evolution Reaction Pathway 65

4.6 Discussion and Conclusion 69

5 Bifunctional Oxygen Evolution Reaction Mechanism 71

5.1 Trends and Principles Governing the Efficiency of the Bifuctional Mechanism 73

5.1.1 Anodic Conditions 73

5.1.2 Bifunctional Mechanism 74

5.1.3 Band Edge Alignment as Descriptor 77

5.1.4 Discussion and Conclusion 81

5.2 The Bifunctional γ-NiOOH/γ-FeOOH Catalyst 84

5.2.1 FeOOH 85

5.2.2 NiOOH 87

5.2.3 Bifuncional FeOOH/NiOOH Catalyst 89

5.2.4 Conclusion 93

6 Effect of Surface Hole Polarons on the OER at the TiO_2/Water Interface 95

6.1 Computational Details 96

6.2 Hole Polarons at the Vacuum Interface 97

6.3 Effect on the Free Energy Steps of the OER 99

6.4 Hole Polarons at the TiO_2/Water Interface 101

6.5 Polaron Energy Level Alignment 103

6.5.1 Results 104

6.6 Conclusion 110

7 Conclusion **113**

Bibliography **119**

Curriculum Vitae **130**

1 Introduction

The global energy demands increase year by year, with over 160’000 TWh consumed just in 2018.[1] With the increase of the global population, and the improvement in the standard of living in many developing countries, this figure is expected to keep increasing in the coming decades. As of now, fossil fuels (coal, natural gas, and oil) account for nearly 85% of the global energy consumption, whereas the remaining 15% are split between nuclear, hydro, and renewable sources.[1] At the same time, the burning of fossil fuels leads to an annual release of more than 35 billion tons of CO_2 into the atmosphere. This unprecedented increase in greenhouse gas concentrations could, if uninhibited, lead to irreversible changes in the environment, which will negatively affect the poorest regions of the world.[2–4] Given the above, radical measures are undertaken to develop new, clean sources of energy, and to increase the use of renewable sources. For instance, the European Union vowed to increase the share of energy from renewable sources to 20% of gross energy consumption by the end of 2020, and to 32% by the year 2030.[5] Simultaneously, nearly €5.9 billion out of the €33 billion Horizon 2020 program is dedicated to energy research and innovation projects.[6] Other global leaders are committed to comparable plans, enabling rapid advances in the development and adoption of novel energy sources and energy storage solutions. These large-scale initiatives have a marked impact on several industrial sectors.

The transportation sector, which accounts for a sizeable fraction of the total global energy consumption (29%),[7] is being transformed in the wake of electric car adoption and the upcoming plans of many countries to eventually ban internal combustion engine vehicles. For example, China, UK, and several EU countries are either discussing, or have already undertaken steps to discontinue the sale of new gasoline-

and diesel-fueled passenger vehicles by as early as 2030.[8–11] While the electrification of light-duty vehicles is underway, the commercial transport sector still relies heavily on fossil fuels. Hence, novel, clean fuel sources are required which can rival fossil fuels when it comes to energy density, availability, and convenience of storage. Hydrogen fuel cells are promising in this regard. Indeed, hydrogen fuel cell buses operate in many cities across the world, and their use is expected to expand in the coming years even further.[12] Hydrogen is likewise an important commodity in the chemical industry. While fossil fuel refineries account for nearly one third of the global hydrogen consumption, the main use of hydrogen is found in the production of ammonia and methanol.[13]

The overwhelming majority of hydrogen (~96%) is currently produced from fossil fuels.[13] The most widely adopted method is steam reforming of natural gas, where methane reacts with water vapour to form carbon monoxide and H_2.[14] This process is endothermic, and requires a considerable amount of heat that is usually supplied by burning the natural gas itself. Most of the remaining hydrogen production can be attributed to electrolysis. Depending on the specific process, electricity can be converted into H_2 with an efficiency of up to 80%.[13] Nevertheless, a supply of electric energy, as well as H_2O_2, is required. In light of the ongoing efforts to reduce our dependence on fossil fuels, a clean and renewable source of hydrogen is critical to achieve a widespread adoption of hydrogen fuel cells in the transportation industry, and to meet the increasing demands for hydrogen in the chemical industry. Photoelectrocatalytic water splitting is one such promising technology.

In recent years, much progress was made in the development of photoelectrocatalytic cells for water splitting.[15–20] The basic operating principle of a simple photoelectrocatalytic cell is illustrated in Fig. 1.1. Electrodes submerged in a water-based electrolyte absorb sunlight and the photogenerated electron-hole pair drives the splitting of water into oxygen and hydrogen. On the right hand side, the cathode facilitates the production of hydrogen by injecting electrons into the solvent, which then recombine with solvated protons at the surface of the electrode. This is referred to as the hydrogen evolution reaction (HER), and the appropriate redox level is that of the reversible hydrogen electrode (RHE). On the left hand side, the anode is involved in the actual water splitting, in which water molecules are split into protons and oxygen gas. Hence, this is the oxygen evolution reaction (OER), and it is associated with the water oxidation potential H_2O/O_2. As Fig. 1.1 illustrates, a suitable anode material is a semiconductor with a band gap that is small enough to absorb sunlight efficiently, yet at the same time large enough to straddle the water splitting redox levels. In that way, the photogenerated holes can drive the OER, while the electrons travel to the cathode and drive the HER. The hydrogen reduction potential and the water splitting potential are separated by 1.23 eV.[21,22]

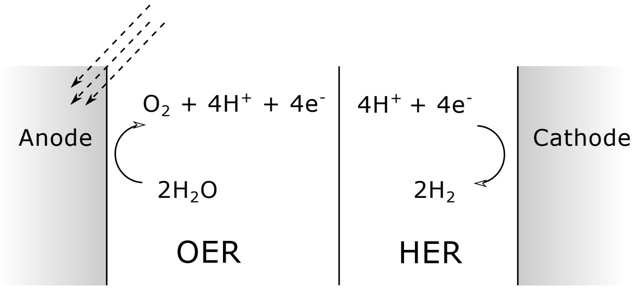

Figure 1.1 – Illustration of a photoelectrocatalytic cell for water splitting.

Four proton-electron pairs need to be transferred in the oxygen evolution reaction $2H_2O_{(\ell)} \xrightarrow{4.92\ \mathrm{eV}} O_{2(g)} + 4H^+ + 4e^-$. The ideal anode material catalyzes the reaction so that the reaction free energy of 4.92 eV is distributed equally among all four reaction steps, leading to the optimal value of 1.23 eV for each Gibbs free energy step. In practice, at least some reaction steps require extra bias to facilitate them, called the overpotential. The unifying theme of this work is the use of *ab-initio* free energy methods in order to calculate the free energy steps associated with the OER from first principles. This ability to evaluate the reaction overpotential allows us to identify materials and reaction mechanisms that lead to superior catalytic activities.

This chapter is structured as follows. First, we introduce the oxygen evolution reaction in more detail and discuss various reaction mechanisms. The emergence of linear scaling relationships which limit the catalytic efficiency of large classes of materials is described. Second, we address the current state-of-the-art free energy method, as well as its limitations, notably temperature effects and the inclusion of solvent. Third, promising strategies to overcome or avoid the linear scaling relationships are presented. For one thing, bifunctional reaction schemes are introduced. For another, the effect of polarons on the OER is discussed.

1.1 Oxygen Evolution Reaction Mechanisms and Linear Scaling Relationships

The four electron oxygen evolution reaction:

$$2H_2O_{(\ell)} \longrightarrow O_{2(g)} + 4H^+ + 4e^-, \tag{1.1}$$

can take place following various reaction pathways. First, the reaction mechanism is pH dependent. In acidic conditions, the commonly adopted mechanism consists of the following four proton-coupled electron transfer (PCET) steps:[23–25]

$$\begin{aligned} H_2O_{(\ell)} &\longrightarrow OH_{ads} + H^+ + e^-, \\ OH_{ads} &\longrightarrow O_{ads} + H^+ + e^-, \\ O_{ads} + H_2O_{(\ell)} &\longrightarrow OOH_{ads} + H^+ + e^-, \\ OOH_{ads} &\longrightarrow O_{2(g)} + H^+ + e^-, \end{aligned} \tag{1.2}$$

where all reaction intermediates are adsorbed at a single active site on the catalyst surface. At variance, in alkaline conditions, charge transfer is mediated by hydroxide groups:[26]

$$\begin{aligned} OH^- &\longrightarrow OH_{ads} + e^-, \\ OH_{ads} + OH^- &\longrightarrow O_{ads} + H_2O_{(\ell)} + e^-, \\ O_{ads} + OH^- &\longrightarrow OOH_{ads} + e^-, \\ OOH_{ads} + OH^- &\longrightarrow O_{2(g)} + H_2O_{(\ell)} + e^-. \end{aligned} \tag{1.3}$$

Even though these mechanisms differ, the reaction intermediates are identical in both cases, which facilitates the generalization of computational approaches to both pH regimes. Henceforth, we will assume acidic condition, unless stated otherwise. As a consequence of the Sabatier and the Brønsted-Evans-Polanyi principles, the catalytic efficiency of a material depends on the binding energies of the reaction intermediates OH_{ads}, O_{ads}, and OOH_{ads}.[27] If any given adsorbate is bound too strongly, the reaction step proceeding from this intermediate becomes improbable, reducing the efficiency of the whole reaction. If instead it is bound too weakly, the step resulting in the intermediate is the reaction limiting one. This can not only affect the catalytic efficiency, but also lead to the selection of different OER mechanisms. For instance, if the formation of the OOH_{ads} intermediate is exceedingly unfavorable due to its weak binding energy, the OER may proceed through a dissociative mechanism:[28]

$$\begin{aligned} 2\times\left(\mathrm{H_2O_{(\ell)}} \longrightarrow \mathrm{OH_{ads}} + \mathrm{H^+} + e^-\right),\\ 2\times\left(\mathrm{OH_{ads}} \longrightarrow \mathrm{O_{ads}} + \mathrm{H^+} + e^-\right),\\ 2\mathrm{O_{ads}} \longrightarrow \mathrm{O_{2(g)}}. \end{aligned} \tag{1.4}$$

If, instead, the formation of O_{ads} is associated with a large overpotential, then a mechanism that omits O_{ads} might be preferable:[29]

$$\begin{aligned} 2\times\left(\mathrm{H_2O_{(\ell)}} \longrightarrow \mathrm{OH_{ads}} + \mathrm{H^+} + e^-\right),\\ 2\mathrm{OH_{ads}} \longrightarrow \mathrm{OOH_{ads}} + \mathrm{H^+} + e^-,\\ \mathrm{OOH_{ads}} \longrightarrow \mathrm{O_{2(g)}} + \mathrm{H^+} + e^-. \end{aligned} \tag{1.5}$$

Given a novel catalyst, the various possible reaction pathways ought to be investigated in order to identify the mechanism with the lowest overpotential. However, based on their characteristics, it is often assumed that for materials belonging in a given class the same reaction mechanism will be favored.

Once a reaction mechanism is chosen, the free energy steps corresponding to each PCET can be calculated. Comprehensive computational studies of large sets of materials have been carried out.[23,30,31] It has been found that the reaction free energy steps are not mutually independent across different materials. In fact, linear scaling relationships exist between the free energy steps which put a limit on the catalytic efficiency of large classes of materials. In particular, it was found that the average of the sum of the free energies corresponding to the second and the third step of Eqs. (1.2) is equal to 3.2 eV in the case of simple and complex transition metal oxides, see Fig. 1.2(a).[23] The ideal reaction free energy of each step is 1.23 eV. Therefore, the optimal sum of the second and third free energy step is 2.46 eV. The linear scaling relationship thus leads to the emergence of an overpotential on at least one of the two reaction steps involved. Figure 1.2(b) shows the reaction overpotential as a function of the second free energy step. This is commonly referred to as a volcano plot. Materials situated at the apex of the volcano exhibit values of the second and third free energy step that are nearly equal, and thus have the lowest overpotential. However, due to the linear scaling law, even the top of the volcano does not reach the ideal 0 eV overpotential line.

While the linear scaling laws are statistical in their nature, they are robust with

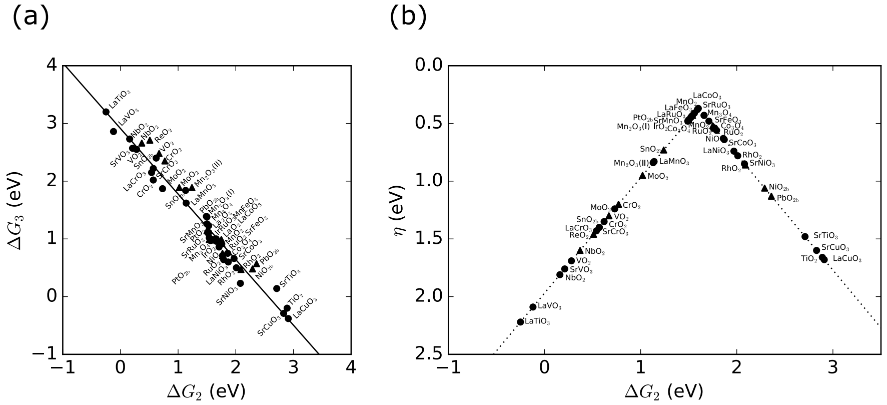

Figure 1.2 – (a) The linear scaling relationship between the second and the third OER step for a set of transition metal oxides. (b) Volcano plot depicting the overpotential η as a function of a single descriptor, the second free energy step ΔG_2. Data obtained from Ref. [23].

respect to the choice of functional,[32] and are present irrespective of the adopted reaction mechanism.[28]

1.2 Current Computational Modeling of the Oxygen Evolution Reaction

The computational hydrogen electrode (CHE) method, developed by Nørskov *et al.*,[31] enables the evaluation of the free energy differences corresponding to PCET reactions. Density functional theory (DFT) is used to calculate the binding energies of the reaction intermediates at the surface of the catalyst. Thermodynamic corrections, such as the zero point energy of lattice vibrations and entropy contributions, are then added to these binding energies. A detailed description of the method is given in Sec. 3.1. While the CHE method is reasonably successful at predicting the overall reaction overpotentials of the OER,[33] it suffers from two drawbacks. First, temperature effects are included only in an approximate fashion. Second, the effect of the solvent is disregarded, or only roughly approximated, and thus its role remains elusive.

The solvation effect is multi-faceted in nature. For one thing, the solvent can stabilize or destabilize the adsorbate, changing the binding energies of the reaction intermediates.[34] Another important role of the solvent lies in the complex way it affects the entropy contributions to the free energy differences. Various schemes have been employed to quantify the effects of the solvent. The roughest approximation ignores the solvent completely.[23] The assumption here is that the solvent affects all the intermediates nearly equally, and thus the solvation effect cancels out in the free energy differences considered. Implicit solvation methods approximate the solvent through a continuum model based on electrostatics.[35–38] Although this approach works well for long range effects, the method cannot account for the immediate vicinity of an adsorbate in contact with a protic solvent such as liquid water, which interacts significantly with solutes through hydrogen bonds and van der Waals interactions. Furthermore, in this case, it is difficult to distinguish the effect of the solvent from the adopted implicit approximation. Explicit solvation methods can employ one or several layers of water molecules in a DFT calculation to compute the binding energies of adsorbates. These water layers are placed above the surface and can be ice-like or undergo structural relaxation.[34,39–43] In this approach, the solvation effect amounts to a straightforward correction to the binding energies of the reaction intermediates. If the water layer is allowed to relax, a doubt remains whether the optimized water structure is an accurate representation of the liquid at the solvated interface.[41] In any case, DFT structural relaxations are performed at

0 K, and therefore such schemes fail in describing the finite temperature behavior of liquid solvents. Furthermore, relaxation of the water layer near the adsorbate can lead to an overestimate of the stabilization due to hydrogen bonds, some of which can be disrupted in finite temperature dynamics where disorder is taken into account.[41] More sophisticated modeling of the solvent involves molecular dynamics (MD) simulations, which sample multiple local minima of the geometry by simulating the finite temperature behavior of the system from first principles. In conjunction with thermodynamic integration (TI),[44] such MD simulations enable one to compute the free energy of a reaction in the presence of an explicit solvent.[45–48]In particular, Cheng *et al*. applied such a scheme to the PCET steps of the oxygen evolution reaction at the TiO_2-water interface.[46] However, there was no attempt to isolate the effect of the solvent, and it thus remains unclear whether this high-level modeling improves the description of the reaction with respect to simpler approaches, such as the CHE method.

Apart from the drawbacks concerning the inclusion of the solvent, most current studies employ the CHE method in conjunction with semilocal DFT. This level of theory offers reasonable accuracy at a relatively low computational cost. Indeed, one of the main benefits of the CHE method is its low computational cost, making it feasible to screen large numbers of potential catalysts. While not a limitation of the CHE method *per se*, it is important to note that the calculated free energy steps are dependent on the adopted level of theory.[49,50] For example, the use of more advanced energy functionals is required to correctly address charge localization effects. A discussion of advanced DFT functionals is postponed until Chapter 2. Charge localization effects are intimately related to, among other things, the formation of polarons, which are the subject of the next section.

1.3 Effect of Polarons on the Oxygen Evolution Reaction

Polarons are localized charge defects accompanied by a lattice distortion, and have been theoretically studied and experimentally observed in many materials relevant to electrocatalytic water splitting, including TiO_2,[46,51–56] and $BiVO_4$.[57–60] Depending on the type of trapped charge, we distinguish between hole and electron polarons. In the case of the OER, which takes place under anodic conditions, hole polarons are of especially great interest. Furthermore, the exposure of surfaces required for catalysis facilitates the formation of defects, including polaronic ones. Indeed, bulk polarons have been found in some materials to travel to the surface, where they become trapped.[60,61] On the one hand, such trapped charged defects at the surface are investigated in connection with the initiation of the water splitting process, which is critical for the OER.[57,62,63] On the other hand, the presence of polarons may enhance electron-hole recombination processes, or slow down charge transport due to slow polaron hopping, thereby negatively affecting the catalytic performance of the material.[60,64,65]

From a computational point of view, the study of polaronic defects is complicated by the necessity of employing higher levels of theory. Semilocal DFT suffers from self-interaction effects that lead to an erroneous delocalization of charges. As a consequence, more advanced approaches, such as DFT+U or hybrid density functionals, need to be adopted in order to accurately describe polarons. While DFT+U offers a lower computational cost, it often yields polaron formation energies that are at odds with the results obtained with the more costly hybrid density functionals.[66,67] Great effort needs to be expended carefully assessing the relative accuracy of these methods.[68]

1.4 Bifunctional Mechanism

As discussed in Sec. 1.1, the adoption of a mechanism involving a single active site leads to the emergence of linear scaling relationships that limit the catalytic efficiency of the OER. In fact, even mechanisms that involve two qualitatively identical active sites suffer from this issue.[28] Hence, bifunctional schemes, in which two functionally different active sites take part in the catalysis, are investigated as a possible means to avoid the linear scaling.[69–74] The most problematic linear scaling relationship is observed between the second and the third step of the mechanism in Eqs. (1.2), $\Delta G_2 + \Delta G_3 \approx 3.2$ eV.[23,31] The free energy steps in this scaling involve the formation of the O_{ads} and OOH_{ads} intermediates. In practice, the latter is often found to bind weakly, leading to a large value of the third free energy step ΔG_3. Hence, bifunctional schemes involving a second active site are envisaged to break the unfavorable scaling either by stabilization of the OOH_{ads} intermediate, or by avoiding it completely.

In the former case, the second active site can be used to form a strong hydrogen bond with OOH_{ads} in order to stabilize it and thus reduce ΔG_3.[73,75] This may be achieved via doping or defect engineering.[26] In the latter case, the formation of OOH_{ads} can be avoided through a mechanism analogous to Eqs. (1.5), in which two O_{ads} intermediates at qualitatively different sites combine to form $O_{2\,ads}$. Another possibility to avoid OOH_{ads} formation lies in using a strong hydrogen acceptor as the second active site, leading to the simultaneous formation of $O_{2\,ads}$ and H_{ads}.[72,74,76] In this last scenario, the suggested reaction mechanism consists of the following four PCET steps:

$$\begin{aligned} H_2O_{(\ell)} &\longrightarrow OH_a + H^+ + e^-, \\ OH_a &\longrightarrow O_a + H^+ + e^-, \\ O_a + H_2O_{(\ell)} &\longrightarrow H_b + O_{2(g)} + H^+ + e^-, \\ H_b &\longrightarrow H^+ + e^-, \end{aligned} \tag{1.6}$$

where a and b refer to adsorbed species at two different but close active sites on the surface of the catalyst. In a recent work, Song *et al.* propose this mechanism as a possible explanation for the high catalytic activity of a novel nickel/iron catalyst.[76] Indeed, the measured OER overpotential lies far below the limit imposed by the linear scaling relationship, suggesting that the bifunctional mechanism offers a real possibility to achieve efficient electrocatalytic production of hydrogen.

1.5 Thesis Outline

This thesis is organized as follows. In Chapter 2 we describe the methodology adopted in this work. First, density functional theory and related computational methods are introduced and some aspects of their implementation in the CP2K suite of codes are presented. Second, two methods to calculate free energies from DFT, namely the thermodynamic integration method and the Blue Moon sampling, are discussed.

Chapter 3 addresses in detail the computational hydrogen electrode method, the current state-of-the art in the field of computational catalysis. The method is presented, and subsequently applied to the problem of the OER. The emergence of linear scaling laws is shown to limit the catalytic efficiency for a set of materials. The effect of the adopted level of theory is addressed by using hybrid density functionals and drawing a comparison with results obtained using semilocal functionals. Finally, the CHE approach is applied in conjunction with more advanced methods to examine an alternative OER mechanism on a platinum electrode under potential bias.

Chapter 4 investigates the effect of the solvent on the OER free energy steps. TiO_2 is chosen as the anode material. Reaction free energies are calculated in the presence of a fully explicit, atomistic solvent using a thermodynamic integration approach. The same framework is applied to the case without the solvent, which allows for the isolation of the solvent effect on the OER free energy steps. The solvent effect is evaluated in terms of structural modifications and the hydrogen bond network, as well as electrostatic effects.

In Chapter 5, we study a bifunctional OER mechanism by performing CHE calculations for a selection of potential catalysts. The bifunctional mechanism introduces a second active site which serves as a hydrogen acceptor, avoiding limitations imposed by the linear scaling relationship, and thus leading to very low OER overpotentials. The mechanism, and its potential in reducing overpotentials, is evaluated both at the semilocal and hybrid functional levels of theory. We find that the bifunctional scheme appears promising irrespective of the adopted functional. Furthermore, we identify a descriptor, robust with respect to the choice of functional, which could be used in determining the performance of possible hydrogen acceptors within the bifunctional framework. Subsequently, a catalyst consisting of γ-NiOOH and γ-FeOOH proposed by Song *et al.*[76] is investigated in detail. Various configurations of the two materials are studied, and their performance in the bifunctional scheme is evaluated.

Chapter 6 deals with the effect of surface hole bipolarons on the energetics of the OER at the rutile TiO_2 surface. The OER free energies are calculated in the framework of the CHE method at the semilocal and hybrid functional levels of theory. In the latter, the formation of surface hole bipolarons at the vacuum interface is observed. We analyze the effect of these polarons on the reaction free energies. We further investigate the stability of the polarons at the hydrated interface, and calculate the formation free energy profile under realistic conditions. The charge transfer levels corresponding to the polaron are identified, and aligned with respect to the band edges and water redox levels in order to further elucidate the effect of such polarons on the OER.

Finally, Chapter 7 concludes this thesis by summarizing all the results obtained.

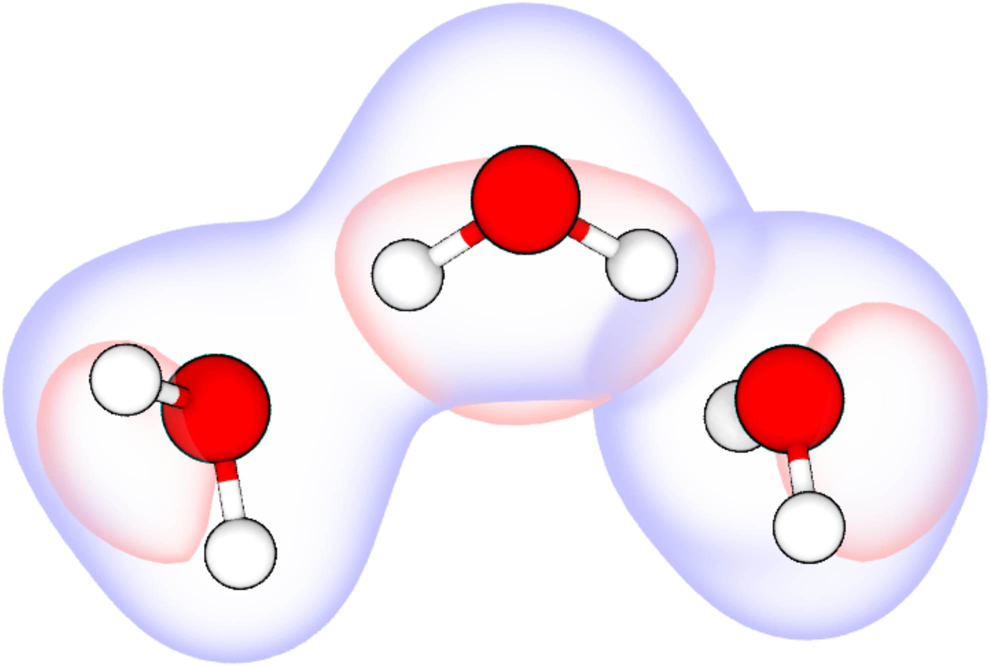

2 Methodology

In this chapter, we present the methods used throughout this work. First, the electronic structure methods, and their implementation in the CP2K[77] code, are discussed. Density functional theory is introduced and the semilocal and hybrid exchange and correlation functionals are presented. Second, a brief overview of geometry optimization and vibrational analysis algorithms is given. Finally, two methods for calculating free energies are introduced. The thermodynamic integration method and the Blue Moon ensemble method allow for first-principles calculations of free energies at finite temperatures. The discussion of the computational hydrogen electrode method, mentioned in the Introduction, is postponed until Chapter 3.

Left: Illustration of the electron density of a set of water molecules obtained using density functional theory.

2.1 Density Functional Theory

Density functional theory is built upon two founding theorems by Hohenberg and Kohn. The first theorem[78] posits that the external potential, and hence the total energy of a system of electrons, is a unique functional of the electron density. In other words, the many-body problem of N electrons with $3N$ spatial coordinates can be reduced to only three spatial coordinates of the ground state electron density $n_0(\mathbf{r})$. The second Hohenberg-Kohn theorem[78] introduces a density functional for the energy of the system, and proves that the ground state electron density minimizes it. Subsequently, Kohn and Sham provided a practical way of calculating this ground state electron density, and as per the Hohenber-Kohn theorems, all the information about the ground state of the many electron system. An auxiliary system of non-interacting electrons in an effective potential V_{eff} is set up:

$$H_{\text{KS}} \equiv -\frac{1}{2}\nabla^2 + V_{\text{eff}}(\mathbf{r}) = -\frac{1}{2}\nabla^2 + v(\mathbf{r}) + V_{\text{H}}(\mathbf{r}) + V_{\text{xc}}(\mathbf{r}), \tag{2.1}$$

where $v(\mathbf{r})$ is the Coulomb potential of the electron-ion interaction:

$$v(\mathbf{r}) = -\sum_{k=1}^{N_{\text{i}}} \frac{Z_k}{|\mathbf{r} - \mathbf{R}_k|}, \tag{2.2}$$

N_{i} being the number of ions, Z_k their charges, and $\mathbf{R}_k$ their positions, $V_{\text{H}}(\mathbf{r})$ is the Hartree potential of the electron-electron interaction:

$$V_{\text{H}}(\mathbf{r}) = \int \frac{n(\mathbf{r}')}{|\mathbf{r} - \mathbf{r}'|} \mathrm{d}\mathbf{r}', \tag{2.3}$$

and $V_{\text{xc}}(\mathbf{r})$ is the exchange and correlation potential defined as:

$$V_{\text{xc}}(\mathbf{r}) \equiv \frac{\delta E_{\text{xc}}[n]}{\delta n} \quad \text{where} \quad E_{\text{xc}}[n] \equiv \int n(\mathbf{r}')\epsilon_{\text{xc}}(\mathbf{r}')\mathrm{d}\mathbf{r}'. \tag{2.4}$$

Here, $E_{\text{xc}}[n]$ is the exchange and correlation functional, and ϵ_{xc} is the exchange and correlation energy density. The solutions of the following system of equations:

$$H_{\text{KS}}\psi_i(\mathbf{r}) \equiv \left[-\frac{1}{2}\nabla^2 + v(\mathbf{r}) + V_{\text{H}}(\mathbf{r}) + V_{\text{xc}}(\mathbf{r})\right]\psi_i(\mathbf{r}) = \epsilon_i\psi_i(\mathbf{r}) \qquad \forall i \in \{1,\ldots,N\}, \tag{2.5}$$

then yield the ground state electron density of the original, interacting system n_0:

$$\sum_{i=1}^{N} \left|\psi_i(\mathbf{r})\right|^2 \equiv n(\mathbf{r}) = n_0(\mathbf{r}). \tag{2.6}$$

There are two things to note. First, the effective potential V_{eff} is itself a function of the ground state electron density we are trying to calculate. Hence, we proceed by self-consistently solving Eq. (2.5), refining the input electron density n until we reach convergence.

Second, the actual form of the exchange and correlation function in Eq. (2.4) is unknown, and hence only an approximation can be used. Generally, a balance between accuracy and computational cost must be struck here. The local density approximation (LDA) based on the homogeneous electron gas (HEG) represents a class of functionals that depend solely on the electron density n, rather than on its derivatives or on the Kohn-Sham orbitals ψ_i. The LDA exchange and correlation functional is given by:

$$E_{\text{xc}}^{\text{LDA}}[n] = \int n(\mathbf{r}')\epsilon_{\text{xc}}(\mathbf{r}';n)\mathrm{d}\mathbf{r}', \tag{2.7}$$

where the energy density ϵ_{xc} only depends on the electron density at the location where the functional is evaluated. While the exchange part of ϵ_{xc} is known analytically, the correlation part is usually an analytical parametrization of numerical results achieved with quantum Monte Carlo simulations of the HEG.[79–82]

The semilocal generalized gradient approximation (GGA) consists in including the gradient of the electron density in the functional dependence of the exchange and correlation energy density:

$$E_{\text{xc}}^{\text{GGA}}[n] = \int n(\mathbf{r}')\epsilon_{\text{xc}}(\mathbf{r}';n,\nabla n)\mathrm{d}\mathbf{r}'. \tag{2.8}$$

Here we will mention the efforts by Perdew and Wang, who developed the PW86 functional,[83] and by Perdew, Burke, and Ernzerhof, who proposed the non-empirical, parameter-less PBE functional.[84] In general, GGA functionals lead to better accuracy than LDA functionals for a wide range of calculated properties.[85,86]

However, these functionals still exhibit limitations. Perhaps most importantly, the sum $E_{\text{xc}} + E_{\text{H}}$ of the exchange and correlation energy and the Hartree energy does not vanish in the case of a single electron problem. Moreover, an extension of DFT to fractional electron numbers should lead to a piece-wise linear dependence of the total energy on the electron number. However, both LDA and GGA result in a convex dependence thereof. All this is related to the self-interaction error, which limits the accuracy of semilocal DFT in calculating ionization potentials, energy band gaps, and other important electronic structure properties. Hybrid density functionals combine exchange and correlation at the LDA or GGA level with the exact exchange of the Fock operator.[87–90] The superior performance of such hybrid functionals is rationalized in terms of the concave energy dependence of the total energy on fractional electron number in the case of pure Fock exchange. A combination of DFT exchange and Fock exchange can thus ameliorate the self-interaction error. A more detailed discussion of selected hybrid density functionals, and their practical implementation, is deferred to Sec. 2.1.2.

2.1.1 Implementation of Density Functional Theory in CP2K

We use the CP2K suite of codes for all electronic structure calculations.[77,91] In CP2K, Kohn-Sham DFT is implemented in the QuickStep program, a mixed Gaussian and plane wave (GPW) code.[91,92] The electron density is represented alternatively using either a Gaussian basis:

$$n(\mathbf{r}) = \sum_{\mu\nu} P_{\mu\nu}\varphi_{\mu}(\mathbf{r})\varphi_{\nu}(\mathbf{r}), \tag{2.9}$$

where P is the density matrix and $\varphi_{\mu}(\mathbf{r}) = \sum_i d_{i\mu} g_i(\mathbf{r})$, with primitive Gaussian functions $g_i(\mathbf{r})$ and their coefficients $d_{i\mu}$, or a plane wave basis:

$$\tilde{n}(\mathbf{r}) = \frac{1}{\Omega}\sum_{\mathbf{G}} \tilde{n}(\mathbf{G})\exp(\mathrm{i}\mathbf{G}\cdot\mathbf{r}), \tag{2.10}$$

where $\mathbf{G}$ are the reciprocal lattice vectors and Ω is the volume of the unit cell. These two representations are chosen is such a way that $n(\mathbf{r}) = \tilde{n}(\mathbf{r})$ on a regular Cartesian grid. Furthermore, a multi-grid method using several grids of increasing resolution allows one to speed up the computation of matrix element and densities without incurring an accuracy penalty. This dual approach enables one to choose a representation most conducive to any given operation. In effect, the plane wave representation serves as an auxiliary basis used in conjunction with fast Fourier transforms, and other efficient algorithms, where possible. At the same time, the nature of Gaussian functions allows one to greatly speed up e.g. the calculation of two-point integrals, where terms involving the product of Gaussian functions sufficiently far away in real space can be screened.

The electron-ion potential in Eq. (2.2) is evaluated using pseudopotentials. The expansion of wave functions and densities for core electrons is computationally inefficient. Concomitantly, most interesting phenomena are associated with valence electrons only. Hence, the ionic potentials are replaced with pseudopotentials that lead to an identical behavior of valence electrons, while avoiding the computationally costly description of core electrons. Analytical, norm-conserving Goedecker-Tetter-Hutter (GTH) pseudopotentials are used for all elements. The free parameters of these pseudopotentials have been tuned in order to reproduce the results of all-electron simulations using various functionals, including PBE.

The orbitals of the valence electrons are expanded in spherical Gaussian basis sets. A progressive basis set family (SZV, DZVP, TZVP, TZV2P) of increasing valence (termed ζ) is constructed, allowing for a systematic convergence of the calculated properties.[91] While a SZV basis set only contains a single contracted function per atomic orbital, TZV2P contains three functions per orbital, plus two additional polarization functions for unoccupied orbitals. These basis sets are optimized for the use with GTH pseudopotentials. Additionally, they can be further optimized in conjunction with the PBE functional so as to achieve a high accuracy on a test set of small molecules. These latter basis sets are referred to as MOLOPT.[93]

2.1.2 Hybrid Density Functionals

Here, two hybrid density functionals, as well as their implementation in CP2K, are described.

PBE0

The PBE0 functional consists of PBE correlation $E_{\mathrm{c}}^{\mathrm{PBE}}$ and a mixture of PBE $E_{\mathrm{x}}^{\mathrm{PBE}}$ and Fock $E_{\mathrm{x}}^{\mathrm{HF}}$ exchange:[88,89]

$$E_{\mathrm{xc}}^{\mathrm{PBE0}} = E_{\mathrm{c}}^{\mathrm{PBE}} + \alpha E_{\mathrm{x}}^{\mathrm{HF}} + (1-\alpha) E_{\mathrm{x}}^{\mathrm{PBE}}, \tag{2.11}$$

where the fraction of Fock exchange is set to $\alpha = 0.25$. To speed up the evaluation of the Fock exchange, the range separated, truncated, PBE0 based functional PBE0-TC-LRC is implemented in CP2K.[94] This energy functional is given by:

$$E_{\mathrm{xc}}^{\mathrm{PBE0\ TC\ LRC}} = E_{\mathrm{c}}^{\mathrm{PBE}} + \alpha E_{\mathrm{x}}^{\mathrm{HF\ TC}} + \alpha E_{\mathrm{x}}^{\mathrm{PBE\ LRC}} + (1-\alpha)E_{\mathrm{x}}^{\mathrm{PBE}}, \tag{2.12}$$

where $E_{\mathrm{x}}^{\mathrm{HF\ TC}}$ represents the truncated Fock exchange, and $E_{\mathrm{x}}^{\mathrm{PBE\ LRC}}$ a long range PBE exchange correction. The truncated Coulomb (TC) Fock exchange is defined as:

$$E_{\mathrm{x}}^{\mathrm{HF\ TC}} \equiv -\frac{1}{2}\sum_{i=1}^{N}\sum_{j=1}^{N}\int\int \psi_i(\mathbf{r}_1)\psi_j(\mathbf{r}_1)g_{\mathrm{TC}}(\mathbf{r}_1,\mathbf{r}_2)\psi_i(\mathbf{r}_2)\psi_j(\mathbf{r}_2)\mathrm{d}\mathbf{r}_1\mathrm{d}\mathbf{r}_2, \tag{2.13}$$

where the form of the TC operator is governed by a tunable cutoff distance R_c:

$$g_{\mathrm{TC}}(\mathbf{r_1},\mathbf{r_2}) = \begin{cases} \dfrac{1}{|\mathbf{r}_1-\mathbf{r}_2|} & \text{for} \quad |\mathbf{r}_1-\mathbf{r}_2| \le R_c, \\ 0 & \text{for} \quad |\mathbf{r}_1-\mathbf{r}_2| > R_c, \end{cases} \tag{2.14}$$

The long range correction $E_{\mathrm{x}}^{\mathrm{PBE\ LRC}}$ is based on the exchange hole formulation of the PBE functional, and compensates for the absence of the Fock exchange for distances larger than the cutoff R_c.[95]

HSE06

The HSE06 functional is another similar range separated hybrid functional.[90] Referring to the electron-electron distance as r, the Coulomb operator of the Fock exchange is split into a short range (SR) and a long range (LR) part:

$$\frac{1}{r} = \frac{1-\mathrm{erf}(\omega r)}{r} + \frac{\mathrm{erf}(\omega r)}{r} \equiv \underbrace{\frac{\mathrm{erfc}(\omega r)}{r}}_{\mathrm{SR}} + \underbrace{\frac{\mathrm{erf}(\omega r)}{r}}_{\mathrm{LR}}. \tag{2.15}$$

Here, ω represents a screening parameter which defines the extent of the Fock exchange. Only the short range term $E_{\mathrm{x}}^{\mathrm{HF\ SR}}(\omega)$ is used in the evaluation of the Fock exchange. The long range exchange $E_{\mathrm{x}}^{\mathrm{PBE\ LR}}$ is that of the PBE functional. The HSE06 functional is thus given by:

$$E_{\mathrm{xc}}^{\mathrm{HSE06}} = E_{\mathrm{c}}^{\mathrm{PBE}} + E_{\mathrm{x}}^{\mathrm{PBE\ LR}}(\omega) + \alpha E_{\mathrm{x}}^{\mathrm{HF\ SR}}(\omega) + (1-\alpha)E_{\mathrm{x}}^{\mathrm{PBE\ SR}}(\omega). \tag{2.16}$$

The limit of $\omega \to 0$ represents the full Coulomb operator, while $\omega \to \infty$ leads to a pure PBE functional. In practice, a value of $\omega = 0.11$ bohr^{-1} was found to be a good compromise between accuracy and computational cost.[90,96]

Auxiliary Density Matrix Method

While the calculation of the Fock exchange in CP2K is already relatively fast on account of the Gaussian basis sets, the auxiliary density matrix method (ADMM) offers an additional speed-up.[97] Using an atom centered basis set as introduced in Eq. (2.9), the Fock exchange energy of Eq. (2.13) can be expressed as:

$$E_{\mathrm{x}}^{\mathrm{HF}} = -\frac{1}{2}\sum_{\lambda\sigma\mu\nu} P_{\mu\sigma}P_{\nu\lambda}\int\int \varphi_{\mu}(\mathbf{r}_1)\varphi_{\nu}(\mathbf{r}_1)g(\mathbf{r}_1,\mathbf{r}_2)\varphi_{\sigma}(\mathbf{r}_2)\varphi_{\lambda}(\mathbf{r}_2)\mathrm{d}\mathbf{r}_1\mathrm{d}\mathbf{r}_2, \tag{2.17}$$

where the density matrix elements $P_{\mu\sigma}$ are obtained from the coefficients $C_{i\mu}$ of the atom centered basis functions $\psi_i(\mathbf{r}) \equiv \sum_{\mu} C_{i\mu}\varphi_{\mu}(\mathbf{r})$:

$$P_{\mu\nu} = \sum_{i} C_{i\mu}C_{i\nu}. \tag{2.18}$$

The fourth order scaling in basis set size of the above expression is what leads to the inherently high computational cost of hybrid functionals. The ADMM introduces an auxiliary density matrix $\hat{P}$ such that:

$$\begin{aligned} E_{\mathrm{x}}^{\mathrm{HF}}[P] &\equiv E_{\mathrm{x}}^{\mathrm{HF}}[\hat{P}] + \left(E_{\mathrm{x}}^{\mathrm{HF}}[P] - E_{\mathrm{x}}^{\mathrm{HF}}[\hat{P}]\right) \\ &\approx E_{\mathrm{x}}^{\mathrm{HF}}[\hat{P}] + \left(E_{\mathrm{x}}^{\mathrm{GGA}}[P] - E_{\mathrm{x}}^{\mathrm{GGA}}[\hat{P}]\right), \end{aligned} \tag{2.19}$$

where the assumption is made that the difference between the Fock exchange energy evaluated for the primary and auxiliary density matrices is well approximated by GGA DFT. The validity of this assumption is evaluated in Ref. [97]. Using a smaller auxiliary basis set for the wave functions:

$$\hat{\psi}_i(\mathbf{r}) \equiv \sum_{\mu} \hat{C}_{i\mu}\hat{\varphi}_{\mu}(\mathbf{r}), \tag{2.20}$$

one can choose the coefficients $\hat{C}_{i\mu}$ so as to minimize the difference between the primary and auxiliary representation of the wave function. Due to the high-order scaling of the Fock exchange energy calculation, even a modest reduction of the basis set size leads to a notable improvement in performance.

2.2 Geometry Optimization, Vibrational Analysis, and Molecular Dynamics

The solution of the Kohn-Sham equations (2.5) yields the ground state electron density. Coupled with the ion-ion repulsion potential:

$$V_{\text{i-i}}\{\mathrm{R}\} \equiv \sum_{k=1}^{N_{\mathrm{i}}}\sum_{\substack{l=1 \\ k\neq l}}^{N_{\mathrm{i}}} \frac{Z_k Z_l}{|\mathbf{R}_k - \mathbf{R}_l|}, \tag{2.21}$$

one can obtain the electrostatic force acting on each atom. These forces can then be used for various purposes, such as optimizing the atomic configuration or lattice parameters, calculating the vibrational spectrum of the system, or evolving the system in time at finite temperature. Here we assume that due to the much lower mass of the electron compared to the nuclei, we can separate their motion. The electrons are subject to a quantum mechanical description, whereas the nuclei are governed by classical mechanics only. This is called the Born-Oppenheimer approximation. In this section, a short description of each of the methods mentioned above is given.

2.2.1 Geometry Optimization

One can obtain the lowest energy atomic configuration by iteratively solving the Kohn-Sham equations, calculating the forces acting on the nuclei, and updating their positions. There are several algorithms for optimizing the atomic configuration implemented in CP2K. Here we will focus on the Broyden-Fletcher-Goldfarb-Shanno (BFGS) algorithm.[98] It is efficient and relatively stable even for a large number of degrees of freedom. It does not require the exact evaluation of second derivatives, i.e. the full Hessian matrix. Only an initial Hessian matrix approximation B_0 is needed, which is then further refined at each iteration step i. The algorithm consists of the following steps:

- Use the approximate Hessian matrix B_i from the last iteration to obtain a direction $\mathbf{p}_i$ by solving $B_i\mathbf{p}_i = -\nabla E\{\mathbf{R}_i\}$, where $E\{\mathbf{R}_i\}$ is the total energy of the system in configuration $\mathbf{R}_i$.
- Perform a line search in direction $\mathbf{p}_i$ to find the size α_i of the displacement

that minimizes the total energy in that direction.

- Update the position of the nuclei by adding the above step $\mathbf{s}_i \equiv \alpha_i \mathbf{p}_i$ to the positions from the last iteration: $\mathbf{R}_{i+1} = \mathbf{R}_i + \mathbf{s}_i$.
- Calculate $\mathbf{y}_i \equiv \nabla E\{\mathbf{R}_{i+1}\} - \nabla E\{\mathbf{R}_i\}$.
- Refine the approximation of the Hessian matrix B_{i+1} using $\mathbf{s}_i$ and $\mathbf{y}_i$.

This procedure is repeated until the maximum and mean force $\nabla E\{\mathbf{R}_i\}$, as well as the maximum and mean step size α_i, fall below the adopted convergence criteria.

A modification of this algorithm can be used to optimize the lattice parameters as well as the atomic configuration at the same time. External strain tensor components are included as extra degrees of freedom, and the stress on the unit cell is calculated in addition to the forces at each iteration.[99] In CP2K, this is referred to as a cell optimization.

2.2.2 Vibrational Analysis

We consider an effective potential $W\{\mathbf{R}\}$ for the nuclei defined as the sum of the ion-ion Coulomb repulsion of Eq. (2.21) and the total DFT energy obtained from solving the Kohn-Sham equations (2.5). We introduce a small displacement to the atomic configuration:

$$\mathbf{R}_k = \mathbf{R}_{0k} + \mathbf{u}(k) \qquad \forall k \in \{1, \ldots, N_\mathrm{i}\}, \tag{2.22}$$

where, for the length of this section, we index a quantity using round brackets whenever convenient. The harmonic approximation is obtained by performing a Taylor expansion of this effective potential near the equilibrium configuration $\mathbf{R}_0$:

$$\begin{aligned} W\{\mathbf{R}\} = W\{\mathbf{R}_0\} &+ \sum_{k=1}^{N_\mathrm{i}} \left.\frac{\partial W}{\partial \mathbf{u}(k)}\right|_{\{R_0\}} \cdot \mathbf{u}(k) \\ &+ \frac{1}{2} \sum_{k=1}^{N_\mathrm{i}} \sum_{l=1}^{N_\mathrm{i}} \sum_{\alpha=x}^{z} \sum_{\beta=x}^{z} \left.\frac{\partial^2 W}{\partial u_\alpha(k) \partial u_\beta(l)}\right|_{\{R_0\}} u_\alpha(k) u_\beta(l) + \mathcal{O}(\mathbf{u}^3), \end{aligned} \tag{2.23}$$

and truncating it after the quadratic term. The constant term can further be disregarded as it does not affect the dynamics of the ions, and the linear term is negligible for a configuration close to the equilibrium configuration $\{\mathbf{R}_0\}$. Hence, the effective potential of the ions W is approximated by the harmonic potential:

$$\begin{aligned} W\{\mathbf{R}\} &\approx \frac{1}{2}\sum_{k=1}^{N_\mathrm{i}}\sum_{l=1}^{N_\mathrm{i}}\sum_{\alpha=x}^{z}\sum_{\beta=x}^{z} \left.\frac{\partial^2 W}{\partial u_\alpha(k)\partial u_\beta(l)}\right|_{\{R_0\}} u_\alpha(k)u_\beta(l) \\ &\equiv \frac{1}{2}\sum_{k=1}^{N_\mathrm{i}}\sum_{l=1}^{N_\mathrm{i}}\sum_{\alpha=x}^{z}\sum_{\beta=x}^{z} A_{\alpha\beta}(k,l)u_\alpha(k)u_\beta(l). \end{aligned} \tag{2.24}$$

The derivative of this potential along a displacement $\mathbf{u}(k)$ represents the negative force acting on atom k:

$$F_\alpha(k) \equiv -\frac{\partial W\{\mathbf{R}\}}{\partial u_\alpha(k)} = -\frac{1}{2}\sum_{l=1}^{N_\mathrm{i}}\sum_{\beta=x}^{z} A_{\alpha\beta}(k,l)2u_\beta(l), \tag{2.25}$$

where the factor of two comes from the derivative of the product of the two displacements for nuclei k and l through a change of indices in one of the resulting terms. Hence, the dynamics of the system of nuclei are governed by the equation of motion:

$$M_k\frac{\mathrm{d}^2u_\alpha(k)}{\mathrm{d}t^2} = -\sum_{l=1}^{N_\mathrm{i}}\sum_{\beta=x}^{z} A_{\alpha\beta}(k,l)u_\beta(l), \tag{2.26}$$

where M_k is the mass of nucleus k.

In a periodic system, such as a crystal or a computational cell with periodic boundary conditions, we further express the position of the nucleus k as:

$$\mathbf{R}_k = \mathbf{R}_{0k} + \mathbf{u}(k) \quad \longrightarrow \quad \mathbf{R}_{m\mu} = \mathbf{R}_{0m} + \rho_\mu + \mathbf{u}(m\mu), \tag{2.27}$$

where $\mathbf{R}_{0m}$ is the position of the unit cell m, and ρ_μ the position of nucleus μ relative to the unit cell. We look for a solution of Eqs. (2.26) in the form:

$$\mathbf{u}(m\mu,t) = \mathbf{u}_\mu e^{i\omega t}e^{i\mathbf{q}\cdot\mathbf{R}_{0m}}, \tag{2.28}$$

which is analogous to the Bloch theorem in the electronic structure theory of solids. From now on, Latin indices refer to the unit cell, and Greek indices refer to the nuclei within a unit cell. Plugging this *Ansatz* into the equation of motion (2.26) one obtains:

$$M_\mu \frac{\mathrm{d}^2}{\mathrm{d}t^2}\left[u_{\mu\alpha} e^{i\omega t} e^{i\mathbf{q}\cdot\mathbf{R}_{0m}}\right] = -\sum_n \sum_\nu \sum_{\beta=x}^{z} A_{\alpha\beta}(\mathbf{R}_{0n} - \mathbf{R}_{0m}, \mu\nu)\, u_{\nu\beta} e^{i\omega t} e^{i\mathbf{q}\cdot\mathbf{R}_{0n}}, \tag{2.29}$$

$$-\omega^2 M_\mu u_{\mu\alpha} e^{i\mathbf{q}\cdot\mathbf{R}_{0m}} = -\sum_n \sum_\nu \sum_{\beta=x}^{z} A_{\alpha\beta}(\mathbf{R}_{0n} - \mathbf{R}_{0m}, \mu\nu)\, u_{\nu\beta}\, e^{i\mathbf{q}\cdot\mathbf{R}_{0n}}, \tag{2.30}$$

$$\omega^2 M_\mu u_{\mu\alpha} = \sum_n \sum_\nu \sum_{\beta=x}^{z} A_{\alpha\beta}(\mathbf{R}_{0n} - \mathbf{R}_{0m}, \mu\nu)\, u_{\nu\beta}\, e^{i\mathbf{q}\cdot(\mathbf{R}_{0n} - \mathbf{R}_{0m})}. \tag{2.31}$$

Introducing $\mathbf{R}_{0h} \equiv \mathbf{R}_{0n} - \mathbf{R}_{0m}$, scaling the displacement of each ion by the square root of its mass:

$$w_{\nu\beta} \equiv \sqrt{M_\nu}\, u_{\nu\beta}, \tag{2.32}$$

and defining the matrix D by:

$$D_{\alpha\beta}(\mathbf{q}, \mu\nu) \equiv \frac{1}{\sqrt{M_\mu M_\nu}} \sum_h A_{\alpha\beta}(\mathbf{R}_{0h}, \mu\nu) e^{i\mathbf{q}\cdot\mathbf{R}_{0h}}, \tag{2.33}$$

we find the following eigenproblem:

$$\sum_\nu \sum_\beta \left[D_{\alpha\beta}(\mathbf{q}, \mu\nu) - \omega^2 \delta_{\alpha\beta} \delta_{\mu\nu}\right] w_{\nu\beta} = 0. \tag{2.34}$$

Here, δ_{ij} are the Dirac delta functions and the matrix D is called the dynamical matrix. Designating by S the number of atoms within a unit cell, there exist $3S$ solutions, called normal modes, each with a corresponding eigenvalue ω.

In practice, the dynamic matrix D can be calculated using a finite difference approach. The matrix elements $A_{\alpha\beta}(k,l)$ in Eq. (2.24) are expressed as:

$$A_{\alpha\beta}(k,l) \equiv \left.\frac{\partial^2 W}{\partial u_\alpha(k) \partial u_\beta(l)}\right|_{\{R_0\}} = \left.\frac{\partial F_\alpha(k)}{\partial u_\beta(l)}\right|_{\{R_0\}}, \tag{2.35}$$

hence A is referred to as the matrix of force constants. Its element $A_{\alpha\beta}(k,l)$ represents the change in the force acting on ion k in the direction α due to the displacement of nucleus l along β. In the finite difference scheme this first order derivative becomes:

$$\left.\frac{\partial F_\alpha(k)}{\partial u_\beta(l)}\right|_{\{R_0\}} \approx \frac{F[\mathbf{R}_{0l}-\delta_\beta]+F[\mathbf{R}_{0l}+\delta_\beta]}{2\delta_\beta} \tag{2.36}$$

where δ_β represents a small displacement in the direction β. For each atom in the unit cell, we displace it by $\pm\delta$ in each cardinal direction, and evaluate the forces between all ions by solving the Kohn-Sham equations in this perturbed configuration. This results in a total of $6S$ extra evaluations of the forces F. Additional symmetries of the force constant matrix can be exploited to further speed up the calculation of A, and hence of the dynamical matrix D as well.

2.2.3 Molecular Dynamics

To investigate the time evolution of a system, we can solve the equations of motion through discretization in time. Within the Born-Oppenheimer approximation, we can deal with the electrons using an *ab initio*, quantum mechanical description like DFT, while treating the nuclei as classical particles subject to Newton's Second Law. This approach is referred to as *ab initio* molecular dynamics (AIMD), or just MD. There are two common approaches to AIMD, the Born-Oppenheimer molecular dynamics (BOMD), and the Car-Parinello molecular dynamics (CPMD). In the BOMD, the electronic ground state is computed using DFT at each simulation step. The ground state electronic density is used to calculate the forces acting on the nuclei, and the position of the nuclei is updated in time in accordance with these forces. In the CPMD approach, the electrons collectively represent extra dynamical variables with fictitious masses. All nuclei and the electron density are propagated in time together, avoiding the need for the costly solution of Kohn-Sham equations at each simulation step.

Despite its name, it is the BOMD method that is implemented in CP2K. While the electron eigenproblem needs to be fully solved at each iteration, the time step of the simulation can be larger than in the case of CPMD, since only the heavy (thus slow) nuclei need to be evolved.[100] The equations of motion are integrated using the velocity Verlet algorithm.[101] The position $\mathbf{R}_k$ and velocity $\mathbf{V}_k$ of nucleus k are updated at each simulation step i according to:

$$\begin{aligned} \mathbf{R}_k^{i+1} &= \mathbf{R}_k^i + \mathbf{V}_k^i \delta t + \frac{\delta t^2}{2M_k}\mathbf{R}_k^i, \\ \mathbf{V}_k^{i+1} &= \mathbf{V}_k^i + \frac{\delta t}{2M_k}\left[\mathbf{F}_k^i + \mathbf{F}_k^{i+1}\right], \end{aligned} \qquad \forall k \in \{1,\dots,N_\mathrm{i}\} \tag{2.37}$$

where δt is the time step of the discretized equations of motion and M_k is the mass of the ion.

When simulating a canonical ensemble (fixed number of particles, volume, and temperature, hence also NVT ensemble), the choice of thermostat is important. Here we will introduce the Nosé-Hoover thermostat,[102] and its extension, the Nosé-Hoover chain method.[103] The Nosé-Hoover thermostat uses a friction term in order to control the velocities of the particles. This friction term is proportional to the one-dimensional momentum p_η of an extra degree of freedom η representing the thermal bath. The mass m_η corresponding to this degree of freedom is associated with the strength of the thermostat. The conserved quantity is the Hamiltonian:

$$H = W\{\mathbf{R}\} + \sum_{k=1}^{N_\mathrm{i}} \frac{\mathbf{P}_k^2}{2M_k} + \frac{p_\eta^2}{2m_\eta} + N_\mathrm{i} k_B T \eta, \tag{2.38}$$

where W is the effective ion potential, $\mathbf{P}$ are the momenta of the ions, $\mathbf{R}$ their positions, and N_i is their number. The system is subjected to the following set of equations of motion:[102]

$$\begin{aligned} \dot{\mathbf{R}}_k &= \frac{\mathbf{P}_k}{M_k}, \\ \dot{\mathbf{P}}_k &= \frac{\partial W}{\partial \mathbf{R}_k} - \mathbf{P}_k \frac{p_\eta}{m_\eta}, \\ \dot{\eta} &= \frac{p_\eta}{m_\eta}, \\ \dot{p}_\eta &= \sum_{k=1}^{N_\mathrm{i}} \frac{\mathbf{P}_k^2}{M_k} - N_\mathrm{i} k_B T. \end{aligned} \qquad \forall k \in \{1,\dots,N_\mathrm{i}\} \tag{2.39}$$

The Nosé-Hoover chain method is an improvement of the above approach. It consists of including M additional thermostat in the form of extra degrees of freedom η_m, each of which is linked only to its neighboring thermostats $\eta_{m\pm1}$. Relabeling η in Eqs. (2.39) by η_0, the Nosé-Hoover chains are characterized by the set of dynamical equations:[103]

$$
\begin{aligned}
\dot{\mathbf{R}}_k &= \frac{\mathbf{P}_k}{M_k}, \\
\dot{\mathbf{P}}_k &= \frac{\partial W}{\partial \mathbf{R}_k} - \mathbf{P}_k \frac{p_{\eta_0}}{m_{\eta_0}}, \\
\dot{\eta}_m &= \frac{p_{\eta_m}}{m_{\eta_m}} & \forall k \in \{1, \ldots, N_\mathrm{i}\} \\
\dot{p}_{\eta_0} &= \sum_{k=1}^{N_\mathrm{i}} \frac{\mathbf{P}_k^2}{M_k} - N_\mathrm{i} k_B T - p_{\eta_0} \frac{p_{\eta_1}}{m_{\eta_1}}, & \forall m \in \{1, \ldots, M\} \\
\dot{p}_{\eta_m} &= \frac{p_{\eta_{m-1}}^2}{m_{\eta_{m-1}}} - k_B T - p_{\eta_m} \frac{p_{\eta_{m+1}}}{m_{\eta_{m+1}}}, \\
\dot{p}_{\eta_M} &= \frac{p_{\eta_{M-1}}^2}{m_{\eta_{M-1}}} - k_B T.
\end{aligned}
\tag{2.40}
$$

Given a suitable choice of the dimensionless masses m_η, this thermostat ensures the ergodicity of the thermostated system.

2.3 Thermodynamic Integration

As discussed in Sec. 1.2, the current state-of-the-art, the CHE method, suffers from two major drawbacks. One, the effect of finite temperature is only taken into account in an approximate manner. Two, the inclusion of the solvent is not straightforward. The thermodynamic integration approach is a free energy method that relies on molecular dynamics simulations performed at finite temperature. Moreover, the solvent can be modeled explicitly, without the need for any further assumptions.

The Helmholtz free energy A of a classical canonical system at temperature T is given in terms of the partition function Z as:

$$A = -k_B T \ln Z. \tag{2.41}$$

The partition function is defined by:

$$Z \equiv \frac{1}{h^3} \iint e^{-\beta H} \mathrm{d}\mathbf{R}\mathrm{d}\mathbf{P}, \tag{2.42}$$

where $\beta \equiv (k_B T)^{-1}$, and H is the Hamiltonian, or total energy of the system. Consider now the free energy difference between a reactant and product state designated by R and P, respectively:

$$\Delta A \equiv A_P - A_R = -k_B T\big(\ln Z_P - \ln Z_R\big) = -\frac{1}{\beta}\ln\left[\frac{\iint e^{-\beta H_P}\mathrm{d}\mathbf{R}\mathrm{d}\mathbf{P}}{\iint e^{-\beta H_R}\mathrm{d}\mathbf{R}\mathrm{d}\mathbf{P}}\right]. \tag{2.43}$$

Defining $\Delta U \equiv H_P - H_R$ as the work required to achieve state P from the initial state R, this can further be simplified to:[104,105]

$$\Delta A = -\frac{1}{\beta}\ln\left\langle e^{-\beta\Delta U}\right\rangle_P \equiv \frac{1}{\beta}\ln\left\langle e^{\beta\Delta U}\right\rangle_R, \tag{2.44}$$

where the angled brackets represent the canonical average for the given state. During equilibrium simulations, the instantaneous configurations that contribute heavily to the exponents in Eq. (2.44) are high in energy, and thus rare, making it difficult to accurately sample them. A way to remedy this is through Kirkwood's coupling parameter method, wherein an effective Hamiltonian is constructed as a linear combination of the reactant and product states:[106]

$$H_\eta = (1-\eta)H_R + \eta H_P. \tag{2.45}$$

The derivative of the total energy with respect to Kirkwood's coupling parameter η is a vertical energy gap:

$$\frac{\partial H_\eta}{\partial \eta} \equiv \Delta E_0 \tag{2.46}$$

The free energy difference between the product and reactant state then becomes:

$$\Delta A(\eta) \equiv A(\eta = 1) - A(\eta = 0) \equiv \int_0^1 \frac{\mathrm{d}A}{\mathrm{d}\eta}\mathrm{d}\eta = \int_0^1 \langle \Delta E_0 \rangle_\eta \, \mathrm{d}\eta, \tag{2.47}$$

where $\langle \Delta E_0 \rangle_\eta$ is the canonical average of the vertical gap in the system defined by the mixed Hamiltonian of Eq. (2.45) for the given value of η. The physical interpretation of the vertical gap varies depending on the type of reaction. For example, in the case of a reaction involving the removal of a hydrogen, the vertical energy gap represents the potential energy difference between the initial state R and the state R with a hydrogen atom removed while keeping the rest of the configuration unchanged.[107]

2.4 Blue Moon

The Blue Moon ensemble method allows us to determine the free energy profile between an initial and a final configuration of a system from constrained molecular dynamics.[108] Suppose the transition from the initial to the final state is described by a single generalized coordinate ξ. A constrained molecular dynamics simulation is performed for each fixed value of ξ between the initial ξ_i and the final ξ_f value. The free energy at temperature T corresponding to such a process is:[109,110]

$$\Delta F = \int_{\xi_i}^{\xi_f} \mathrm{d}\xi \frac{\left\langle \mathcal{Z}^{-1/2}(\lambda + k_B T \mathcal{G}) \right\rangle_\xi}{\left\langle \mathcal{Z}^{-1/2} \right\rangle_\xi}, \tag{2.48}$$

where λ are the Lagrange coefficients corresponding to the constraint. The factor $\mathcal{G}$ is given by:

$$\mathcal{G} = \frac{1}{\mathcal{Z}^2} \sum_{k,l=1}^{N_\mathrm{i}} \frac{1}{M_k M_l} \frac{\partial \xi}{\partial \mathbf{R}_k} \cdot \frac{\partial^2 \xi}{\partial \mathbf{R}_k \partial \mathbf{R}_l} \cdot \frac{\partial \xi}{\partial \mathbf{R}_l}, \tag{2.49}$$

where M_k are the masses of the atoms, $\mathbf{R}_k$ their coordinates, and $\mathcal{Z}$ is a factor introduced to compensate the bias of the constraint:

$$\mathcal{Z} = \sum_{k=1}^{N_\mathrm{i}} \frac{1}{M_k} \left(\frac{\partial \xi}{\partial \mathbf{R}_k} \right)^2 . \tag{2.50}$$

If the reaction coordinate ξ is the distance between two atoms, then the factor $\mathcal{Z}$ is constant, and, moreover, $\mathcal{G} = 0$ on account of the second derivative. Hence, the free energy corresponding to a reaction parametrized solely by an interatomic distance is given by:

$$\Delta F = \int_{\xi_i}^{\xi_f} \mathrm{d}\xi \, \langle \lambda \rangle_\xi . \tag{2.51}$$

In practice, to calculate the free energy profile of a reaction, the procedure is as follows. A reaction coordinate, ideally an interatomic distance, is determined. Several values between the initial ξ_i and the final ξ_f value are chosen. For each fixed value of ξ a constrained molecular dynamics simulation is carried out. The Lagrange coefficients corresponding to the constraint are computed using the SHAKE algorithm.[111] Their average is then numerically integrated along ξ to obtain the free energy difference ΔF.

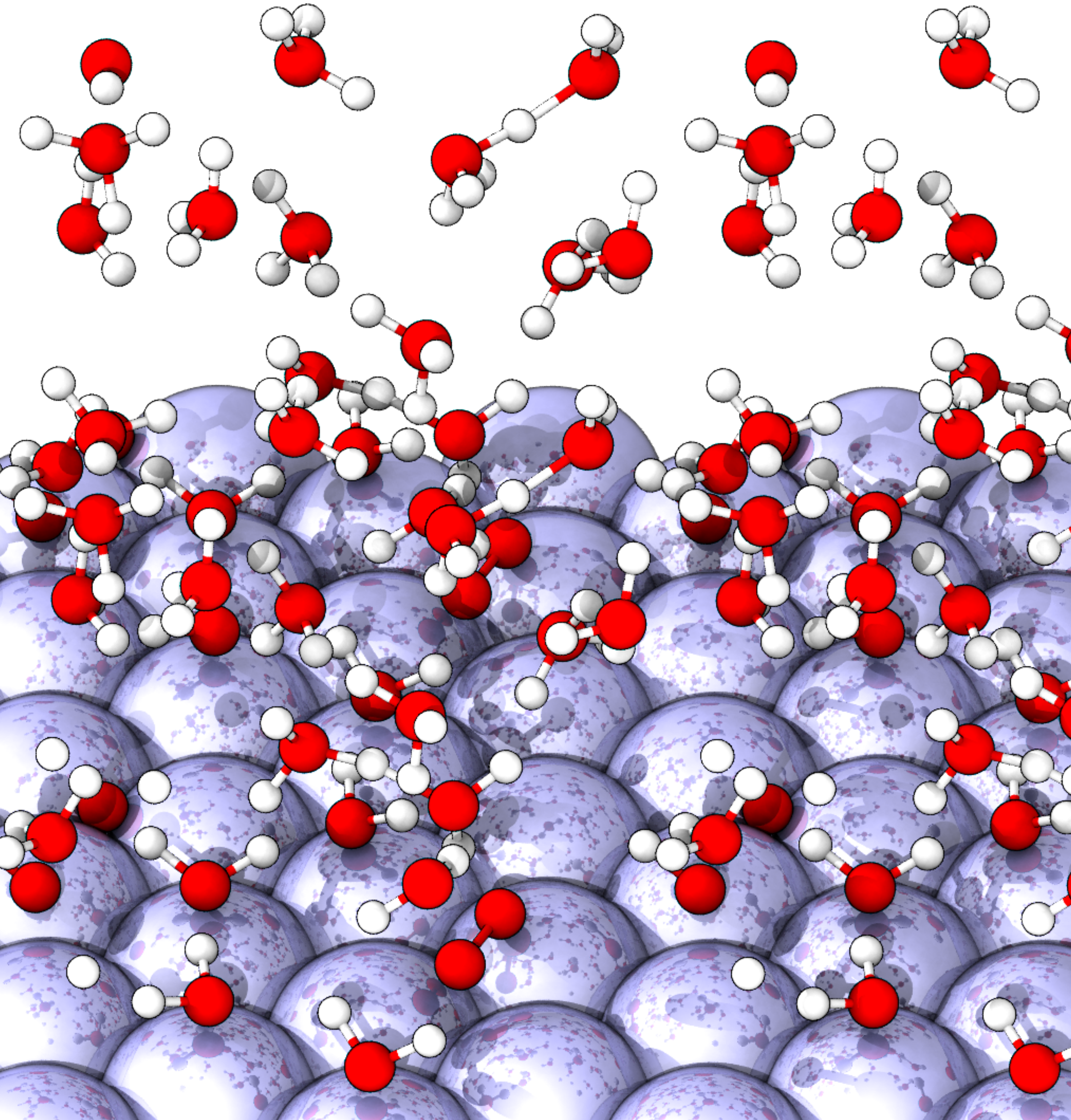

3 Computational Hydrogen Electrode

This chapter deals with the computational hydrogen electrode method. First, a detailed description of the CHE approach is provided. Next, the OER on a set of materials is studied via the CHE method. The emergence of linear scaling laws between the calculated free energy steps is observed. We then comment upon the choice of the energy functional by comparing results obtained at the semilocal and hybrid functional levels of theory. Irrespective of the functional used, linear scaling laws are found to occur. Finally, we use the CHE method to study different reaction intermediates observed under potential bias on the surface of a platinum electrode. We find that the CHE approach can be used in conjunction with an exploratory scheme to validate the viability of the observed reaction mechanism.

The results presented in this chapter have been published in Refs. [50] and [112].

Left: A snapshot of the platinum surface covered by a layer of water.

3.1 Formulation of the Computational Hydrogen Electrode Method

The CHE method for the calculation of Gibbs free energies corresponding to PCET reactions is here outlined.[31] Using the RHE as a reference, at the conditions of $P = 10^5$ Pa, $T = 298$ K, and any pH, the free energy of the reaction:

$$\mathrm{H}^+ + e^- \longleftrightarrow \tfrac{1}{2}\mathrm{H}_{2(\mathrm{g})} \tag{3.1}$$

is set to zero, and therefore we write:[113,114]

$$\mu[\mathrm{H}^+] + \mu[e^-] = \tfrac{1}{2}\mu[\mathrm{H}_{2(\mathrm{g})}]. \tag{3.2}$$

In effect, the chemical potential of the proton-electron pair is replaced with the computationally more accessible chemical potential of gaseous hydrogen. The Gibbs free energy difference corresponding to a PCET reaction:

$$A \longrightarrow B + \mathrm{H}^+ + e^- \tag{3.3}$$

can then be expressed as:

$$\Delta G_{AB} = \mu[B] - \mu[A] + \tfrac{1}{2}\mu[\mathrm{H}_{2(\mathrm{g})}]. \tag{3.4}$$

The chemical potentials of species A and B can in turn be approximated by:[115]

$$\mu = E^{\mathrm{DFT}} + \mathrm{ZPE} - TS + \Delta U^{0\to T}, \tag{3.5}$$

where E^{DFT} is the total DFT energy of the system, and ZPE is the zero point energy of the adsorbed or free species calculated in the harmonic approximation. T is the desired temperature. $\Delta U^{0\to T}$ represents the internal energy change between 0 K and the temperature T. For the free species (gaseous or liquid, i.e. not adsorbed), the entropy S consists of vibrational, rotational, and translational contributions:

$$\mu = E^{\mathrm{DFT}} + \mathrm{ZPE} - T\left(S^{\mathrm{vib}} + S^{\mathrm{rot}} + S^{\mathrm{trans}}\right) + \Delta U^{0\to T}, \tag{3.6}$$

whereas in the case of adsorbed species all degrees of freedom are assumed to be vibrational and thus only the vibrational entropy contribution remains:

$$\mu = E^{\text{DFT}} + \text{ZPE} - TS^{\text{vib}} + \Delta U^{0\to T}. \tag{3.7}$$

The changes in the vibrational spectrum of the slab upon the adsorption of a molecule are neglected.[34] Therefore, in the vibrational analysis the substrate is kept fixed, and only the vibrational spectrum of the adsorbed molecule is evaluated.

The various correction terms mentioned above are calculated as:[116]

$$\text{ZPE} = \tfrac{1}{2}\sum_{\omega} \hbar\omega, \tag{3.8}$$

$$S^{\text{vib}} = R\sum_{\omega}\left(\frac{\hbar\omega}{k_B T\left[\exp\left(\frac{\hbar\omega}{k_B T}\right)-1\right]} - \ln\left[1-\exp\left(-\frac{\hbar\omega}{k_B T}\right)\right]\right), \tag{3.9}$$

$$S^{\text{trans}} = R\ln\left[\left(\frac{2\pi m k_B T}{h^2}\right)^{3/2}\frac{k_B T}{P}\right] + \tfrac{5}{2}R, \tag{3.10}$$

$$S^{\text{rot}} = \begin{cases} R\ln\left(\dfrac{8\pi^2 k_B T I}{h^2\sigma}\right) + R, & \text{for linear molecules} \\ R\ln\left[\left(\dfrac{8\pi^2 k_B T}{h^2}\right)^{3/2}\dfrac{\sqrt{\pi I_1 I_2 I_3}}{\sigma}\right] + \tfrac{3}{2}R, & \text{for non-linear molecules} \end{cases} \tag{3.11}$$

$$\Delta U^{0\to T} = R\sum_{\omega}\frac{\hbar\omega}{k_B\left[\exp\left(\frac{\hbar\omega}{k_B T}\right)-1\right]}, \tag{3.12}$$

where ω are the frequencies calculated in the harmonic approximation, R is the universal gas constant, I_i are the moments of inertia, and σ is the symmetry number representing the number of equivalent orientations of the molecule.

Instead of the RHE, which is defined for any pH, the standard hydrogen electrode (SHE) is often used as the reference electrode. The SHE represents the potential under which the reaction Eq. (3.2) is reversible at pH = 0. By construction, the DFT calculations of the reaction intermediates are carried out at the pH of zero charge pH_{pzc}. Hence, if instead of the RHE we want to use the SHE as the reference, the chemical potential in Eq. (3.5) must be modified by a correction that corresponds to the difference in the pH:[17,117]

$$\mu^{\mathrm{SHE}} = E^{\mathrm{DFT}} + \mathrm{ZPE} - TS + \Delta U^{0\to T} + \Delta E^{\mathrm{pH}}. \tag{3.13}$$

Assuming the reaction given in Eq. (3.3) is Nernstian, the correction is given by:[114]

$$\Delta E^{\mathrm{pH}} = 0.059 \cdot \left(\mathrm{pH}_0 - \mathrm{pH}_{\mathrm{pzc}}\right)\ \mathrm{eV}, \tag{3.14}$$

where the reference $\mathrm{pH}_0 \equiv 0$ in the case of the SHE. However, unless stated otherwise, we will use the RHE as the reference electrode due to its convenience.

3.2 Linear Scaling Relationships

We use the CHE method to calculate the OER free energy steps for the reaction mechanism given by Eqs. (1.2). The following interfaces are studied: rutile $TiO_2(110)$, anatase $TiO_2(101)$, $SnO_2(110)$, $RuO_2(110)$, $IrO_2(110)$, $Ni_2P(0001)$, $BiVO_4(001)$, γ-FeOOH(100), and ZnO(10$\bar{1}$0). For each of these surfaces, the free energy steps ΔG_i, $i \in \{1,2,3,4\}$ are computed. This allows us to investigate the scaling laws that exist between the free energy values within the studied set of materials.

3.2.1 Computational Details

All material surfaces are modeled by periodic, orthogonal slabs separated by 20 Å of vacuum in the direction perpendicular to the surface (see Table 3.1). The lattice parameters of the slabs are determined through lattice optimizations of bulk supercells. In the case of SnO_2, however, the experimental lattice parameters are used following Guo *et al.*[118] This choice is motivated by the fact that the calculated energy levels are very sensitive to small deviations in lattice parameters on account of the high deformation potential of SnO_2.[119] In each case, the number of layers is chosen so as to achieve bulk-like properties in the center of the slab.

The cutoff for the density is set to 600 Ry. No constraints are imposed on the atoms in the geometry optimization calculations. The revised PBE (RPBE) functional[86] is used to obtain optimized geometries and binding energies of the reaction intermediates. Triple-ζ MOLOPT basis sets[93] and Goedecker-Teter-Hutter pseudopotentials[120] are used for all elements.

The thermodynamic corrections corresponding to the same reaction intermediates at different surfaces are assumed to be identical. The zero point energies ZPE, entropy corrections TS, and internal energy contributions used in the calculations of the chemical potentials of the reaction intermediates are listed in Table 3.2.

The RPBE functional yields a free energy difference of $\Delta G_{\mathrm{OER}} = 4.00$ eV for the overall OER:

$$2\,\mathrm{H_2O}_{(\ell)} \longrightarrow \mathrm{O}_{2(\mathrm{g})} + 2\mathrm{H}_{2(\mathrm{g})}, \tag{3.15}$$

This value is considerably lower than the experimental reference $\Delta G_{\mathrm{OER}} = 4.92$ eV.

Table 3.1 – From left to right: supercell sizes L_x and L_y in the x and y directions chosen to lie perpendicular to the surface normal, number of layers, and total number of atoms used in the slab model for each material.

System	L_x (Å)	L_y (Å)	Periodicity	Layers	Atoms
$SnO_2(110)$	13.405	12.740	2×4	5	240
$IrO_2(110)$	12.870	12.709	2×4	5	240
$RuO_2(110)$	12.978	12.467	2×4	5	240
r-$TiO_2(110)$	13.286	12.054	2×4	5	240
$BiVO_4(001)$	10.592	10.351	2×2	3	144
a-$TiO_2(101)$	10.522	11.431	2×3	6	180
$Ni_2P(0001)$	11.744	10.250	2×3	6	196
$ZnO(10\bar{1}0)$	10.673	9.998	2×3	6	144
FeOOH(100)	13.994	11.542	2×4	3	192

This discrepancy is commonly attributed to the inability of the semilocal functional in describing the O_2 intermediate.[31] The conventional workaround consists in modifying the total energy of (gas phase) O_2. Hence, a correction of 0.92 eV is added to the fourth free energy steps in Eqs. (1.2) involving O_2, in accordance with common practice.[24,33,41] This ensures that the overall reaction free energy ΔG_{OER} agrees with the experimental value. However, this correction assumes all the error associated with the use of the adopted functional is solely contained in the fourth free energy step ΔG_4. This might not necessarily be the case in reality.

3.2.2 Results

For each material in the studied set we calculate the free energy steps corresponding to the regular OER mechanism in Eqs. (1.2). The calculated values are shown in Table 3.3. Where the comparison with previous calculations can be made, our results show good agreement.[23,24,33,36,41,121] Man *et al.*[23] found that the values of ΔG_2 and ΔG_3 are linearly correlated, the value of ΔG_3 being given by $\Delta G_3 \approx 3.2\,\mathrm{eV} - \Delta G_2$. Figure 3.1(a) demonstrates that such scaling laws are observed in our calculations as well. In particular, upon performing a linear regression, we find that the intercept with the vertical axis has a value of 3.0 ± 0.3 eV, which is in reasonable agreement with the literature value of 3.2 eV. As discussed in the Introduction (see Sec. 1.1), this gives rise to an overpotential on at least one of the two free energy steps

Table 3.2 – From left to right: Zero point energy ZPE, entropy correction TS, internal energy contribution $\Delta U^{0\to T}$, and total correction ΔE_{corr} defined as $\Delta E_{\text{corr}} \equiv \text{ZPE} - TS + \Delta U^{0\to T}$. All values are in eV.

Species	ZPE	TS	$\Delta U^{0\to T}$	ΔE_{corr}
$H_{2(g)}$	0.19	−0.42	0.10	−0.13
$H_2O_{(\ell)}$	0.55	−0.65	0.10	−0.00
$O_{2(g)}$	0.07	−0.59	0.10	−0.42
OH_{ads}	0.37	−0.06	0.04	0.35
O_{ads}	0.08	−0.04	0.03	0.06
OOH_{ads}	0.47	−0.14	0.08	0.41
H_{ads}	0.30	−0.01	0.01	0.29

involved. Defining the OER overpotential as $\eta \equiv \max_i \{\Delta G_i - 1.23\}$ for $i \in \{1,2,3,4\}$, we can plot it as a function of the second free energy step ΔG_2. This leads to the volcano plot shown in Fig. 3.1(b). The top of the volcano represents the lowest attainable overpotential. Given the scaling relationship $\Delta G_2 + \Delta G_3 = 3.2$ eV, the minimum overpotential $\eta = (3.2 - 2 \times 1.23)/2$ eV $= 0.37$ eV occurs for $\Delta G_2 = 1.6$ eV. The overpotential for materials situated on the right slope ($\Delta G_2 > 1.6$ eV) is generally dominated by ΔG_2, whereas for those on the left slope ($\Delta G_2 < 1.6$ eV) it is generally dominated by the third free energy step ΔG_3.

Table 3.3 – The free energy steps ΔG_i obtained using the RPBE functional. All values are in eV.

Surface	ΔG_1	ΔG_2	ΔG_3	ΔG_4
$SnO_2(110)$	1.78	2.40	0.34	0.41
$IrO_2(110)$	0.05	1.07	1.89	1.91
$RuO_2(110)$	0.71	0.79	2.11	1.30
r-$TiO_2(110)$	1.92	2.10	0.34	0.57
$BiVO_4(001)$	2.69	2.35	−0.10	−0.02
a-$TiO_2(101)$	2.55	2.37	−0.10	0.11
$Ni_2P(0001)$	0.83	1.31	1.76	1.02
$ZnO(10\bar{1}0)$	1.88	2.25	−0.06	0.85
FeOOH(100)	1.70	1.49	0.04	1.70

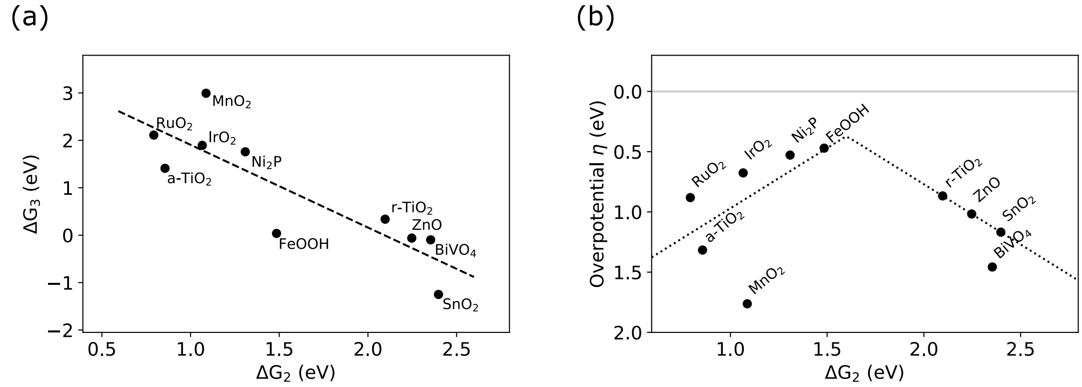

Figure 3.1 – (a) Linear scaling relationship between the free energies corresponding to the second and third OER steps following the mechanism in Eqs. (1.2). (b) Volcano plot depicting the OER overpotential η as a function of the second free energy step ΔG_2. The dotted line is defined by $\max\{\Delta G_2 - 1.23, 3.2 - \Delta G_2 - 1.23\}$. Note that the vertical axis is inverted, and thus the apex of the curve exhibits the lowest overpotential.

We find that r-TiO_2, ZnO, and SnO_2 are limited by ΔG_2, and thus lie directly on the right slope of the volcano in Fig. 3.1(b). The materials Ni_2P, RuO_2, and MnO_2 are instead limited by the third OER step ΔG_3, and are thus found on the left slope. The other materials exhibit the highest overpotential on either the first or the fourth free energy step, but can still be seen to conform to the shape of the volcano.

3.3 Hybrid Functional Level of Theory

It is well known that semilocal functionals, such as RPBE, fail at accurately describing the electronic structure and the charge localization in the case of semiconductors and insulators. Furthermore, the use of an *ad-hoc* correction for the O_2 energy is unsatisfactory and it is unclear how this correction might affect the achieved results. To address these issues, we have set out to repeat all RPBE calculations in Sec. 3.2 using hybrid functionals.

3.3.1 Computational Details

The hybrid functional calculations employ a modified PBE0(α) functional[88] in the case of semiconductors, and a modified HSE06(α) functional[90,122] in the case of metals (IrO_2, RuO_2). The fraction of exact exchange α that leads to the experimental value of $\Delta G_{\mathrm{OER}} = 4.92$ eV is found to be $\alpha = 0.29$ in the case of PBE0 and $\alpha = 0.305$ in the case of HSE06. When proceeding with the same rationale as in the case of the semilocal RPBE functional, this implies that no further *ad-hoc* correction is needed to account for the O_2 molecule with these hybrid functionals. While this does not signify that the energy of the O_2 molecule is perfectly captured within such a scheme, it nevertheless provides us with the possibility of examining the robustness of our RPBE results through the use of more advanced functionals.

A full geometry optimization of each studied interface with each reaction intermediate is carried out. Due to the inherently larger computational cost of hybrid functionals, only double-ζ quality basis sets are used. The smaller basis set size is found to modify total energy differences by less than 0.1 eV in selected cases. We use the auxiliary density matrix method[97] in conjunction with double-ζ quality auxiliary basis sets to improve the performance of the calculations.

The configurations of reaction intermediates achieved at the hybrid functional level of theory are similar to those obtained using RPBE. Hence, we assume the modification of the vibrational modes is negligible, and thus use the same thermodynamic corrections calculated at the semilocal level (see Table 3.2).

3.3.2 Results and Discussion

The free energy steps corresponding to the reactions in Eqs. (1.2) calculated at the hybrid functional level of theory are given in Table 3.4. The comparison of the results achieved with hybrid functionals and the RPBE results achieved in Sec. 3.2 is shown in Fig. 3.2 for a selection of the studied materials. The results obtained with the two theoretical schemes differ quite noticeably in quantitative terms. For instance, ΔG_3 in the case of of Ni_2P changes from ~1.8 eV with RPBE to ~2.4 eV with the hybrid functional. In the case of IrO_2, we even observe a qualitative change with the rate limiting step shifting from ΔG_4 with RPBE to ΔG_2 with hybrid functionals.

Table 3.4 – The free energy steps ΔG_i obtained using hybrid functionals. All values are in eV.

Surface	ΔG_1	ΔG_2	ΔG_3	ΔG_4
SnO_2(110)	1.89	2.52	0.59	−0.06
IrO_2(110)	0.48	1.91	0.99	1.56
RuO_2(110)	2.73	0.23	1.89	0.10
r-TiO_2(110)	2.40	2.87	−0.50	0.17
$BiVO_4$(001)	2.92	2.84	−0.23	−0.60
a-TiO_2(101)	2.64	2.65	0.03	−0.38
Ni_2P(0001)	0.18	0.39	2.41	1.95
FeOOH(100)	−0.85	2.74	0.81	2.23

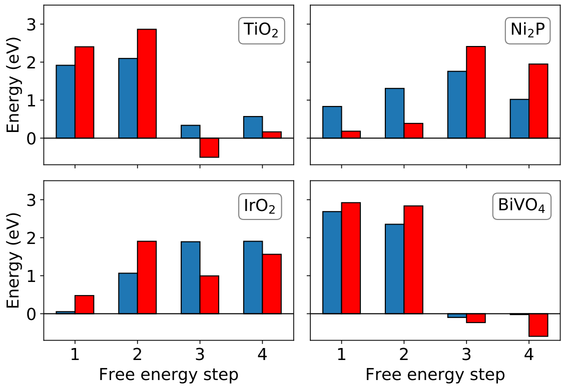

Figure 3.2 – Free energy steps ΔG_i, $i \in \{1,2,3,4\}$, corresponding to the regular OER mechanism in Eqs. (1.2) for four materials. Results obtained using RPBE and hybrid functionals are shown in blue and red, respectively.

The changes between RPBE and hybrid functional results also reflect in Fig. 3.3(b), leading to noticeable differences in both the values of ΔG_2 and η found for the individual materials when compared to Fig. 3.1(b). In particular, the order of the materials according to ΔG_2 is not preserved. All materials except Ni_2P, RuO_2, and $BiVO_4$ are found to be limited by the second free energy step ΔG_2, and thus lie on the right slope of the volcano, which corresponds to the dotted line for $\Delta G_2 > 1.6$ eV in Fig. 3.3(b). Out of these three exceptions, only Ni_2P is limited by ΔG_3. Nevertheless, the calculated overpotentials are consistent with the linear scaling relationship even at the hybrid functional level, as can be seen in Fig. 3.3(a). The second and third free energy steps ΔG_2 and ΔG_3 are related through the expression $\Delta G_2 + \Delta G_3 = 2.5\ \text{eV} \pm 0.2\ \text{eV}$. Due to the limited size of the studied set of materials, outliers have a strong influence on the calculated offset in the linear scaling relationship. Therefore, we resort to the literature value of 3.2 eV when constructing the volcano plot in Fig. 3.3(b).

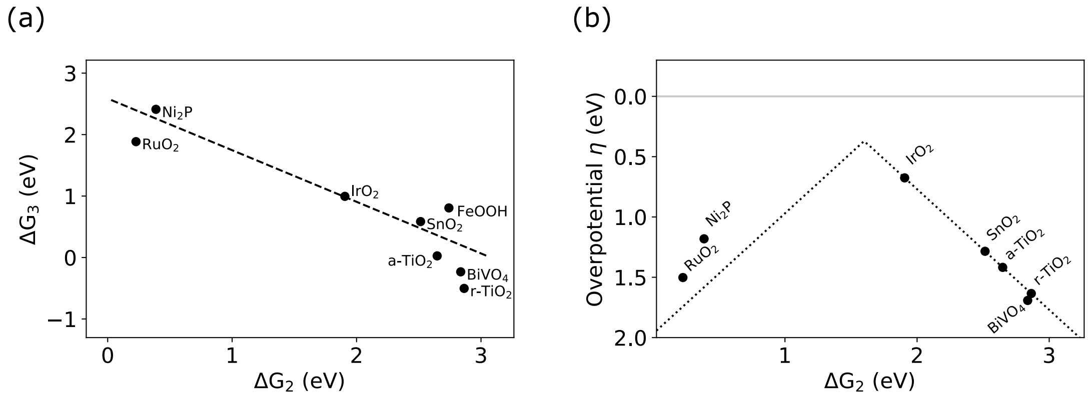

Figure 3.3 – (a) Linear scaling relationships between the free energies corresponding to the second and third OER step following the mechanism in Eqs. (1.2). (b) Volcano plot depicting the OER overpotential η as a function of the second free energy step ΔG_2. The dotted line is defined by $\max\{\Delta G_2 - 1.23, 3.2 - \Delta G_2 - 1.23\}$. Note that the vertical axis is inverted, and thus the apex of the curve exhibits the lowest overpotential.

We note that the results obtained at the semilocal level of theory are in better agreement with previous literature, both in qualitative as well as in quantitative terms.[23,24,33,36,41,121] In particular, the order of the materials in Fig. 3.3(b) achieved using hybrid functionals is different than in the case of the RPBE functional [see Fig. 3.1(b)], resulting in the erroneous assessment of the relative performance of the studied catalysts. Moreover, at the hybrid functional level of theory, the predicted reaction determining step for some materials is different than the one identified using semilocal functionals. Such large differences upon adoption of hybrid functionals have been noted before.[49,123] Nevertheless, the linear scaling is still present at both levels of theory, further supporting previous findings of its robustness with respect to the choice of DFT functional.[32]

3.4 The OER Mechanism on the Platinum Electrode under Potential Bias

In this section we exemplify the use of the CHE approach as a means of confirming and complementing the results of an exploratory computational technique. The results presented here are part of the work published by Bouzid *et al.* in Ref. [112]. In this study, a constant Fermi level molecular dynamics scheme is employed to simulate the Pt(111) interface with liquid water under a potential bias. This method allows one to fix the value of the Fermi level by adopting a grandcanonical potential. The charge is allowed to fluctuate in order to satisfy the constant Fermi level condition, leading to an effective potential bias. By modifying the preset value of the Fermi level, the effective potential bias is varied and different electrochemical regimes are investigated. Under these conditions, the oxygen evolution reaction is found to take place spontaneously via an unexpected reaction mechanism. We use the CHE method to verify the viability of this reaction scheme, and investigate its performance with respect to the commonly adopted mechanism:

$$\begin{aligned} \mathrm{H_2O}_{(\ell)} &\longrightarrow \mathrm{OH_{ads}} + \mathrm{H^+} + e^-, \\ \mathrm{OH_{ads}} &\longrightarrow \mathrm{O_{ads}} + \mathrm{H^+} + e^-, \\ \mathrm{O_{ads}} + \mathrm{H_2O}_{(\ell)} &\longrightarrow \mathrm{OOH_{ads}} + \mathrm{H^+} + e^-, \\ \mathrm{OOH_{ads}} &\longrightarrow \mathrm{O}_{2(\mathrm{g})} + \mathrm{H^+} + e^-. \end{aligned} \tag{3.16}$$

3.4.1 Observations from Constant Fermi Level Molecular Dynamics

To model the solvated platinum electrode under OER conditions, the constant Fermi level MD method was applied to a periodic platinum/water interface. The Pt slab consisted of three layers of 12 Pt atoms each. Two identical surfaces with a $3 \times \sqrt{3}$ surface repeat unit were exposed to a water layer consisting of 32 water molecules. By modifying the Fermi level, an effective potential bias was applied to the studied system. The potential bias was gradually increased in a step-wise manner until the OER was observed to take place spontaneously. Figure 3.4 shows the time evolution of the distance between the oxygen atoms of the two adjacent species participating in the O_2 formation. The creation of the O_2 bond concluded the observed OER. By analyzing the obtained trajectory, the following mechanism was observed. After around 10 ps, an adsorbed water molecule loses one of its hydrogen atoms, forming

OH_{ads}. Next, this OH_{ads} reacts with an adjacent OH_{ads} initially present on the Pt surface, forming an $H_2O_{2\,ads}$ intermediate. One hydrogen is released and OOH_{ads} forms. Eventually, the second hydrogen is released as well, leaving behind $O_{2\,ads}$ on the Pt surface:

$$\begin{aligned} H_2O_{(\ell)} &\longrightarrow OH_{ads} + H^+ + e^-, \\ OH_{ads} + H_2O_{(\ell)} &\longrightarrow OH_{ads} + OH_{ads} + H^+ + e^-, \\ OH_{ads} + OH_{ads} &\longrightarrow H_2O_{2\,ads} \longrightarrow OOH_{ads} + H^+ + e^-, \\ OOH_{ads} &\longrightarrow O_{2(g)} + H^+ + e^-. \end{aligned} \tag{3.17}$$

At variance with the commonly adopted reaction mechanism in Eqs. (3.16), no O_{ads} intermediate is observed. Instead, $H_2O_{2\,ads}$ forms as a reaction intermediate.

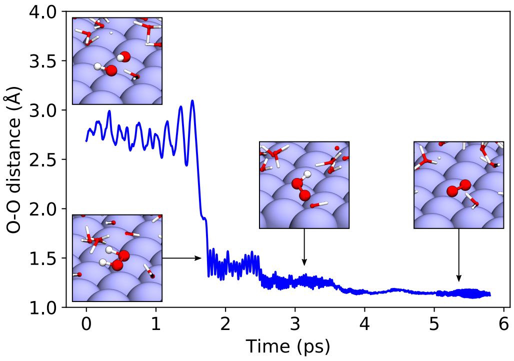

Figure 3.4 – The distance between the oxygen atoms of an initially adsorbed water molecule and of a neighboring OH group. The insets illustrate the evolution of the two adsorbates over the duration of the MD simulation.

3.4.2 Results and Discussion

While the trajectory obtained from the constant Fermi level MD simulation shows the OER taking place, it is unclear whether the observed reaction mechanism is thermodynamically favored with respect to the standard mechanism. The effective potential employed to drive the reaction on the short time scales conducive to AIMD does not correspond to the potential bias under real OER conditions. Hence, to allow for a meaningful comparison with previous work, the stability of all intermediates and the free energy steps corresponding to both the observed and the standard mechanism are evaluated under neutral charge conditions.

We employ the CHE approach to investigate the relative stability of the intermediates and to calculate the OER overpotentials for both reaction mechanisms. The Pt(111)/vacuum interface is modeled by an orthogonal slab consisting of 36 platinum atoms. Adopting common practice, the effect of the solvent is neglected. All reaction intermediates are fully relaxed, and the vibrational modes of the adsorbates are calculated in order to evaluate the thermodynamic corrections. The same modified rVV10 functional is used as in the case of the constant Fermi level MD.[124–126] We employ an energy cutoff of 700 Ry for the basis of the plane wave representation of the electron density. Triple-ζ quality MOLOPT[93] basis sets in conjunction with Goedecker-Tetter-Hutter pseudopotentials[120] are used for all elements. At least 20 Å of vacuum separate the periodic images of the slabs in the direction perpendicular to the interface.

Table 3.5 – From left to right: total DFT energy, zero point energy ZPE, entropy correction TS, internal energy contribution $\Delta U^{0\to T}$, and total correction ΔE_{corr} defined as $\Delta E_{\mathrm{corr}} \equiv \mathrm{ZPE} - TS + \Delta U^{0\to T}$. The total energy of adsorbed species is given with respect to the clean surface. All values are in eV.

	ZPE	TS	$\Delta U^{0\to T}$	ΔE_{corr}
$H_{2(g)}$	0.264	0.422	0.101	−0.057
$H_2O_{(\ell)}$	0.561	0.652	0.101	0.010
$O_{2(g)}$	0.095	0.590	0.101	−0.394
OH_{ads}	0.357	0.093	0.048	0.312
O_{ads}	0.089	0.031	0.021	0.079
OOH_{ads}	0.428	0.107	0.066	0.387
$OH_{\mathrm{ads}} + OH_{\mathrm{ads}}$	0.744	0.109	0.071	0.706

The calculated free energy steps are shown in Fig. 3.5, and Table 3.5 lists the thermodynamic corrections for all reaction intermediates and the binding energies for the adsorbed ones. We find that the O_{ads} intermediate, present only in the regular mechanism, is bound strongly at the Pt surface, thus leading to a large overpotential in the third reaction step (OOH_{ads} formation). At variance, in the proposed reaction mechanism in Eqs. (3.17) the formation of this intermediate proceeds from $H_2O_{2\,\mathrm{ads}}$. As a result, the overpotential on the third reaction step is lower by about 0.2 eV with respect to the regular mechanism.

In summary, we used the CHE approach to calculate the OER free energy steps associated with a reaction mechanism observed through constant Fermi level MD. The spontaneous O_2 formation avoids the O_{ads} intermediate, instead relying on the

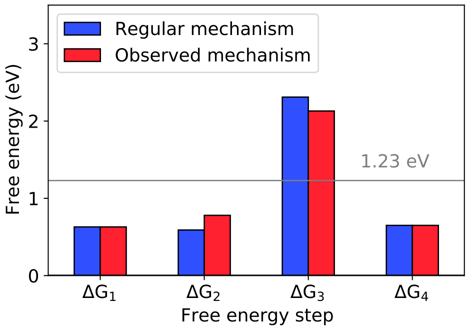

Figure 3.5 – Comparison of the free energy steps ΔG_i achieved with the regular OER mechanism is Eqs. (1.2) and with the mechanism proposed in Eqs. (3.17).

reaction of two nearby OH_{ads} adsorbates. The CHE method successfully predicted a lower overpotential in the case of the observed mechanism as compared to the commonly adopted one.

3.5 Conclusion

In this chapter we provide a comprehensive overview of the CHE method, and present several applications. The CHE approach is used to showcase the emergence of the linear scaling relationship between the free energy steps corresponding to a regularly adopted four PCET OER mechanism. This linear scaling is found to persist upon the adoption of the more advanced hybrid functionals.

An important finding is the emergence of a linear scaling relationship between the second and third free energy step corresponding to the regular OER mechanism. This scaling law places a lower limit on the achievable OER overpotential, thus limiting the catalytic efficiency of large classes of materials. We verified the robustness of the scaling relationship with respect to the choice of functional by performing all calculations both at the semilocal as well as the hybrid functional level of theory. Regardless of the functional used, the free energy steps involved in the linear scaling law were found to be correlated for a set of catalysts.

The CHE method is a free energy method based on static DFT calculations of the reactant and product systems. These DFT energies are augmented by thermodynamic corrections that can be achieved through a vibrational analysis. As discussed in Sec. 1.1, this approach models temperature effects only in an approximate fashion, and the presence of the solvent is often neglected. However, only the differences between free energies are of interest, and hence the cancellation of errors inherent in this scheme leads to results that are generally consistent with more advanced computational approaches or experiments. The validity of this assumption is supported by the case of the platinum electrode under potential bias. Here, the results obtained using CHE for a vacuum interface under neutral conditions are in qualitative agreement with the results obtained at a fully atomistic Pt/water interface at finite temperature under effective potential bias. Given the low computational cost, this makes the CHE method a versatile and robust state-of-the-art approach in the field of electrochemistry and catalysis. Nevertheless, the effect of finite temperature and the presence of the solvent, both of which are insufficiently addressed within the CHE scheme, are worth being examined in more detail and will be the subject of the following chapter.

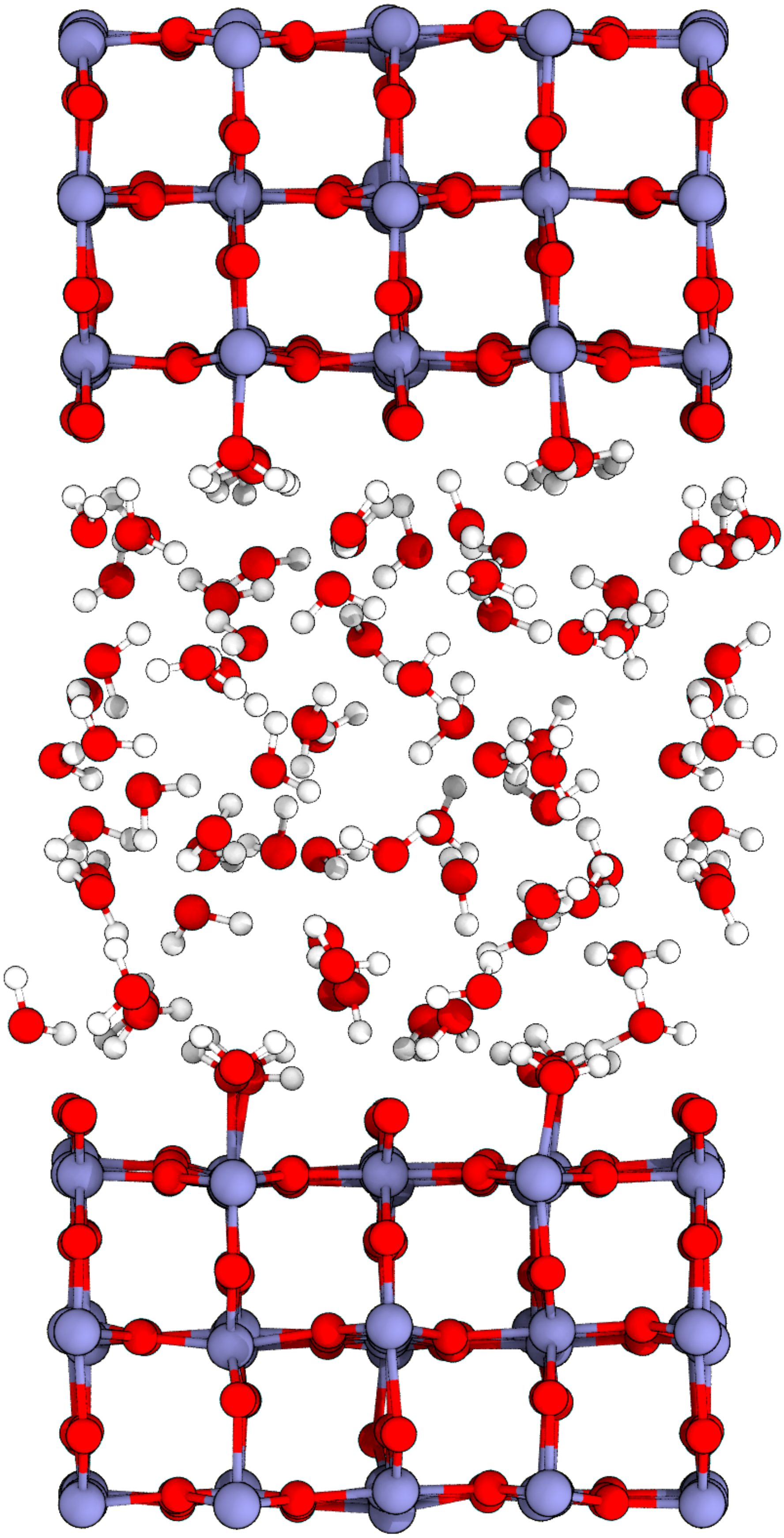

4 Effect of Solvent on the Oxygen Evolution Reaction on TiO_2

In this chapter, we investigate the role of the solvent in determining the OER free energy steps on rutile TiO_2. Titanium dioxide is chosen on account of its status as a benchmark material in connection with photocatalysis.[127] From a computational point of view, its relevant properties have been studied both in the absence[33,128,129] and in the presence of the solvent. In the latter case, models ranging from frozen water monolayers on the one hand,[130,131] to fully explicit water layers at finite temperature on the other hand,[51,132,133] have been considered in the past. The presence of explicit water was found to be of importance, both directly and indirectly, in the detailed process of water splitting.[134–136] Ultimately, Cheng *et al.* succeeded in evaluating the OER free energy steps in the presence of fully explicit water molecules at finite temperature.[46] However, it was not possible to isolate the effect of the solvent, and the detailed mechanism of the interaction between the reaction intermediates and liquid water molecules was not addressed. Therefore, it is our goal to model the OER both in the presence and in the absence of water, and to identify in this way the effect on the relevant free energy steps.

To calculate the free energy steps in the presence of the fully explicit solvent, an approach based on AIMD and thermodynamic integration is developed. The effect of the solvent is isolated by performing free energy calculations of the OER steps both at the solvated and at the vacuum rutile interface. The same free energies are evaluated at the level of the CHE method, which ignores the solvent and treats entropy effects only approximately. This approach allows us to quantify the effect of the solvent on the energetics of the OER.

Left: Illustration of the rutile TiO_2 interface with explicit water.

First, the TI approach used to calculate the free energies corresponding to the PCET steps of the OER is described. Next, computational details of all methods used throughout this chapter are given. The results of the TI calculations are presented, the effect of the solvent isolated, and a comparison with the CHE results is drawn. We investigate two possible explanations of the observed solvent effect, a structural and an electrostatic hypothesis. Finally, having addressed the origin of the effect of the solvent, we model the full OER pathway in the presence and in the absence of the solvent.

The results presented in this chapter have been published in Ref. [137].

4.1 OER Free Energies through Thermodynamic Integration

To calculate the free energy of a PCET reaction using the thermodynamic integration method we resort to the scheme employed in the CHE approach. The chemical potential of the proton-electron pair is replaced by one half of the chemical potential of hydrogen gas. The free energy of a reaction of the form:

$$R \longrightarrow P + \mathrm{H}^+ + e^-, \tag{4.1}$$

where the product P and reactant R differ by a single hydrogen atom, is hence calculated as:

$$\Delta G = \mu[P] - \mu[R] + \tfrac{1}{2}\mu[\mathrm{H}_{2(\mathrm{g})}]. \tag{4.2}$$

A mixed Hamiltonian is set up as a linear combination of the reactant and product Hamiltonians:

$$H = (1-\eta)H_R + \eta H_P, \tag{4.3}$$

where η is the Kirkwood mixing parameter, a real number between 0 and 1. For each value of η, an *ab-initio* molecular dynamics simulation with the mixed Hamiltonian is carried out. The vertical dehydrogenation energy $\langle \Delta_{\mathrm{dh}} E \rangle_\eta$ is calculated as the average difference between the total energies of the product and the reactant systems. Integrating the vertical dehydrogenation energy in η we obtain, following Eq. (2.47), the dehydrogenation free energy:[45]

$$\Delta_{\mathrm{dh}} A \equiv \int_0^1 \langle \Delta_{\mathrm{dh}} E \rangle_\eta \, \mathrm{d}\eta. \tag{4.4}$$

The free energy of the PCET step in Eq. (4.2) then becomes:

$$\Delta G = \Delta_{\mathrm{dh}} A + \tfrac{1}{2}\mu[\mathrm{H}_{2(\mathrm{g})}], \tag{4.5}$$

where the chemical potential of the hydrogen gas is calculated using the CHE method. However, the removal of the hydrogen from the system introduces an error due to the difference in the number of vibrational degrees of freedom, and the resulting discrepancy between the vibrational zero point energies. Hence, an *ad-hoc* correction $\Delta_{\mathrm{zp}} E$, the zero point energy difference between the product and the reactant systems, is added to the free energy in Eq. (4.5). The calculation of

$\Delta_{\rm zp}E$ is described in Sec. 3.1. The final free energy difference associated with the PCET step in Eq. (4.1) is thus:

$$\Delta G = \Delta_{\rm dh}A + \Delta_{\rm zp}E + \tfrac{1}{2}\mu\left[\mathrm{H}_{2\,\mathrm{(g)}}\right]. \tag{4.6}$$

4.2 Computational Details

All calculations are carried out with a modified rVV10 functional,[125] which is suitable for describing the long-range correlation present in liquid water. Following the work of Miceli *et al.*, the b parameter of rVV10 is set to $b = 9.3$ in order to obtain the correct water density.[126] An energy cutoff for the plane wave basis of 500 Ry is found to lead to converged results. The valence electrons of titanium are described using a double-ζ quality MOLOPT basis set.[93] Correlation-consistent triple-ζ (cc-TZ) basis sets are used for hydrogen and oxygen.[138,139] The core potential of all elements is modeled by Goedecker-Teter-Hutter pseudopotentials.[120]

All MD simulations are carried out with a time step of 0.5 fs in order to adequately sample all vibrational modes present in the system. The temperature is controlled by a Nosé-Hoover chain and set to $T = 350$ K. This slight increase with respect to room temperature is chosen to ensure the frank liquid behavior of water.[140] The effect of this temperature raise on the reaction free energies is estimated using the CHE approach. A modification of at most 0.06 eV with respect to room temperature is calculated. The MD simulations of the systems with the various intermediates are carried out for at least 4 ps when averaging both structural properties and vertical dehydrogenation energies. In the case of OOH_{ads} an harmonic constraint has been used to restrain the hydrogen in the OOH adsorbate, as it has the tendency to spontaneously dissociate and bond with a nearby bridge oxygen atom at the surface. Hence, the intermediate considered in this case corresponds to a metastable configuration. To ensure that the effect on the calculated free energies is negligible, a similar constraint is applied to both the reactant and the product system in the relevant reaction step.[141,142]

4.2.1 Computational Hydrogen Electrode

The atomic configurations corresponding to the vacuum interfaces with the various reaction intermediates are relaxed. Two adsorbates are attached symmetrically to the slab, one at each surface. This eliminates any buildup of electric fields across the vacuum region devoid of a screening medium, and binding energy modifications associated therewith.

For each species, whether adsorbed or not, we carry out a vibrational analysis to determine the vibrational modes. We use the calculated frequencies to compute the thermodynamic corrections as described in Sec. 3.1. The obtained values are shown in Table 4.1.

Table 4.1 – From left to right: Zero point energy ZPE, entropy correction TS, internal energy contribution $\Delta U^{0\to T}$, and total correction ΔE_{corr} defined as $\Delta E_{\text{corr}} \equiv \text{ZPE} - TS + \Delta U^{0\to T}$. All values are in eV.

	ZPE	TS	$\Delta U^{0\to T}$	ΔE_{corr}
$H_2O_{(\ell)}$	0.265	0.434	0.103	−0.066
$H_{2(g)}$	0.573	0.673	0.103	0.003
$O_{2(g)}$	0.092	0.606	0.103	−0.411
H_2O_{ads}	0.691	0.099	0.060	0.652
OH_{ads}	0.356	0.078	0.046	0.324
O_{ads}	0.092	0.027	0.019	0.084
$H_2O_{2\,\text{ads}}$	0.789	0.136	0.080	0.733
OOH_{ads}	0.473	0.149	0.082	0.406
$O_{2\,\text{ads}}$	0.147	0.159	0.082	0.070

4.3 Results

The rutile TiO_2(110) surface is modeled by a 5-layer slab exposing a 4×2 interface repeat unit in the supercell. The slab is separated from its nearest periodic image in the z direction by 15 Å. In the solvated case, this region is filled with 80 water molecules. We consider all reaction intermediates to be adsorbed at a single five-coordinated surface titanium atom (Fig. 4.1). In particular, the MD simulation of the O_{ads} adsorbate in the presence of explicit water indicates that this species forms a single bond with the surface through the Ti atom. However, at the vacuum interface O_{ads} forms an additional bond with a surface O atom in its most stable configuration. Therefore, to enable a meaningful comparison with the solvated case, we sample the vacuum interface with O_{ads} in a similar configuration without extra bonds, which is found to correspond to a local minimum.

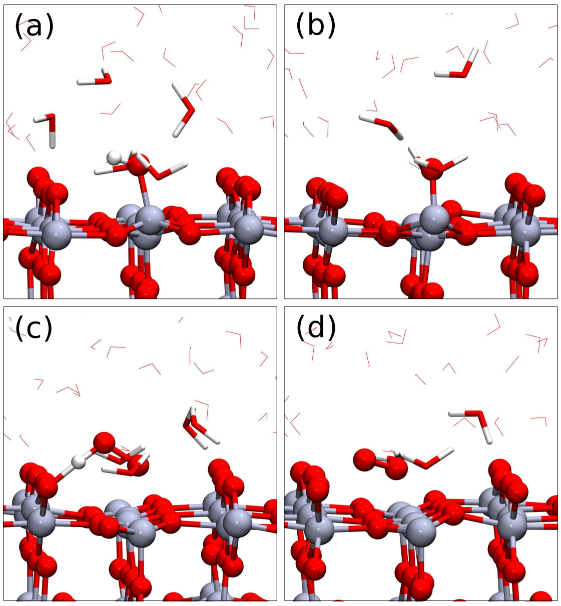

Figure 4.1 – Detailed views of the first solvation shell for (a) OH_{ads}, (b) O_{ads}, (c) OOH_{ads}, and (d) O_{2ads}. White atoms represent hydrogen, red atoms oxygen, and gray atoms titanium. For clarity, water molecules far away from the active site are rendered schematically.

To verify the proper liquid behaviour of the water layer, we evaluate the radial distribution function of the O-O distance, as well as the density across the water region. Fig. 4.2(a) shows that the radial distribution of the water oxygen atoms $g_{OO}(r)$ in the interface model is in accord with the radial distribution function of bulk water. The density across the water region approaches 1 g/cm^3 in its center, as can be seen Fig. 4.2(b). Oscillations in the mass density indicating a long-range fluctuation in the structure of the simulated water layer persist even in the centermost region. While this may be explained by the relatively short sampling time of 4 ps, it could also be the consequence of an insufficiently thick water layer. Nevertheless, in light of the good agreement between the radial distribution function of the simulated water layer with that of bulk liquid water, and given the disproportionate importance of the immediate environment of the adsorbate on the studied solvent effect, the chosen water layer thickness is deemed sufficient for the purpose of this study.

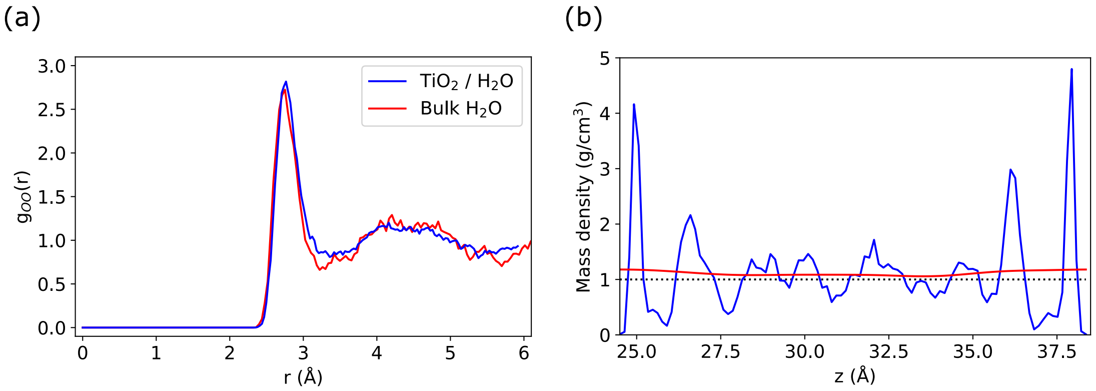

Figure 4.2 – (a) The radial distribution function of the O-O distance for the TiO_2/water interface model (shown in blue), and for bulk water (red). (b) The mass density across the water region, represented by the blue curve. The red curve corresponds to an average density achieved as a convolution of the calculated density and a Gaussian function. The dotted line corresponds to the experimental water density of 1 g/cm^3.

In order to apply the procedure outlined in Sec. 4.1, the reaction mechanism in Eqs. (1.2) is adapted so as to ensure that all reaction intermediates remain adsorbed at the TiO_2 surface, and that the product and reactant configurations in each PCET step only differ by a single hydrogen atom:

$$\begin{aligned} H_2O_{ads} &\longrightarrow OH_{ads} + H^+ + e^-, \\ OH_{ads} &\longrightarrow O_{ads} + H^+ + e^-, \\ H_2O_{2\,ads} &\longrightarrow OOH_{ads} + H^+ + e^-, \\ OOH_{ads} &\longrightarrow O_{2\,ads} + H^+ + e^-. \end{aligned} \tag{4.7}$$

Note that both the initial water molecule as well as the final oxygen molecule remain attached, and that the third step proceeds from the $H_2O_{2\,ads}$ intermediate. According to Eq. (4.6), the free energy steps corresponding to the above set of reactions are:

$$\begin{aligned}
\Delta G'_1 &= \Delta_{\mathrm{dh}} A_{\mathrm{H_2O\,ads}} + \tfrac{1}{2}\mu[\mathrm{H_{2(g)}}] + \Delta_{\mathrm{zp}} E_{\mathrm{H_2O\,ads}}, \\
\Delta G'_2 &= \Delta_{\mathrm{dh}} A_{\mathrm{OH\,ads}} + \tfrac{1}{2}\mu[\mathrm{H_{2(g)}}] + \Delta_{\mathrm{zp}} E_{\mathrm{OH\,ads}}, \\
\Delta G'_3 &= \Delta_{\mathrm{dh}} A_{\mathrm{H_2O_2\,ads}} + \tfrac{1}{2}\mu[\mathrm{H_{2(g)}}] + \Delta_{\mathrm{zp}} E_{\mathrm{H_2O_2\,ads}}, \\
\Delta G'_4 &= \Delta_{\mathrm{dh}} A_{\mathrm{OOH\,ads}} + \tfrac{1}{2}\mu[\mathrm{H_{2(g)}}] + \Delta_{\mathrm{zp}} E_{\mathrm{OOH\,ads}},
\end{aligned} \tag{4.8}$$

where $\Delta_{\mathrm{dh}} A_{X\,\mathrm{ads}}$ is the dehydrogenation free energy of species X calculated via the TI method, $\Delta_{\mathrm{zp}} E_{X\,\mathrm{ads}}$ is the zero point energy difference between the reactant and the dehydrogenated product, and the chemical potential of the hydrogen molecule $\mu[\mathrm{H_{2(g)}}]$ is calculated in the gas phase approximation at the conditions of the reversible hydrogen electrode.[142] The procedure adopted to calculate the free energy steps is as follows. For the value of Kirkwood mixing parameter $\eta = 0$ a set of representative configurations is selected from the simulated trajectory of the reactant system. The total energy of each configuration is computed through single-point calculations with the hydrogen atom present, and with the hydrogen atom removed. The vertical dehydrogenation energy is the average of the differences between these total energies. For $\eta = 1$, the procedure is similar, albeit based on the trajectory of the product system. Instead of removing the hydrogen atom, a hydrogen atom is added in each selected configuration instead. This added hydrogen atom is allowed to relax, while the remaining atomic positions are kept fixed. For intermediate values of η ($0 < \eta < 1$), the dynamics is evolved according to a linear combination of the forces achieved with and without the hydrogen atom. The vertical dehydrogenation energy level is calculated as the difference between the total energy of a configuration of the reactant and that of the same configuration with the hydrogen atom removed. During the mixed Hamiltonian dynamics, the hydrogen atom, which is absent in the dehydrogenated configuration, is replaced by a "ghost" hydrogen atom without a corresponding pseudopotential or basis set. The position of this "ghost" atom is subject to harmonic constraints in order to ensure that it remains in a reasonable position throughout the mixed dynamics. We find that MD runs starting from equilibrated configurations of the reactant (i.e. with the hydrogen atom present) yield converged vertical dehydrogenation energies within about 1 ps. The statistical error on the average vertical dehydrogenation energy is estimated through a blocking analysis.[143] We find that the error incurred by the application of the trapezoidal integration rule is lower than the statistical error in all cases.

The free energy steps in Eqs. 4.8 are evaluated both in the presence and in the absence of the explicit solvent, which makes it possible to isolate the effect of the solvent on the relevant free energy steps. Figure 4.3 shows the four free energy steps as the areas below the curves representing the vertical dehydrogenation energies. Finally, the same reaction free energies are calculated at the vacuum interface using the CHE method. The results of the TI method in the presence and in the absence of the solvent, as well as those of the CHE approach, are listed in Table 4.2.

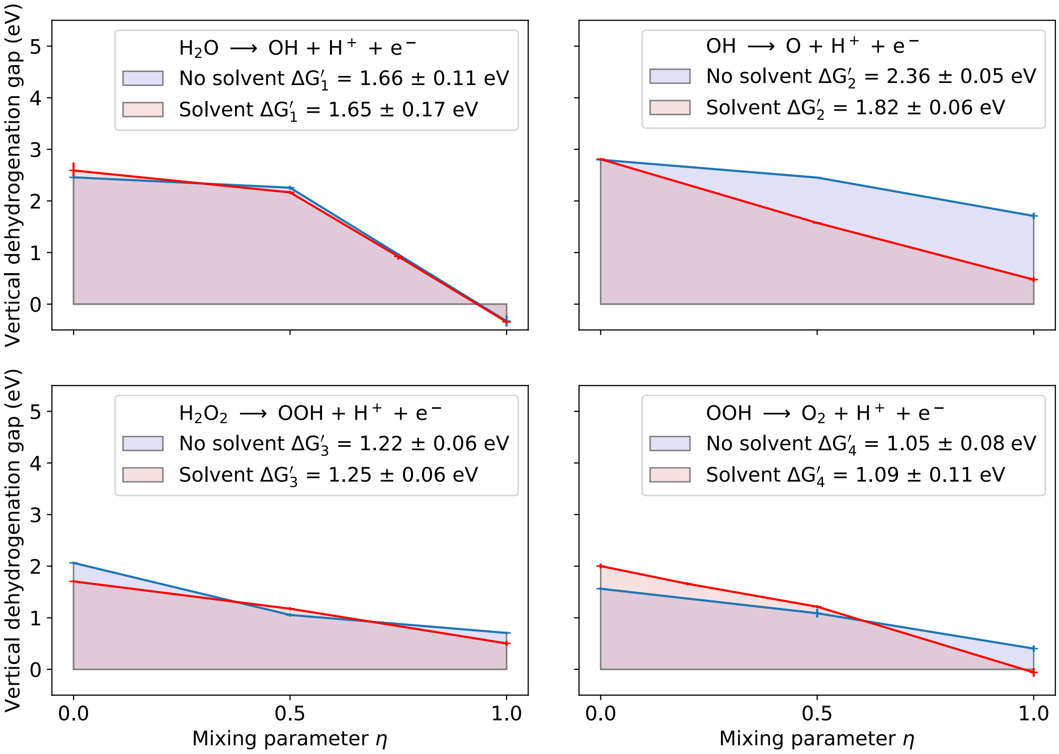

Figure 4.3 – Vertical dehydrogenation energies calculated for the four reactions in Eqs. (1.2), including the zero point energy correction and the chemical potential of hydrogen, as a function of the Kirkwood mixing parameter η. The area under the curve represents the free energy corresponding to the proton-coupled electron transfer step.

First, we compare the reaction free energies obtained at the vacuum interface using the TI and CHE methods. The values of $\Delta G'_1$, $\Delta G'_2$, and $\Delta G'_3$ calculated at the two levels of theory exhibit a difference of less than 0.1 eV. The fourth free energy step, $\Delta G'_4$, is larger by 0.3 eV in the case of the CHE method than in the TI framework. This difference is attributed to small variations in the binding energies and in the thermodynamic corrections of the OOH_{ads} and $O_{2\,ads}$ adsorbates. Overall, a good agreement is found between the CHE and the TI results at the vacuum interface, suggesting that the CHE model is sufficient in capturing thermal effects. Next, a

Table 4.2 – Free energy steps $\Delta G'_i$ calculated using the thermodynamic integration (TI) method with and without solvent, and the computational hydrogen electrode (CHE) method. All values are in eV.

	CHE	TI no solvent	TI solvent
$\Delta G'_1$	1.76	1.66 ± 0.11	1.65 ± 0.17
$\Delta G'_2$	2.43	2.36 ± 0.05	1.82 ± 0.06
$\Delta G'_3$	1.12	1.22 ± 0.06	1.25 ± 0.06
$\Delta G'_4$	1.38	1.05 ± 0.08	1.09 ± 0.11

comparison between the results in the presence and the absence of liquid water is drawn. The free energy steps $\Delta G'_1$, $\Delta G'_3$, and $\Delta G'_4$ are practically unaffected by the inclusion of the solvent, showing differences below 0.1 eV. The second reaction step $\Delta G'_2$, instead, is modified by 0.54 eV in the presence of the water, implying a strong solvent effect on the reaction intermediates involved.

4.4 Origin of the Solvent Effect

4.4.1 Structural Analysis

In order to get deeper insight into the solvent effect, we analyze in detail the structural features of the adsorbates in the presence of the solvent, in particular the number of hydrogen bonds. Table 4.3 gives the number of coordinated water molecules and hydrogen bonds associated with the oxygen atoms of the adsorbed reaction intermediate. The number of water molecules coordinated with the adsorbate is obtained as the average number of oxygen atoms belonging to water molecules that are closer than 3.5 Å. Following a commonly adopted criterion in the literature,[126,142,144] we assume that an accepted hydrogen bond is formed when the OHO angle involving an O atom of a coordinated water molecule, one of its hydrogen atoms, and an oxygen atom of the adsorbate is greater than 140°. We consider the hydrogen bond to be donated when it involves a hydrogen atom of the adsorbate and a water molecule.

Table 4.3 – For each adsorbate, we give the average number of coordinated water molecules (cw), the sum of accepted (aH) and donated (dH) hydrogen bonds, and the variation of bond length between the surface Ti atom and the O atom of the adsorbate ($\Delta_{\text{Ti-O}}$) upon inclusion of the solvent.

Adsorbate	cw	aH + dH	$\Delta_{\text{Ti-O}}$ (Å)
H_2O_{ads}	5.71	2.44	0.04
OH_{ads}	5.53	1.69	0.04
O_{ads}	5.65	2.13	−0.20
$H_2O_{2\,ads}$	6.44	4.26	0.29
OOH_{ads}	4.72	1.85	0.21
$O_{2\,ads}$	4.08	1.35	−0.11

In the first OER step, H_2O_{ads} and OH_{ads} are of importance. The adsorbed water molecule coordinates 5.71 liquid water molecules on average. 2.44 hydrogen bonds are formed overall, with one being accepted and up to two donated. OH_{ads} coordinates nearly the same number of water molecules, but only forms 1.69 hydrogen bonds [cf. Fig. 4.1(a)]. The lower number of hydrogen bonds in the product system of the first OER step suggests an increase of $\Delta G'_1$ upon inclusion of the solvent. However, no such increase is observed. In the second step, O_{ads} [cf. Fig. 4.1(b)] forms 2.13 hydrogen bonds, more than the average of 1.69 in the case of the reactant OH_{ads}. More hydrogen bonds in the product system imply extra stabilization with respect to the reactant, and thus a decrease in the associated free energy step upon solvation. Indeed, $\Delta G'_2$ at the water interface is lower by 0.54 eV compared to the vacuum interface. The third reaction step involves $H_2O_{2\,ads}$ and OOH_{ads}. The former coordinates a large number of water molecules (6.44 on average) and is stabilized by 4.26 hydrogen bonds. In contrast, OOH_{ads} forms less than two hydrogen bonds. In particular, a donated hydrogen bond between the adsorbate and a surface bridge oxygen is present [cf. Fig. 4.1(c)]. The lower hydrogen bond stabilization of OOH_{ads} suggests an increase of the third free energy step $\Delta G'_3$ when water is included. However, the value of $\Delta G'_3$ remains unchanged upon the introduction of the solvent. Finally, in relation to the fourth OER step, the product $O_{2\,ads}$ [cf. Fig. 4.1(d)] forms slightly fewer hydrogen bonds than OOH_{ads} on average: only 1.35 compared to 1.85. On this basis, $\Delta G'_4$ is expected to be larger in the presence of the solvent than in its absence. At variance, no such behavior of the calculated free energies is observed, as $\Delta G'_4$ remains unchanged in both cases. Overall, the structural analysis based on hydrogen bond counting appears to be inadequate to explain the observed trends in free energy.

4.4.2 Electrostatic Analysis

The structural analysis proving inconclusive, the explanation of the large solvent stabilization of O_{ads} needs to be looked for elsewhere.

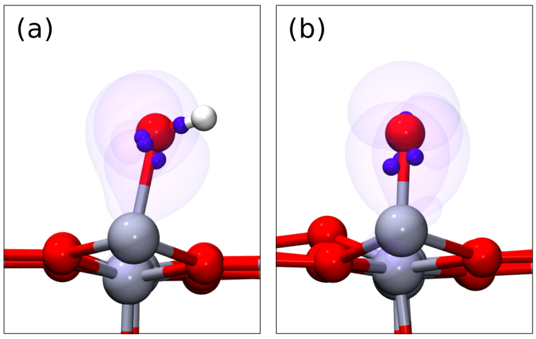

Figure 4.4 – Centers of maximally localized Wannier functions (blue balls) in the case of (a) OH_{ads} and (b) O_{ads}. In both cases, the oxygen atom of the adsorbate carries eight Wannier centers, but Wannier centers of opposite spin almost coincide and thus appear as a single ball. Since an extra proton is present in the case of OH_{ads}, the adsorbates OH_{ads} and O_{ads} are effectively in a charge state of -1 and -2, respectively. The isosurfaces illustrate the shape of the Wannier orbitals.

A study of the maximally localized Wannier functions associated with the OER intermediates indicates that O_{ads} acquires two electrons from the TiO_2 slab [see Fig. 4.4]. This is in contrast with the other reaction intermediates OH_{ads}, $H_2O_{2\,ads}$, and OOH_{ads} which only harbor one electron. The large partial negative charge localized at O_{ads} at the interface could then lead to a strong electrostatic stabilization in water ($\epsilon_r \approx 80$) as compared to in vacuum ($\epsilon_r = 1$). Two tests are carried out to investigate this hypothesis.

First, we replace the adsorbed oxygen with a fluorine atom both at the vacuum and the solvated interface. The atomic configuration is kept fixed. Since the fluorine atom attracts only one electron to fill its valence shell, this reduces the amount of partial charge located at the interface. In agreement with our assumption, the solvent stabilization of F_{ads} is reduced with respect to that of O_{ads} by up to 1.4 eV. In the second test, a classical electrostatics simulation of a model system is carried out.[145] The semiconductor/water and semiconductor/vacuum interfaces are modeled using periodic cells of dielectric materials. A Gaussian charge distribution of magnitude $q = -e$ or $q = -2e$ and a spatial extent consistent with the Wannier function analysis is placed at the interface. We find that in the case of the model semiconductor/water interface, the electrostatic energy difference between a charge $q = -e$ and $q = -2e$ is approximately 1.5 eV. This value is in accord with that obtained from the first test, and suggests that the extra solvent stabilization of O_{ads} can be explained on the grounds of electrostatic effects.

4.5 Full Oxygen Evolution Reaction Pathway

Having analyzed the effect of the solvent on the individual PCET steps in Eqs. (4.7), we now focus on the full OER pathway in Eqs. (1.2). In particular, the initial system must nominally consist of liquid water and a bare active Ti site, and the final system must exhibit gaseous oxygen and again, an empty active site. The analysis of the solvent effect suggests that only reaction steps involving doubly charged intermediates are critical, as the electrostatic solvent stabilization scales with the square of the charge. Hence, we calculate the initial adsorption free energy of a water molecule, and the final desorption free energy of the O_2 molecule in the CHE framework at the vacuum interface. We find that the free energy of H_2O adsorption $\Delta F_{\mathrm{ads}}[H_2O] = -0.37$ eV, and the free energy of O_2 desorption $\Delta F_{\mathrm{des}}[O_2] = -1.30$ eV. Furthermore, the third step needs to be modified for the reaction to proceed from O_{ads} and a liquid water molecule rather than from $H_2O_{2\,\mathrm{ads}}$. Therefore, the free energy $\Delta F[O_{\mathrm{ads}} \rightarrow H_2O_{2\,\mathrm{ads}}]$ must first be obtained. As the strongly charged O_{ads} species is involved, the solvent effect is assumed to be important. Thus, we use the Blue Moon method, described in Sec. 2.4, to calculate $\Delta F[O_{\mathrm{ads}} \rightarrow H_2O_{2\,\mathrm{ads}}]$ in the presence of the explicit solvent, as well as at the vacuum interface. The initial and final configurations are shown in Fig. 4.5.

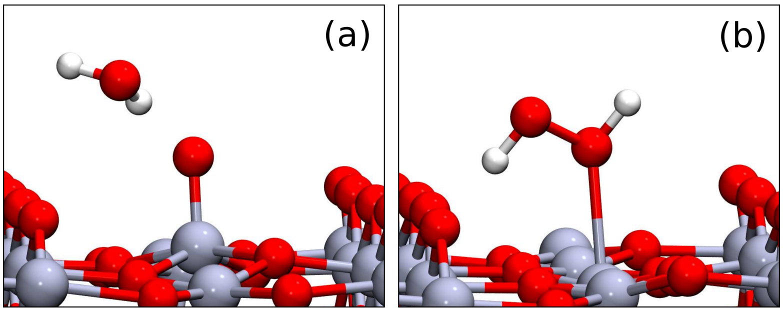

Figure 4.5 – Illustration of (a) the initial configuration consisting of O_{ads} and a nearby water molecule, and (b) the final configuration containing $H_2O_{2\,\mathrm{ads}}$. Oxygen atoms are shown in red, hydrogen atoms in white, and titanium atoms in gray. The solvent is not shown for the sake of clarity.

The distance between O_{ads} and the oxygen atom of a coordinated liquid water molecule is chosen as the reaction coordinate ξ. Seven values of ξ are uniformly chosen from the interval defined by the initial value $\xi_i = 2.66$ Å, representing $O_{\mathrm{ads}} + H_2O$ [cf. Fig. 4.5(a)], and the final value $\xi_f = 1.46$ Å, corresponding to $H_2O_{2\,\mathrm{ads}}$ [cf. Fig. 4.5(b)]. For each ξ a constrained MD simulation is carried out in which the distance between the two selected atoms remains fixed. The Lagrange coefficients

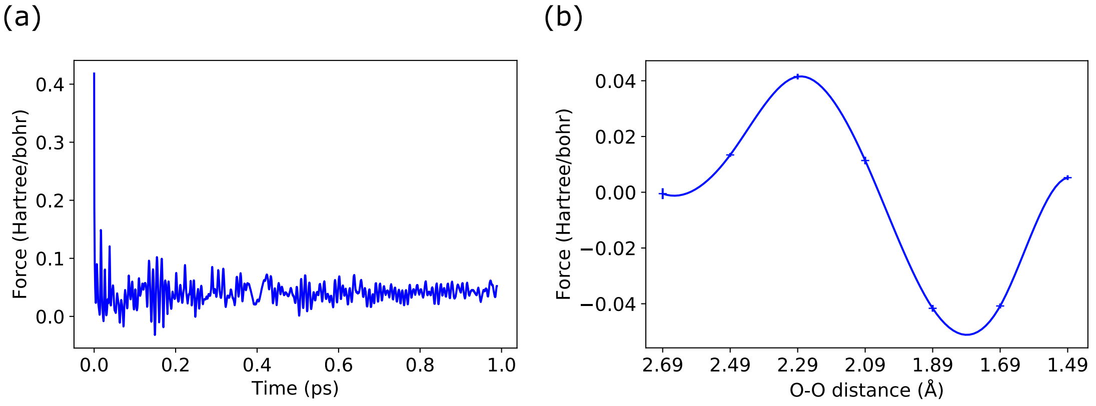

Figure 4.6 – (a) The force acting on the constraint for one specific choice of O-O distance over the duration of the MD simulation. Rapid convergence is observed. (b) Force acting on the constrained atoms as a function of the O-O distance.

associated with the constraint are computed at each MD step. As per Sec. 2.4, for our choice of reaction coordinate the Lagrange coefficients directly represent the force acting on the constraint. We find 1.5 ps sufficient to obtain a converged value for this force. Fig. 4.6(a) shows the force on the constraint as a function of time. Only minor oscillations are observed after an initial equilibration period. The average force for each ξ is given in Fig. 4.6(b). The error is calculated using a blocking analysis.[143] Finally, the force profile can be integrated using the trapezoid integration rule to achieve the free energy profile of the reaction described by ξ. The free energy profiles of $H_2O_{2\,\mathrm{ads}}$ formation corresponding to the water and vacuum interfaces are shown in Fig. 4.7. We obtain a value of -0.14 ± 0.02 eV and -0.69 ± 0.03 eV for the free energy difference $\Delta F\,[\mathrm{O_{ads}} \rightarrow \mathrm{H_2O_{2\,ads}}]$ in the solvated and the vacuum case, respectively. These values differ by 0.55 eV on account of the different screening conditions in the two cases, and are consistent with the results shown in Fig. 4.3. We also calculate $\Delta F\,[\mathrm{O_{ads}} \rightarrow \mathrm{H_2O_{2\,ads}}]$ using the CHE method at the vacuum interface for the sake of comparison. We find a value of -0.88 eV, comparing favorably with the value obtained using Blue Moon in the vacuum case. The OER free energies corresponding to the reactions in Eqs. (1.2) can be expressed using the above correction as follows:

$$\begin{aligned}
\Delta G_1 &= \Delta G_1' + \Delta F_{\mathrm{ads}}\,[\mathrm{H_2O}],\\
\Delta G_2 &= \Delta G_2',\\
\Delta G_3 &= \Delta G_3' + \Delta F\,[\mathrm{O_{ads}} \rightarrow \mathrm{H_2O_{2\,ads}}],\\
\Delta G_4 &= \Delta G_4' + \Delta F_{\mathrm{des}}\,[\mathrm{O_2}].
\end{aligned} \tag{4.9}$$

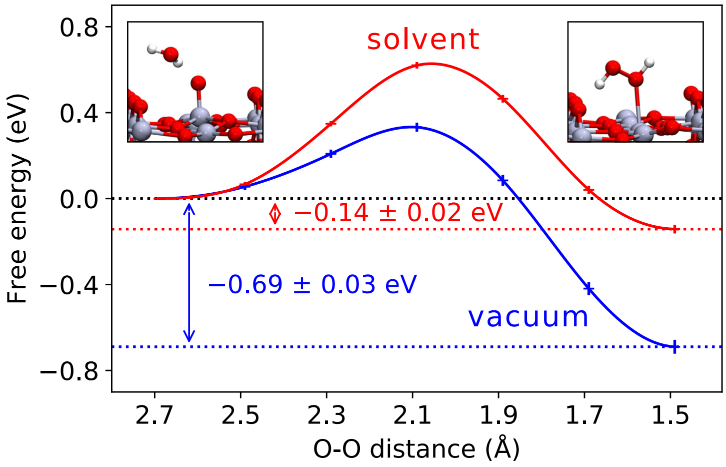

Figure 4.7 – Free energy profile of the H_2O_{2ads} formation in the vacuum (blue) and in the solvated (red) case. The insets illustrate the initial and final configurations. The solvent is not shown for clarity.

The calculated free energy steps are given in Table 4.4 and shown in Fig. 4.8. The sum of the four ΔG steps is approximately 4.0 eV regardless of the adopted method. The value achieved with the CHE method is, by construction, the overall OER overpotential ΔG_{OER} corresponding to the reaction:

$$2H_2O_{(\ell)} \longrightarrow 2H_{2(g)} + O_{2(g)} \tag{4.10}$$

However, this does not apply to the TI results, where the above only holds true in principle. Hence, it is reassuring that the values of ΔG_{OER} obtained using different techniques fall within 0.15 eV of each other. Unlike in other work,[31,33,41] and in contrast to the previous chapter, we do not fix the total energy of the $O_{2(g)}$ species in order to obtain the experimental value of $\Delta G_{\mathrm{OER}} = 4.92$ eV.[146] The discrepancy between the measured and the calculated value of ΔG_{OER} reflects the limitations of the adopted DFT functional.

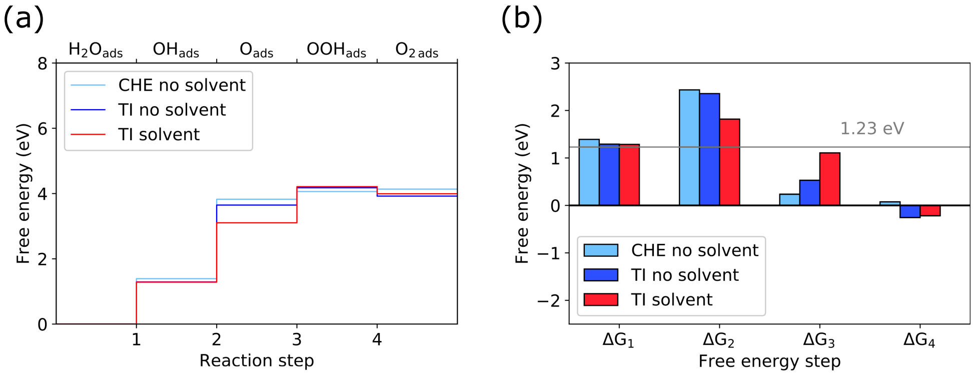

Figure 4.8 – Comparison of the free energies corresponding to the full OER mechanism calculated using the CHE method and the TI method.

Table 4.4 – Free energy steps ΔG_i calculated using the thermodynamic integration (TI) method with and without solvent, and the computational hydrogen electrode (CHE) method. All values are in eV.

	CHE	TI no solvent	TI solvent
ΔG_1	1.39	1.29 ± 0.11	1.29 ± 0.17
ΔG_2	2.43	2.36 ± 0.05	1.82 ± 0.06
ΔG_3	0.24	0.53 ± 0.06	1.11 ± 0.07
ΔG_4	0.08	−0.26 ± 0.08	−0.22 ± 0.11

4.6 Discussion and Conclusion

The presence of explicit water molecules has a noticeable influence on the ΔG values of the OER. First, the reaction determining step ΔG_2 of the OER at the TiO_2/vacuum interface is reduced by 0.5 eV upon inclusion of the solvent. In the work of Cheng *et al.*,[46] only a fraction of a water monolayer is used to model the solvent. The effect of hydrogen bond stabilization and charge effects are therefore not fully captured and their result of 2.4 eV might be overestimated, as can be inferred by comparing our values of ΔG_2 with and without solvent. Second, the stabilization of the O_{ads} intermediate in the presence of liquid water leads to an increase of the third free energy step ΔG_3. This contrasts with results from static calculations at the similar IrO_2 interface in which the solvation effect was found to yield reduced overpotentials in the first three OER steps.[41] This difference most likely results from the consideration of a relaxed configuration for O_{ads} that differs from the equilibrium structure that we observe in the molecular dynamics simulations. For the same reason, in the CHE approach, our value of ΔG_2 is noticeably larger than that found by Valdés *et al.* (1.47 eV).[33]

In conclusion, we described the solvent effects on the energetics of the OER at finite temperature. In the absence of the solvent, the computational hydrogen electrode method yielded free energies that agree well with those obtained by thermodynamic integration. A significant reduction of the free energy associated with the rate determining step was observed upon inclusion of the solvent. An analysis of the structure at the solvated interface, with a particular focus on hydrogen bonds, was insufficient to explain the observed trends. Instead, the large stabilization of the oxygen intermediate due to the solvent can be understood in terms of the screening at the interface. This finding supports the use of implicit models for describing the solvent, which generally capture the electrostatics but are unable to account for hydrogen bonds. In the light of the present study, it is recommended that solvent effects be carefully considered in ongoing searches for novel OER catalysts.

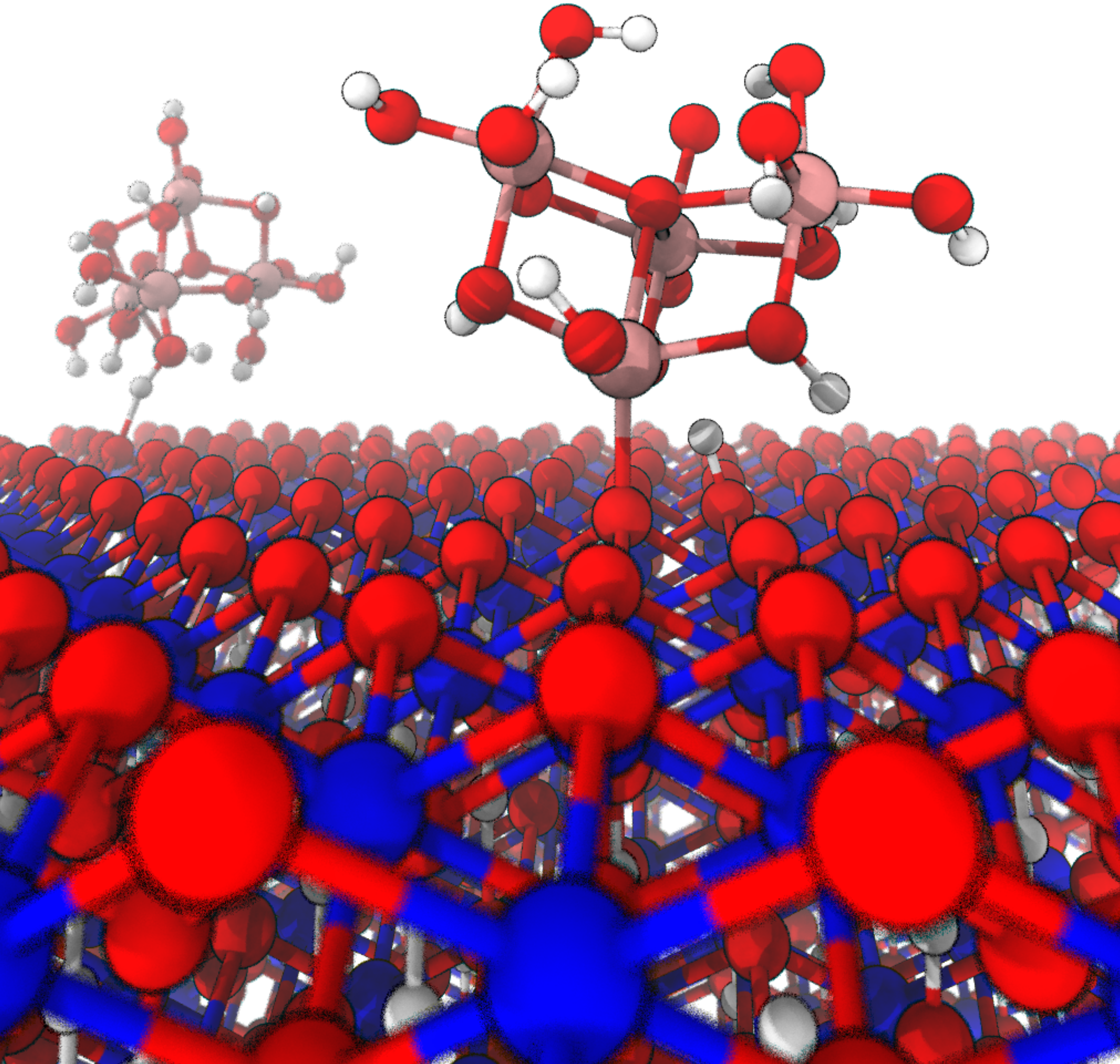

5 Bifunctional Oxygen Evolution Reaction Mechanism

In this chapter, we investigate the potential of the bifunctional mechanism in Eqs. (1.6):

$$
\begin{aligned}
H_2O_{(\ell)} &\longrightarrow OH_a + H^+ + e^-, \\
OH_a &\longrightarrow O_a + H^+ + e^-, \\
O_a + H_2O_{(\ell)} &\longrightarrow H_b + O_{2(g)} + H^+ + e^-, \\
H_b &\longrightarrow H^+ + e^-,
\end{aligned}
\tag{5.1}
$$

to reduce the overpotential of the OER. First, we calculate the free energy steps corresponding to the bifunctional mechanism for a set of catalysts. This set consists of mainly transition metal oxides, including both metals and semiconductors. In particular, we consider the following surfaces: rutile TiO_2(110), anatase TiO_2(101), SnO_2(110), RuO_2(110), IrO_2(110), Ni_2P(0001), and $BiVO_4$(001). In addition, we also address to what extent the free energy steps depend on the adopted theoretical framework and thus perform calculations at both the semilocal and hybrid functional levels of theory. Our calculations demonstrate that it is theoretically conceivable that the bifunctional mechanism leads to the breaking of the scaling relationships for a suitable combination of catalysts. The detailed mechanism by which two active reaction sites on different catalysts are involved is not addressed. Instead, free energy calculations on idealized surfaces are used to gain insight into the mechanism and to identify general trends governing the catalytic performance in the bifunctional scheme.

Left: FeOOH nanoclusters adsorbed on the surface of NiOOH – a catalyst studied in connection with the bifunctional mechanism.

Second, we investigate in detail the specific pairing of γ-NiOOH and γ-FeOOH, which is suggested to be the unconventional bifunctional catalyst in the work of Song *et al.*[76] Several possible configurations of the two catalysts are studied, including slabs, layers, and nanoclusters. While not exhaustive, this work represents a first study of the detailed arrangement of the two active sites.

The results presented in this chapter have been published in Ref. [50].

5.1 Trends and Principles Governing the Efficiency of the Bifuctional Mechanism

5.1.1 Anodic Conditions

In the study of the regular OER mechanism in Chapter 3, we adopted neutral charge conditions. This approach is consistent with previous work on the OER in the literature.[23,24,33,36,41,121,147–149] In reality, the OER takes place under anodic conditions. To model these conditions, we remove an electron from the catalyst, creating a hole in the highest occupied electronic state, and perform calculations for the charged system. First, we investigate the effect of adopting such anodic conditions on the free energy steps of the regular OER mechanism discussed in Eqs. (1.2). The calculations are performed at the semilocal level of theory using the RPBE functional.[86] The computational details are identical to those given in Sec. 3.2.1. Figure 5.1(a) shows the comparison of the free energy steps ΔG_i obtained under neutral charge and anodic conditions. All reaction intermediates in the regular mechanism are electronegative, and will attract an electron from the valence band of the substrate. The introduction of an extra valence band hole does therefore not affect the binding energy of the intermediates to any great extent. We observe a mean absolute error (MAE) of 0.11 eV. This small difference should be attributed to finite size effects associated with the finite charge density of the delocalized valence band hole.

Unlike the regular OER mechanism, the bifunctional mechanism in Eqs. (5.1) involves a hydrogen atom adsorbate. The hydrogen atom, being only weakly electronegative, gives up its electron upon adsorption. In the case of a neutral system, this electron accommodates in the lowest unoccupied electronic state, which corresponds to the conduction band edge or a shallow defect state in the case of a semiconductor and to the Fermi energy in the case of a metal. Under anodic conditions, i.e. in the presence of valence band holes, the electron accommodates close to the highest occupied electronic state instead. This indicates that under anodic conditions the hydrogen is stabilized with respect to the neutral case by an amount corresponding to the band gap. Hence, while the regular mechanism in Eqs. (1.2) is unaffected upon the introduction of anodic conditions, the bifunctional mechanism in Eqs. (5.1) should be strongly affected due to the extra stabilization of the hydrogen intermediate. To verify this, we calculate the hydrogen binding free energy using the RPBE

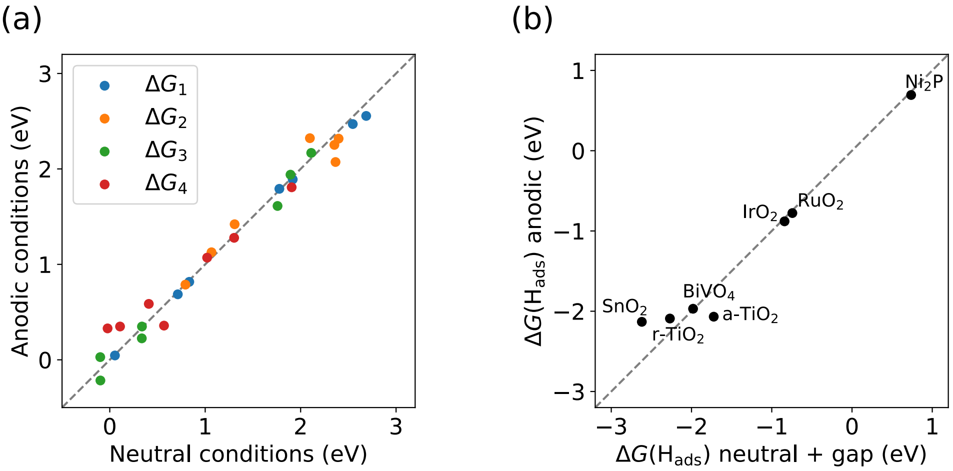

Figure 5.1 – (a) Comparison of the free energy steps corresponding to the regular OER mechanism obtained in neutral and anodic conditions calculated using the RPBE functional. (b) The hydrogen adsorption free energy relevant in the bifunctional mechanism as obtained under anodic conditions (vertical axis) vs. the sum of the band gap and the adsorption free energy evaluated under neutral conditions (horizontal axis).

functional under both neutral and anodic conditions. Figure 5.1(b) shows that by subtracting the band gap from the hydrogen adsorption free energy in the case of neutral simulation cells we obtain values close to those achieved in the presence of a valence band hole. Given the limited effect of anodic conditions on all the reaction intermediates except H_{ads}, as evidenced by the data shown in Fig. 5.1(a), we henceforth retain neutral conditions for all calculations and subtract the value of the band gap from the adsorption free energy of H_{ads} to effectively model anodic conditions.

5.1.2 Bifunctional Mechanism

The free energy steps corresponding to the bifunctional mechanism are calculated in the following way. For every material associated with the binding site a in Eqs. (5.1), we consider the possibility that the H_{ads} in the third reaction step be adsorbed at surface site b of any other material, including itself. In all cases, an undercoordinated surface metal atom serves as site a, and a surface oxygen atom as site b, except in the case of Ni_2P, where a surface phosphorus atom is considered instead. Denoting by N the number of catalysts that we investigate, this approach yields an $N \times N$ array of OER free energy steps, each element belonging to a specific

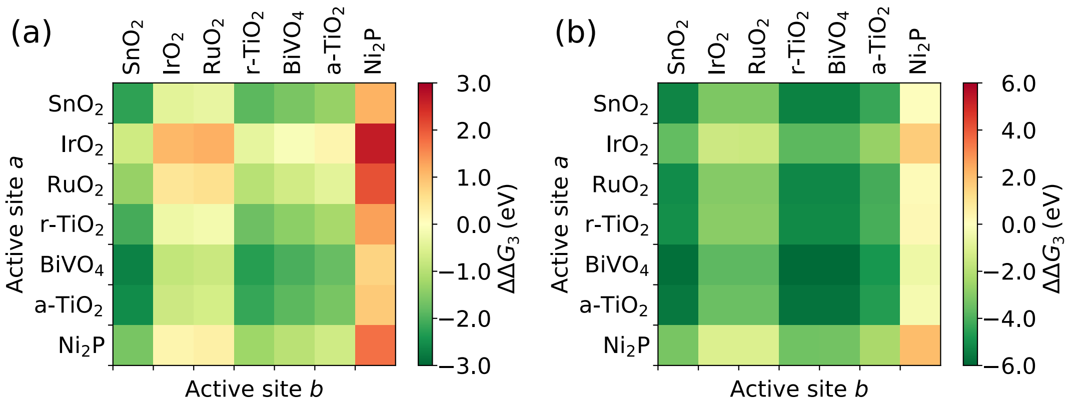

Figure 5.2 – The third OER free energy step ΔG_3 for the bifunctional mechanism with respect to the regular mechanism as calculated with (a) the RPBE functional and (b) the hybrid functionals. The active sites a and b refer to those appearing in Eqs. (1.6). The green color indicates that the corresponding combination of catalysts leads to a reduction of the third OER step in the bifunctional mechanism.

combination of catalysts for the respective reactions on sites a and b. We perform all calculations at both the semilocal level of theory using the RPBE functional, and at the hybrid functional level of theory. The computational details are identical to those presented in Secs. 3.2.1 and 3.3.1, respectively.

The differences in the third OER free energy step as calculated for the bifunctional mechanism and for the regular mechanism are shown in Fig. 5.2. The greenish colors indicate that the bifunctional mechanism yields lower ΔG_3 values, whereas the reddish colors indicate the opposite. The grading of the intensity reflects the size of the difference. At the level of RPBE, we find that all materials except Ni_2P can lead to a reduction of the third free energy step ΔG_3. Moreover, SnO_2, TiO_2, and $BiVO_4$ are associated with the largest reductions of up to 0.4 eV. Using hybrid functionals, we find that even Ni_2P can reduce ΔG_3 when acting as hydrogen acceptor in conjunction with $BiVO_4$ or anatase TiO_2. The reductions of ΔG_3 are generally larger at the hybrid functional level than in the case of RPBE due to the stronger H binding energy. While the bifunctional mechanism leads to a lower value of ΔG_3 for many combinations of catalyst, this alone is not sufficient to result in the reduction of the OER overpotential, as can be seen in Fig. 5.3. In the case of RPBE, the lower value of ΔG_3 in the bifunctional mechanism leads to a lower overpotential only for the following pairings of catalysts: RuO_2 and $BiVO_4$, RuO_2 and anatase TiO_2, Ni_2P and anatase TiO_2. Here, the first material refers to active site a, and the second material to the hydrogen acceptor associated with active site b. In the case of RuO_2

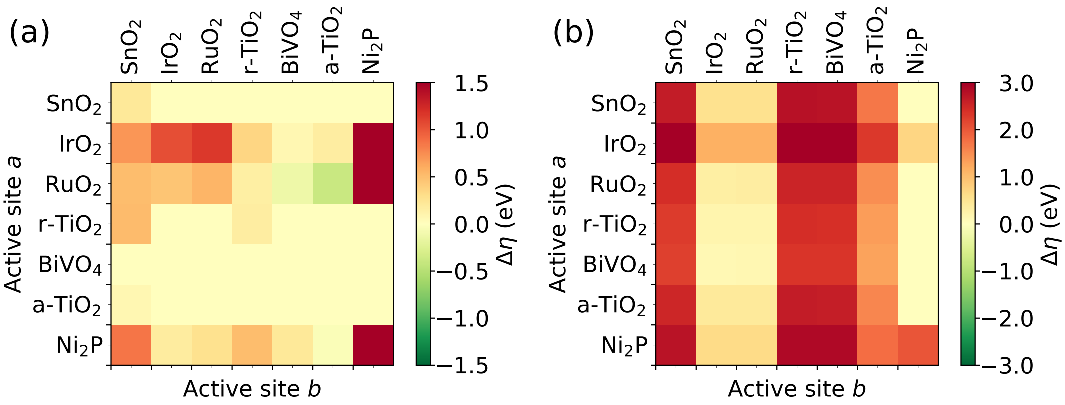

Figure 5.3 – The OER overpotential η for the bifunctional mechanism with respect to the regular mechanism as calculated with (a) the RPBE functional and (b) the hybrid functionals. The green color indicates that the corresponding combination of catalysts leads to an OER overpotential reduction in the bifunctional mechanism.

and a-TiO_2, the bifunctional mechanism leads to a OER overpotential reduction of 0.4 eV. The comparison of the overpotential η achieved with the regular and the bifunctional mechanisms at the semilocal level of theory is illustrated in Fig. 5.4(a). At variance, at the hybrid functional level of theory, no combination of catalysts leads to the reduction of the overall OER overpotential, see Fig. 5.3(b). The same can be concluded from inspecting Fig. 5.4(b), where no combination rises above the black points which correspond to overpotentials in the regular mechanism.

Hence, this investigation demonstrates that there exist specific combinations of catalysts for which the overpotential of the OER following the bifunctional mechanism can indeed be reduced with respect to the regular mechanism. These combinations exhibit lower overpotentials than imposed by the linear scaling relationship, and thus indicate that this relationship can be broken. Even though none of the cases studied here surmounts the top of the volcano, our calculations suggest that such advantageous pairings are indeed within reach. These are important results that support the search for the ideal combination of materials catalyzing the OER through the bifunctional mechanism.

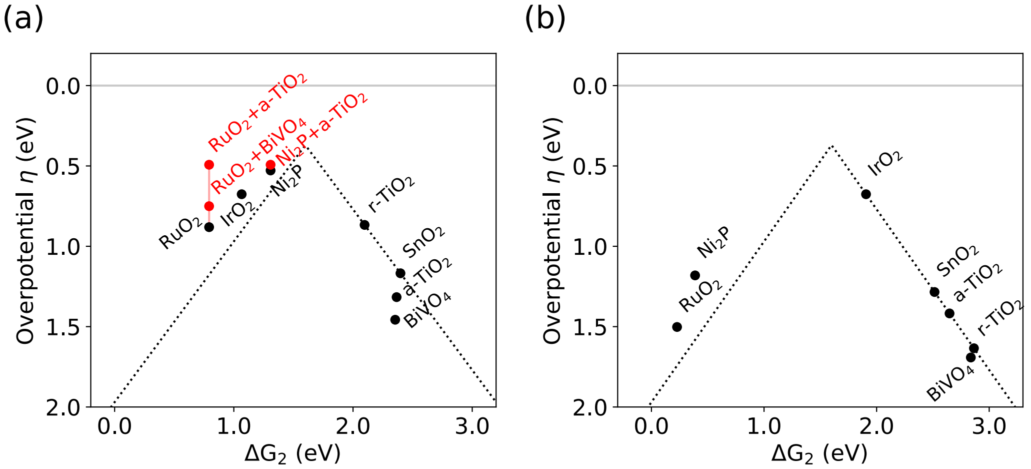

Figure 5.4 – Volcano plot highlighting the linear scaling relationship and showing the comparison between the regular and the bifunctional OER mechanisms. The values corresponding to the regular mechanism are taken from Sec. 1.1. The dotted line is defined by $\max\{\Delta G_2 - 1.23, 3.2 - \Delta G_2 - 1.23\}$. The free energy steps are calculated with (a) the RPBE functional and (b) the hybrid functionals. The black dots correspond to the regular mechanism. The red dots correspond to the bifunctional mechanism and are only shown when this mechanism leads to a lower overpotential.

5.1.3 Band Edge Alignment as Descriptor

In order to guide the search towards the optimal catalyst, it is important to identify relevant physical descriptors characterizing the performance of a catalyst. In the bifunctional mechanism, the third OER step decreases with an increasing hydrogen adsorption free energy, which can be defined as the opposite of ΔG_4 pertaining to the mechanism given in Eqs. (5.1). At the same time, the hydrogen binding energy for the ideal hydrogen acceptor should not be too large, since otherwise the fourth step would turn unfavorable. For instance, SnO_2, TiO_2, and $BiVO_4$ are examples of materials with strong hydrogen adsorption free energy leading to large reductions in ΔG_3 when used as hydrogen acceptors. The hydrogen binding energy could thus be used as a descriptor of the suitability of a material as hydrogen acceptor within the bifunctional scheme.

The case of SnO_2, which is characterized by a deep position of the valence band edge when the material is exposed to an aqueous solution,[118] suggests that the hydrogen adsorption free energy can be associated with the energy level of the highest occupied electronic state. Indeed, a similar correlation between hydrogen adsorption and the lowest unoccupied electronic state has been identified in the case of oxidative dehydrogenation catalyzed by vanadia and ceria.[150]

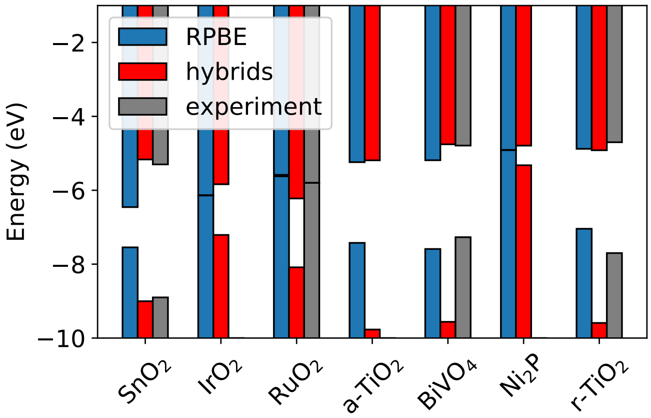

Figure 5.5 – Band edge alignment with respect to the vacuum level. RPBE results are shown in blue, hybrid functional results in red. Where available, the experimental reference is shown in grey. The experimental band gap is added to the electron affinity in order to obtain the position of the valence band edge. The references are the following: SnO_2, Refs. [151–153]; RuO_2, Ref. [154]; rutile TiO_2, Refs. [155] and [156]; $BiVO_4$, Refs. [157] and [158].

To verify this connection, we calculate for all materials in the studied set the alignment of the band edges with respect to the vacuum level. We proceed as follows. First, we establish the energy level of the highest occupied electronic state with respect to the average electrostatic potential by modeling the bulk material in a periodic simulation cell. Next, we consider a slab of the material in vacuum and calculate the line-up of the average electrostatic potential between the bulk-like central region of the slab and the vacuum region. By combining these results we can position the highest occupied electronic level with respect to the vacuum level. This level corresponds to the valence band edge in the case of semiconductors (ionization potential) and to the Fermi level in the case of metals (work function). All these calculations are carried out in neutral charge conditions.

The calculated values obtained with RPBE and hybrid functionals are shown in Fig. 5.5 in comparison with available experimental values. We find that the hybrid functionals lead to a better agreement with experiment for the lowest unoccupied electronic level, except for RuO_2. The data shown in Fig. 5.5 result in a mean absolute error of 0.49 eV in the case of RPBE, as compared to a MAE of 0.27 eV in the case of hybrid functionals. Both functionals perform poorly when it comes to determining the position of the highest occupied electronic level. The RPBE functional gives a

MAE of 0.63 eV due to the systematic tendency of placing this level too high. The hybrid functionals perform even worse pushing the highest occupied level well below the experimental value, with a corresponding MAE of 1.64 eV. This shortcoming of the hybrid functionals should be attributed to the rather high fractions of Fock exchange α used here. Indeed, for most of the studied materials the fraction α that reproduces the experimental band gap is lower than the one adopted here (29% in the case of PBE0 and 30.5% in the case of HSE06). These fractions of Fock exchange were chosen in order to match the calculated free energy of the overall OER with the experimental value of $\Delta G_{\mathrm{OER}} = 4.92$ eV. This, in turn, allows us to dispense with the *ad-hoc* correction to the total energy of the O_2 species, see Sec. 3.3.1. However, the resulting overestimation of α leads to an excessive opening of the band gap and consequently to a deeper energy level for the highest occupied electronic state. Numerical values shown in Fig. 5.5 are provided in Table 5.1.

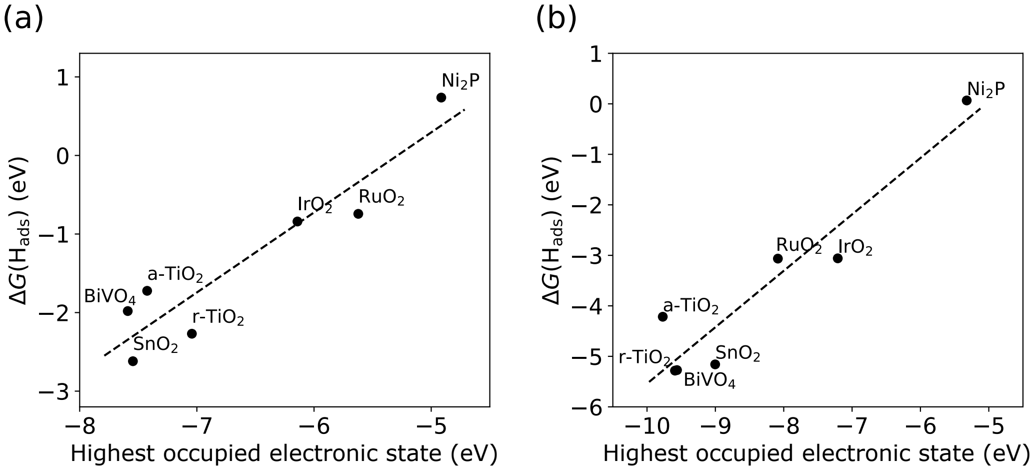

Figure 5.6 – Free energy of hydrogen adsorption vs. highest occupied electronic level aligned with respect to the vacuum level. The dotted line represents a linear regression. The results, which correspond to anodic conditions, are achieved (a) with the RPBE functional and (b) with the hybrid functionals.

Table 5.1 – Band gap (E_g) and energy levels of the highest occupied (VB) and the lowest unoccupied (CB) electronic states with respect to the vacuum level, as obtained with the semilocal and hybrid functionals. In the case of the lowest unoccupied level, the experimental values correspond to the opposite of the electron affinity (work function) for semiconductors (metals). The experimental value of the highest occupied level is achieved by subtracting the experimental band gap from the lowest unoccupied level. All values are in eV.

	RPBE			Hybrids			Experiment		
Species	VB	CB	E_g	VB	CB	E_g	VB	CB	E_g
SnO_2	−7.55	−6.46	1.09	−9.00	−5.17	3.84	−8.90	−5.30[a]	3.60[b]
IrO_2	−6.14	−6.13	0.01	−7.21	−6.36	1.37			
RuO_2	−5.62	−5.58	0.04	−8.09	−6.48	1.86	−5.80	−5.80[c]	0.00
r-TiO_2	−7.04	−4.88	2.16	−9.59	−4.92	4.67	−7.70	−4.70[d]	3.00[e]
$BiVO_4$	−7.59	−5.19	2.40	−9.56	−4.76	4.81	−7.27	−4.79[f]	2.48[g]
a-TiO_2	−7.42	−5.24	2.19	−9.77	−5.19	4.58			
Ni_2P	−4.91	−4.91	0.01	−5.32	−4.80	0.53			

[a] Ref. [151]; [b] Refs. [152, 153]; [c] Ref. [154]; [d] Ref. [155]; [e] Ref. [156]; [f] Ref. [157]; [g] Ref. [158].

Figure 5.6 shows a clear correlation between the hydrogen adsorption free energy and the highest occupied electronic level aligned with respect to the vacuum level: the lower the energy level, the stronger the hydrogen binding energy. The correlation holds for both levels of theory considered here despite their inherent errors. The energy level of the highest occupied electronic state can thus be used as a valid descriptor of the potential of a material for acting as a hydrogen acceptor within the framework of the bifunctional mechanism. More specifically, because of its association with ΔG_4, a suitable hydrogen binding free energy in the bifunctional OER pathway should not be much higher than 1.23 eV to avoid disfavoring the last OER step. The correlation in Fig. 5.6 indicates that the ideal hydrogen acceptor should exhibit a valence band edge lying at ~6.5 eV below the vacuum level. This condition suggests that typical oxide insulators like SnO_2, $BiVO_4$, and TiO_2 generally bind hydrogen too strongly, while Ni_2P shows the opposite behavior. In our set of materials, the middle region around 6.5 eV is occupied by the metals IrO_2 and RuO_2, albeit the two adopted levels of theory show noticeable variation in the results. In this respect, one should remind that the use of hybrid functionals results in the opening of a band gap for these metals and might thus be less reliable than RPBE in these cases.

5.1.4 Discussion and Conclusion

The RPBE results suggest that the bifunctional mechanism can indeed lead to a reduction of the OER overpotential with respect to the regular mechanism. The bifunctional mechanism is more favorable when the following two criteria are met. First, the potential determining step in the regular mechanism corresponds to the third one, i.e. the formation of the OOH_{ads} intermediate. Second, the hydrogen acceptor binds the hydrogen strongly, resulting in a large stabilization of the third step in Eqs. (1.6) as compared to the third step in Eqs. (1.2). Since the reduction of the overpotential is generally limited by the linear scaling relationship involving the second and third steps, the fulfillment of these criteria opens the way to a competitive bifunctional mechanism, as proposed by Song *et al.*[76]

As indicated above, materials that bind hydrogen strongly can most suitably act as hydrogen acceptors. We find a correlation between the energy level of the lowest unoccupied electronic state and the hydrogen adsorption free energy. This relationship can be explained as follows. Upon adsorption, the hydrogen gives up its electron to the bulk of the material. This electron accommodates in the lowest unoccupied electronic state, which corresponds to the conduction band edge or a shallow defect state in the case of a semiconductor and to the Fermi energy in the case of a metal. The lower the energy level of this unoccupied state, the greater the stabilization of the transferred electron and consequently the stronger the hydrogen adsorption free energy. Thus, the energy level of the lowest unoccupied electronic state could be used as a descriptor of the potential of a material for acting as a hydrogen acceptor within the framework of the bifunctional mechanism.

However, these results have been obtained at the semilocal level of theory. For one thing, the RPBE functional used in this work suffers inherently from the self-interaction error and could lead to an inadequate description of charge localization. For another, the overall calculated OER free energy is off by about one electron-volt with respect to the experimental value, which is addressed by correcting the energy of the O_2 molecule. Therefore, we turn to hybrid functionals, which properly reproduce the experimental value of the OER, enhance band gaps, and yield more accurate formation energies in general. This study confirms the correlation between the energy level of the lowest unoccupied state and the hydrogen adsorption free energy, showing an almost identical ordering of the materials according to the considered energy level, see Fig. 5.6. Likewise, the hybrid functional results are largely consistent with the linear scaling relationship between the OER free energy steps. However, for individual materials, the OER free energy steps are strongly modified with respect to the RPBE results, as seen in Fig. 5.4(b). We again observe the reduction of the third OER free energy step ΔG_3 [cf. Fig. 5.2(b)]. However, as the third reaction step is not the reaction limiting step at the hybrid functional level for any of the studied materials, the decrease of ΔG_3 in the bifunctional scheme does not affect the reaction overpotential. Thus the bifunctional mechanism appears to be disfavored with respect to the regular mechanism for our selection of materials. While the absence of overpotential reduction at this level of theory might indeed be just an artefact of our limited set of materials, this nevertheless indicates that the adopted functional is critical when assessing the validity of such a mechanism.

In regard to the band alignment, we find that the hybrid functionals lead to an overall better agreement with experiment for the lowest unoccupied electronic level, except in the case of RuO_2. The data shown in Table 5.1 lead to a mean absolute error of 0.49 eV in the case of RPBE, as compared to 0.27 eV in the case of hybrid functionals. We have modified the fraction of exact exchange used in the hybrid functionals to recover the overall OER free energy. Therefore, the absolute positions of the highest occupied and of the lowest unoccupied electronic level, as well as the size of the band gap, are not expected to match their experimental references. Nevertheless, the modified hybrid functionals used in this work show fractions of Fock exchange not very different from those used in standard PBE0 and HSE06 functionals with $\alpha = 0.25$ and are thus expected to lead to results of higher accuracy compared to RPBE.

We remark that the detailed reaction mechanism has not been addressed in this work. It therefore remains an open question to what extent the two active sites a and b can be brought in proximity in order to promote the reaction through the bifunctional mechanism. Nevertheless, our calculations of the free energy steps associated with the formation of the intermediates support the viability of the bifunctional mechanism proposed by Song *et al.* to interpret their experimental data.[76] Likewise, our work did not consider more complicated effects, such as those related to polaronic defects at the surface or to an explicit treatment of the solvent. Polaronic defects have been found to affect the OER free energy steps in the case of TiO_2 (Ref. [56]) and might similarly be relevant for some of the materials under consideration in this work. The effect of the solvent on the OER free energies has been investigated in detail in the specific case of rutile TiO_2.[137] The second and third

OER steps have been found to be affected by up to 0.5 eV upon explicit consideration of the solvent. However, the sum of these two free energy steps remained practically unchanged, as only the free energy of a single intermediate was noticeably influenced by the solvent. Therefore, the linear scaling relationships are still expected to hold even when the solvent is explicitly considered. Hence, while the calculated OER free energy steps might be subject to variation upon the consideration of an explicit solvent, the general conclusions drawn from the trends observed within this work should remain valid.

We studied the energetic viability of the bifunctional mechanism for the oxygen evolution reaction for a variety of catalyst materials, both at the semilocal and hybrid functional levels of theory. We found that the bifunctional mechanism may lead to the reduction of the OER overpotential for specific combinations of catalysts. At the same time, we observed that the particular functional used is critical for the identification of such favorable pairings of catalysts. Irrespective of the adopted functional, we nevertheless identified a correlation between the energy level of the lowest unoccupied electronic state and the hydrogen adsorption free energy. In this way, the present work introduces a descriptor to guide the search for suitable hydrogen acceptors within the framework of this mechanism. Overall, our work provides support to the bifunctional mechanism as a means to break the linear scaling relationships, which otherwise hinder further reductions.

5.2 The Bifunctional γ-NiOOH/γ-FeOOH Catalyst

The bifunctional mechanism addressed in the previous section was proposed as an explanation of the high catalytic activity of a novel γ-NiOOH/γ-FeOOH catalyst.[76] While the two catalysts appear in an unprecedented configuration, both NiOOH and FeOOH, as well as their combinations, have been given extensive attention as potential OER catalysts in previous studies.[159–163]

Nickel hydroxide $Ni(OH)_2$ has been widely studied as an electrode material for alkaline batteries due to its layered structure and relative abundance. However, when contaminated with iron impurities, its use in batteries was found to be compromised.[164,165] Further studies revealed this to be a consequence of the greatly reduced oxygen evolution overpotential, sparking interest in nickel and iron based electrodes for OER catalysis.[159,166] Indeed, such NiFe electrodes exhibit OER overpotentials below 0.3 eV, leading to activity rates higher by an order of magnitude than what is achievable with conventional catalysts based on iridium oxide.[167,168]

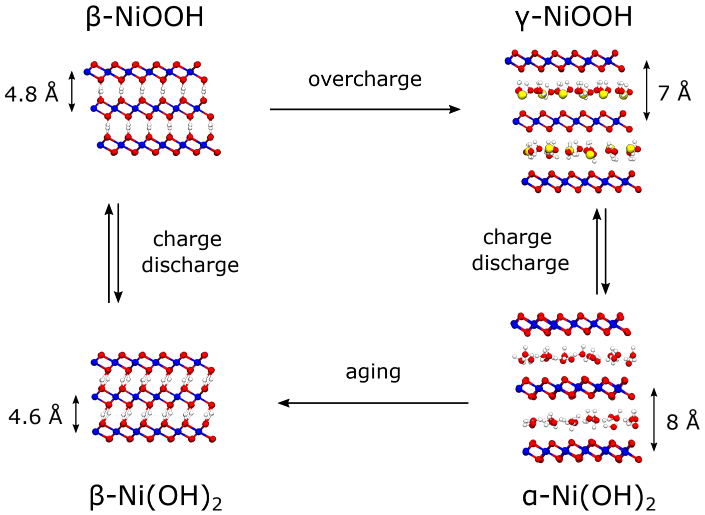

Figure 5.7 – The various phases of nickel hydroxide/oxyhydroxide. The illustrations show the main structural characteristics of each phase.

As already mentioned, nickel hydroxide $Ni(OH)_2$ and nickel oxyhydroxide NiOOH are examples of layered double hydroxides (LDH) on account of their structure. These materials are related through the so-called Bode diagram[169] shown in Fig. 5.7. Under potential bias applied during the OER, NiOOH is formed in two possible phases. The β-NiOOH phase consists of hexagonal NiOOH layers with a relatively small separation. Upon overcharging, the interlayer distance increases, leading to the formation of γ-NiOOH. The larger spacing between fully dehydrogenated NiO_2 layers allows for the intercalation of water molecules and electrolyte ions. Both of these phases have previously been thought of as catalytically active, with the γ phase being considered as the more likely candidate.[159,168]

To understand the low OER overpotentials, the detailed role of iron impurities in NiOOH has been addressed. Several studies point to iron being the active site for the catalysis.[170] It was assumed that iron atoms are substituted for nickel, forming $Ni_{1-x}Fe_xOOH$ compounds, with the value of x in the range of 0.1 to 0.25.[148,167,168] The recent work by Song *et al.* instead rationalizes the high OER activity rates of their electrode in terms of the synergy between catalytically active γ-FeOOH nano-clusters and a γ-NiOOH substrate acting as hydrogen acceptor.[76] While several polymorphs of FeOOH exist, the unifying feature is the presence of FeO_6 octahedra.[163,171]

In this section, we present a systematic study of NiOOH, FeOOH, and their interfaces, and evaluate their potential as possible catalysts within the bifunctional scheme given in Eqs. (5.1). All calculations are carried out with the PBE functional.[84] The rVV10 functional is used to account for the long range interactions between the layers.[124] The other computational parameters are identical to those adopted in Sec. 5.1.

5.2.1 FeOOH

We begin by addressing FeOOH and NiOOH separately. In regard to FeOOH, two polymorphs are investigated. Both exhibit a layered structure of edge-sharing FeO_6 octahedra. The first is γ-FeOOH, or lepidocrocite, and it exhibits an orthorhombic crystal structure. The second studied polymorph is the one adopted in the computational models of Song *et al.*[76] The octahedra are arranged in layers consistent with a trigonal symmetry. Both supercells are relaxed in order to obtain the optimized lattice parameters and the corresponding total energy. We find that lepidocrocite is more stable than the other polymorph by 0.04 eV per atom. Even though entropic effects are neglected in this comparison, we henceforth consider the lepidocrocite structure in further calculations concerning FeOOH in the framework of the CHE method.

To assess the performance of γ-FeOOH in the context of the OER, we use the CHE method to calculate the free energy steps corresponding to the regular mechanism.

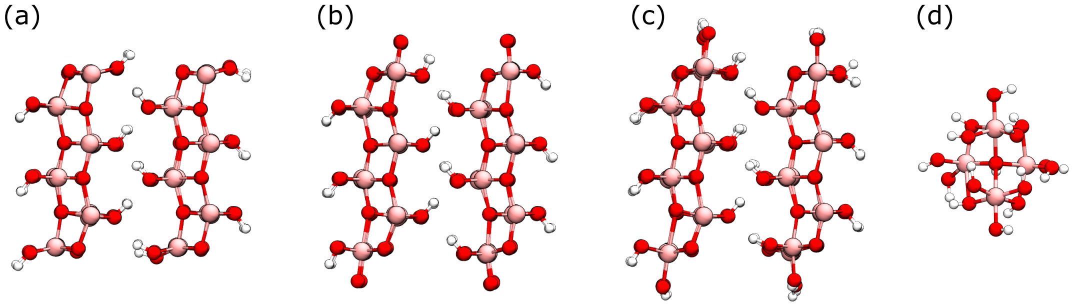

Figure 5.8 – The slab structures considered in this work. (a) Bare γ-FeOOH with Fe atoms exposed on the (100) facet, (b) O covered slab and (c) OH covered slab. The layer configurations are obtained by isolating a single layer from each respective slab structure. (d) FeOOH nanocluster. Iron atoms are shown in pink, oxygen atoms in red, and hydrogen atoms in white.

Several possible γ-FeOOH configurations are studied. First, a slab model is built by exposing the (100) facet of the bulk supercell to 20 Å of vacuum. This choice is made on account of the exposed Fe atoms along edges of the FeOOH layers. The (001) facet has been found to lead to high OER overpotentials in previous studies.[172] Three possible surface terminations are considered: a surface with all Fe atoms being bare, an O covered surface, and an OH covered surface. In the latter two cases, the active site for the OER catalysis is created by exposing a single surface iron atom through the removal of a surface O atom or OH group, respectively. The studied structures are shown in Fig. 5.8(a)-(c). Second, a layer model is obtained by isolating a single lepidocrocite layer from the slab model, with adjacent layers being separated by 20 Å of vacuum. Again, three edge terminations are investigated. In the first, the edge consists of exposed Fe atoms. In the second and third, the edge is terminated by O atoms and OH groups, respectively. Here, we find that the bare-edged layer does not remain structurally sound during relaxation. The unpredictable structural reorganizations prevent a meaningful evaluation of binding energies of the reaction intermediates, which are central to the CHE method. Therefore, the layered model with a bare edge is disregarded. Third, a nanocluster model is considered. Due to the large configuration space, we limit ourselves to clusters consisting of four FeO_6 octahedra extracted from the lepidocrocite structure. Figure 5.8(d) shows one of the considered γ-FeOOH nanoclusters. Three cluster models are investigated in total: the first with all surface oxygen atoms covered with hydrogen [$Fe_4O(OH)_{15}$, cluster 1], the second with a single hydrogen atom removed [$Fe_4O_2(OH)_{14}$, cluster 2], and the third with two hydrogen atoms removed [$Fe_4O_3(OH)_{13}$, cluster 3].

All structures corresponding to the slab, layer, and nanocluster model are relaxed. A surface iron atom is exposed if not already bare by design, and is considered as the active site in the regular OER mechanism. The binding energies of the OH_{ads}, O_{ads}, and OOH_{ads} intermediates are evaluated, and the OER free energy steps calculated. Given the similar configurations of the adsorbates, we assume the thermodynamic corrections to be identical in all studied models. The values given in Table 3.2 are used for all systems. The final free energy steps for each studied model are listed in Table 5.2. As discussed in Sec. 5.1.4, some of the present structures turn out to be favorable candidates within the bifunctional OER scheme. In particular, the O terminated lepidocrocite layer shows low overpotentials on the first and the second OER step, with the third step being the reaction limiting one.

Table 5.2 – The free energy steps ΔG_i corresponding to the regular OER mechanism for all studied FeOOH systems. All values are in eV.

System	ΔG_1	ΔG_2	ΔG_3	ΔG_4
slab	0.76	0.91	1.93	1.32
O covered slab	0.00	1.92	0.82	2.18
OH covered slab	0.79	1.62	1.22	1.29
O terminated layer	0.98	1.10	1.87	0.98
OH terminated layer	0.01	1.47	1.48	1.96
cluster 1	1.27	0.99	2.52	0.13
cluster 2	1.40	1.68	1.42	0.42
cluster 3	0.96	2.05	1.54	0.37

5.2.2 NiOOH

In order to evaluate the free energy steps following the bifunctional OER mechanism, we study NiOOH as a potential hydrogen acceptor. Two polymorphs are generally studied in connection with the OER: β-NiOOH and γ-NiOOH. Both exhibit a trigonal symmetry and consist of NiO_2 layers. In β-NiOOH, the interlayer spacing is small, and one half of the oxygens in the NiO_2 layers are hydrogenated, forming OH groups. In the case of γ-NiOOH, the distance between the layers is large enough for water molecules to intercalate the NiO_2 sheets. Apart from water molecules, electrolyte ions are presumed to be present as well, with concentrations of up to 33%.[173,174] Due to the complexity of modeling such a system, and in the absence of a detailed characterization of the γ-NiOOH structure, we focus solely on β-NiOOH.

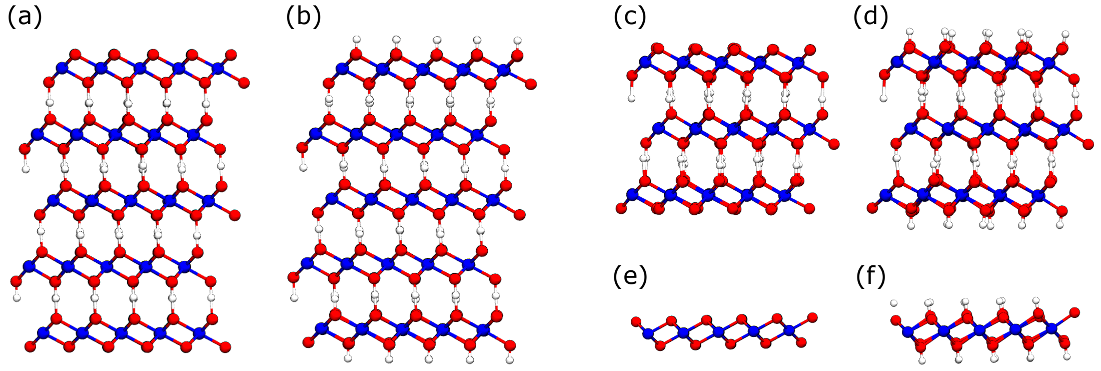

Figure 5.9 – Slab models of β-NiOOH. (a), (c), and (e): Five, three, and one layer models with a bare surface, respectively. (b), (d), and (f): Five, three, and one layer models with a partially hydrogen covered surface, respectively.

Slab models consisting of one, three, and five layers are built. For each choice of slab thickness, two possible surface terminations are considered, for a total of six models. First, a bare outermost NiO_2 layer. Second, a partially hydrogen covered surface layer, such that the overall stoichiometry of NiOOH is preserved. Figure 5.9 illustrates the studied NiOOH models. In all cases, an exposed surface oxygen atom is assumed to be the hydrogen acceptor. All structures are relaxed and the hydrogen binding energy is calculated. As discussed in Sec. 5.1.1, effective anodic conditions are modeled by subtracting the calculated band gap from the total energy of the hydrogen adsorbate H_{ads}. The hydrogen adsorption free energies are listed in Table 5.3. The stoichiometric NiOOH configurations are found to bind hydrogen more weakly, whereas the configurations with bare surfaces bind hydrogen more strongly. The calculated binding energies increase with decreasing slab thickness. Extrapolating from the present set of values, the binding energies for both surface coverages tend to a single value as the number of layers is increased. Since the stoichiometric slab and the slab with the bare surface only differ in the two outermost layers, the two models become more similar with every additional layer. Ultimately, out of the studied models, the 5-layer NiOOH system with the bare surface appears to be the most favorable within the bifunctional scheme on account of the small difference between the hydrogen adsorption energy and the water splitting potential of 1.23 eV.

Table 5.3 – The hydrogen adsorption free energy $\Delta G[\mathrm{H_{ads}}]$ for each NiOOH configuration. To model anodic conditions, the band gap of the dehydrogenated system is subtracted from the total energy of the hydrogenated system in the calculation of the adsorption free energy. All values are in eV.

System	bare surface	stoichiometric
5-layer thick slab	−1.36	−1.06
3-layer thick slab	−1.41	−0.80
single layer	−1.94	−0.82

5.2.3 Bifuncional FeOOH/NiOOH Catalyst

First, the catalytic performance of the FeOOH/NiOOH catalysts in the bifunctional scheme is studied by considering the FeOOH system associated with site a and the NiOOH system associated with site b in separate computational cells. The hydrogen adsorption free energy in Table 5.3 represents the negative of ΔG_4 in the bifunctional mechanism. The first two steps ΔG_1 and ΔG_2 of both the regular mechanism in Eqs. (1.2) and the bifunctional mechanism in Eqs. (5.1) are identical. Finally, given that the overall OER free energy is $\Delta G_{\mathrm{OER}} = 4.92$ eV, the third step ΔG_3 can be calculated as $\Delta G_3 = 4.92 - \Delta G_1 - \Delta G_2 - \Delta G_4$. Hence, combining the results for FeOOH listed in Table 5.2 and for NiOOH in Table 5.3 we obtain the free energy steps corresponding to the bifunctional mechanism for all combinations of the studied systems. The reaction overpotential η for each pairing of FeOOH and NiOOH is shown in Fig. 5.10(a). Figure 5.10(b) draws a comparison between the overpotential achieved with the regular mechanism and the overpotential in the bifunctional scheme. Some combinations of a FeOOH system and a NiOOH substrate exhibit overpotentials above the volcano imposed by the linear scaling relationships. In particular, the combination of the fully hydrogen covered FeOOH nanocluster (cluster 1) and the 5-layer thick bare slab of NiOOH exhibit an overpotential of only 0.13 eV.

The study of the three cluster models, which only differ in the number of hydrogen atoms, shows how sensitive these systems are to the detailed charge conditions. The presence of hydrogen atoms has a twofold effect. First, the extra electron of each additional hydrogen atom affects the charge state of the active iron site. Second, the hydrogen atoms participate in the formation of hydrogen bonds with nearby oxygen atoms, including the OER intermediates. It appears that decreasing the number of hydrogen atoms (and thereby increasing the charge state of the active site) leads to the increase of the second ΔG_2 and the reduction of the third ΔG_3 free energy step, shifting the position of the cluster from the left side of the volcano to the right side in Fig. 5.4. While cluster 2 exhibits the lowest overpotential in the regular OER mechanism, it is cluster 1, the model with all surface O atoms covered by hydrogen, that proves to be the most favorable in the bifunctional scheme.

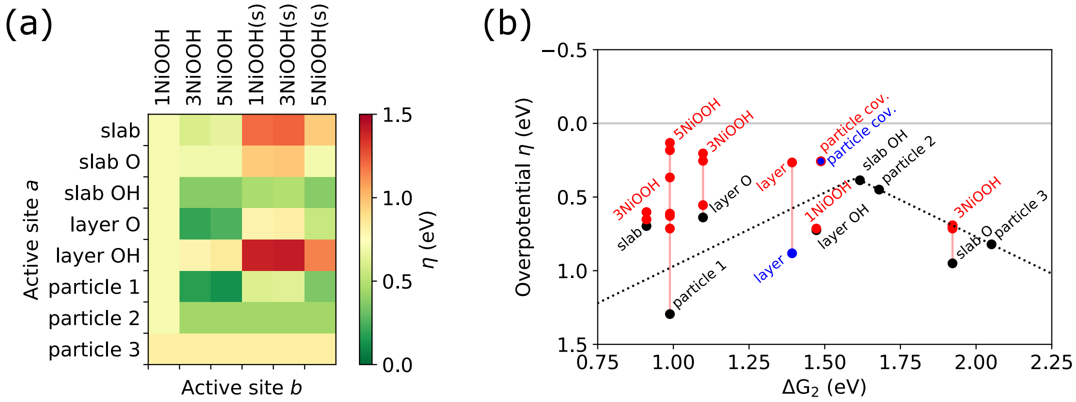

Figure 5.10 – (a) The OER overpotential $\eta \equiv \max_i\{\Delta G_i - 1.23\}$ for $i \in 1,2,3,4$ calculated for each combination of an FeOOH configuration acting as active site a and a NiOOH system acting as site b within the binfunctional OER scheme. The green color signifies a pairing of systems with a very low overpotential. (b) Volcano plot of the OER overpotential η as the function of the second free energy step ΔG_2. The black dots correspond to the regular mechanism, and the labels refer to the respective FeOOH system. The red dots correspond to the bifunctional mechanism, and the labels are only shown for the NiOOH system that leads to the lowest overpotential for the sake of clarity. The blue dots correspond to the joint FeOOH/NiOOH systems.

Given the impressive performance of some pairings of FeOOH and NiOOH when considered separately, the next question that arises is how these catalysts perform when explicitly interfaced. First, we build models consisting of the 5-layer thick NiOOH slab and the FeOOH catalyst physisorbed on its surface. In the case of the oxygen terminated FeOOH layer, the interface with the NiOOH substrate can be formed in a straightforward manner on account of the match between the lattice parameter of lepidocrocite and the NiOOH supercell dimensions. The optimized configuration is shown in Fig. 5.11(a). In the case of the FeOOH nanocluster, it is oriented in such a way that three of the four iron atoms face the NiOOH substrate, see Fig. 5.11(b). Second, a covalent bond between NiOOH and FeOOH is considered, as suggested in the work by Song *et al.*[76] The mismatch between the lattice vectors of the trigonal NiOOH and the orthorhombic γ-FeOOH complicates the construction of a simple model interface. Hence, we only focus on FeOOH nanoclusters attached

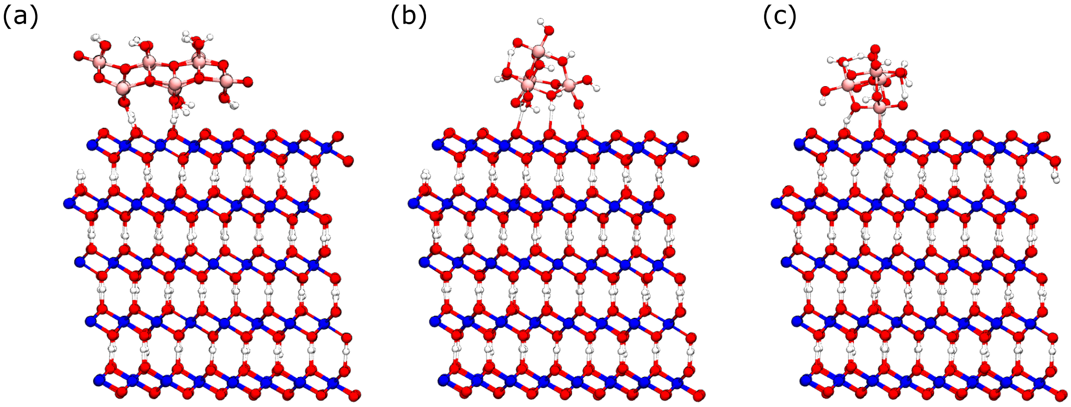

Figure 5.11 – Interfaces between the five layer thick NiOOH slab and a selection of FeOOH configurations: (a) lepidocrocite layer with oxygen terminated edges, (b) FeOOH nanocluster attached to the NiOOH substrate through hydrogen bonds, (c) covalently bound FeOOH nanocluster. Iron atoms are shown in pink, oxygen atoms in red, nickel atoms in blue, and hydrogen atoms in white.

Table 5.4 – The free energy steps ΔG_i following the regular and the bifunctional OER mechanism for all three studied NiOOH/FeOOH interfaces. All values are in eV.

System	ΔG_1	ΔG_2	ΔG_3	ΔG_4
layer regular	1.17	1.39	2.01	0.35
layer bifunctional	1.17	1.39	0.96	1.40
cluster regular	2.61	0.59	0.50	1.22
cluster bifunctional	2.61	0.59	1.10	0.62
cluster cov. regular	1.18	1.49	0.97	1.29
cluster cov. bifunctional	1.18	1.49	1.09	1.17

to the NiOOH surface. The cluster is adsorbed through a single bond between an iron atom in the cluster and a NiOOH surface oxygen atom. The optimized structure is shown in Fig. 5.11(c) The iron atom bound to the surface is considered as the active site. The OER free energy steps are calculated from the binding energies of all reaction intermediates, and are listed in Table 5.4. The reaction overpotentials corresponding to both the regular and the bifunctional mechanism are shown in Fig. 5.10(b).

In the case of the adsorbed FeOOH layer, the free energy steps corresponding to both reaction mechanisms are similar to those achieved for the separate layer and NiOOH substrate. The OER overpotential η in the bifunctional scheme was found to be as low as $\eta = 0.27$ eV. This result suggests that the proximity of the two van der Waals bound catalysts may lead to only a minor modification of the free energy steps achieved with separate computational cells for each material.

In the case of the physisorbed lepidocrocite cluster, the analysis of the bifunctional mechanism was obstructed by the significant structural changes that the cluster underwent upon adsorption. Some of the Fe-O bonds in the cluster were found to break in order to maximize the number of hydrogen bonds formed with the surface. Since the reaction intermediates take part in the formation of hydrogen bonds, this behavior was not universal to all intermediates, and a straightforward calculation of the binding energies of the intermediates is therefore not meaningful. Moreover, in the case of the OOH_{ads} intermediate, the hydrogen atom was found to attach to the NiOOH substrate, and the remaining O-O dimer to detach from the cluster, thereby further complicating the analysis. Since our main goal here is to indetify general trends, we neglect this configuration in further discussions.

Finally, in the case of the covalently bound FeOOH cluster, a very low overpotential was found for both the regular and the bifunctional mechanism. In fact, due to the second reaction step being the reaction limiting one, both mechanisms lead to the same overpotential of $\eta = 0.26$ eV. This suggests that nickel/iron electrodes not only can act as efficient catalysts within the bifunctional scheme, but that they can also exhibit exceedingly small overpotentials in the case of the regular OER mechanism. Furthermore, these findings are of interest in relation to the work by Song *et al.*, in which an iron atom attached to the NiOOH substrate was identified experimentally as the active site of the OER. The studied γ-FeOOH nanocluster on a NiOOH substrate may therefore be a realistic model of the unconventional catalyst observed in the aforementioned work.

While these results are encouraging, several points remain to be addressed. For one thing, the role of the solvent is unknown in the presently studied cases. While the effect of the solvent on the regular OER mechanism was investigated at the TiO_2 interface, it is not yet clear to what extent the findings are applicable in the case of the bifunctional mechanism at the nickel/iron electrode. The solvent can affect the stability of the various reaction intermediates. Moreover, it is unclear how the third step of the bifunctional mechanism, which involves the adsorption of hydrogen on the second active site, proceeds in the presence of water. For another thing, only a limited selection of possible systems and their mutual interfaces was investigated in the present study. The relative stability of the studied systems was not addressed either. Hence, it remains to be seen how realistic the identified interface models are. Nevertheless, our results motivate the further study of the detailed NiOOH/FeOOH catalyst configurations in connection with the bifunctional OER mechanism.

5.2.4 Conclusion

We studied in detail the bifunctional OER mechanism on a NiOOH/FeOOH electrode using the CHE method. A selection of configurations for both FeOOH and NiOOH, including two-dimensional, one-dimensional, and zero-dimensional systems, was investigated in a systematic manner. All possible combinations of the two systems were examined, and detailed interfaces were designed for the best performing ones. A careful analysis of the joint NiOOH/FeOOH catalyst configurations suggests the following. First, the combination of NiOOH and FeOOH can indeed lead to overpotentials at variance with the limitations imposed by the linear scaling laws via the bifunctional OER mechanism. Second, some configurations can achieve these low overpotentials even following the regular mechanism. Both findings support the application of NiOOH/FeOOH based electrocatalysts for efficient water splitting.

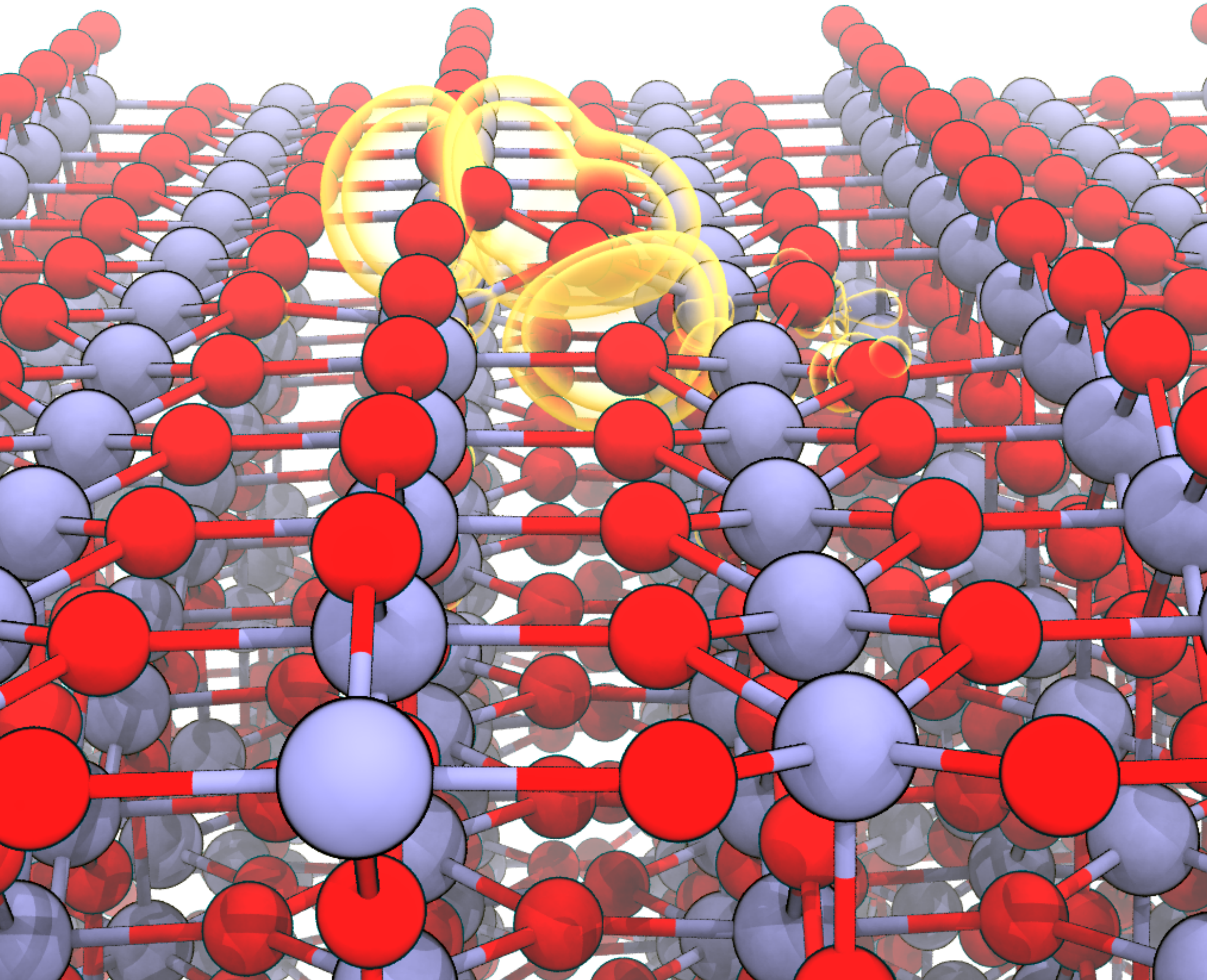

6 Effect of Surface Hole Polarons on the OER at the TiO_2/Water Interface

The universality of the linear scaling relationships has been established through studies of binding energies of OER intermediates on pristine interfaces.[23,31,175] However, surface defects can potentially affect these binding energies, and thus modify the OER free energy steps. Polarons are promising in this regard, as they are ubiquitous in many materials, and affect several aspects related to the OER as well, such as charge trapping,[60,61] charge transport,[64,65] and charge transfer between catalyst and solvent.[57,62,63]

TiO_2 is often studied as a potential OER catalyst,[127] and at the same time, is known to exhibit polaronic defects.[176,177] Polarons in TiO_2 have been studied extensively in connection with the OER mechanism.[178,179] Hole polarons are of special interest, and several studies have investigated charge trapping at the TiO_2 surface.[52,61] Moreover, theoretical studies exploiting more advanced energy functionals invoke the presence of defects in order to explain observed differences between the calculated and the experimental OER overpotential.[49]

In this chapter, we present a surface hole bipolaron consisting of an oxygen dimer, hitherto unstudied on rutile TiO_2. The effect of such polarons on the intermediates of the OER is established using hybrid functional theory. We assess the effect of these polarons on the free energies calculated via the computational hydrogen electrode method. Furthermore, we investigate the stability of the polarons at the hydrated surface adopting a free energy analysis and an explicit solvent. Finally, we calculate the polaron energy level and align it with respect to the redox levels of water splitting in order to better understand the role of the polaron in the OER. The results presented in this chapter have been published in Ref. [56].

Left: Illustration of the electrostatic potential corresponding to the hole bipolaron at the TiO_2 surface.

6.1 Computational Details

All simulation cells consist of a five layer slab of the 4×2 (110) rutile TiO_2 surface. The reaction intermediates are adsorbed on the exposed fivefold coordinated titanium atoms on both sides of the slab with a coverage of 50%. This symmetric arrangement prevents the build-up of electric fields in the direction perpendicular to the interface.[180] Neutral charge conditions are imposed on all simulated systems. The RPBE functional is used at the semilocal level of theory.[86] In order to improve the description of the localized polaronic states we use a modified hybrid density functional.[55,178,181] The fraction of exact exchange in the hybrid PBE0[89] functional is set to 16% so as to reproduce the experimental band gap of 3.3 eV of bulk TiO_2.[182,183] This choice is supported by the finding that hybrid functionals which reproduce the band gap generally provide an accurate description of polarons.[184]

Triple-ζ quality MOLOPT basis sets[93] and GTH pseudopotentials[120] are used for all elements. The plane wave representation of the electronic density uses a cutoff of 700 Ry. The performance of the hybrid functional calculations is improved by adopting the auxiliary density matrix method in conjunction with double-ζ auxiliary basis sets. The molecular dynamics calculations are performed with a simulation time step of 0.5 fs. A Nosé-Hoover thermostat is employed to regulate the temperature, which is set to 350 K. After an initial thermal equilibration, at least 2 ps worth of trajectory is collected.

6.2 Hole Polarons at the Vacuum Interface

We first study the stability of polarons at OH, O, and OOH covered TiO_2 surfaces in vacuum. The initial configurations corresponding to the surface hole polarons are created manually in the following way. The relative distance between a surface plane oxygen atom and a neighboring bridge oxygen atom is reduced to a value of 1.46 Å. These configurations are then optimized. Each polaron consisting of an O-O dimer draws two positive charges, leaving the reaction intermediates in a negative partial charge state. Similar hole O-O bipolarons have been proposed in bulk transition metal oxides, such as anatase TiO_2, V_2O_5, and MoO_3,[185] in bulk amorphous Al_2O_3,[186,187] as well as on the surface of $BiVO_4$.[57] In our calculations we create two such polarons per surface.

Figure 6.1 illustrates the relaxed surfaces with and without polarons. For each reaction intermediate (OH_{ads}, O_{ads}, and OOH_{ads}) the DFT energy difference between the slab with polarons and the corresponding structure without polarons is also given. We find that the OH and OOH covered surfaces are stabilized by the presence of the surface hole polarons. In the case of OH_{ads} this stabilization reaches 1.58 eV per polaron. At variance, the O covered surface is not conducive to the formation of polarons. However, the adsorbate itself relaxes towards the surface and forms a dimer with a surface plane oxygen atom.

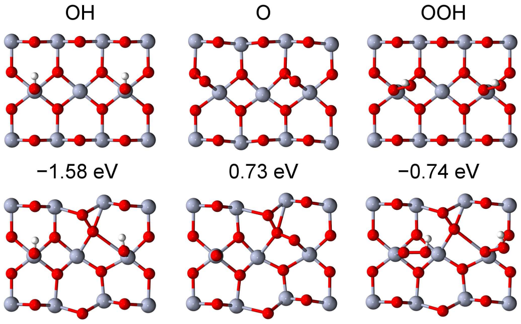

Figure 6.1 – Top view of the relaxed surface layer of the OER intermediates without polarons (top) and with polarons (bottom). Ti atoms are shown in gray, H atoms in white, and O atoms in red. The total energy differences per polaron (ΔE_{pol}) of the OH, O, and OOH covered slabs with and without polarons are shown. A negative sign indicates that the polaron formation leads to a lower total energy.

To gain a better understanding of the polaron formation, we study the electronic structure via the projected density of states (PDOS). The PDOS of the OH covered slabs projected on surface oxygen atoms corresponding to both the case with and without the polaron are shown in Fig. 6.2. In the absence of the polarons, we observe unoccupied levels inside the band gap localized on surface plane oxygen atoms, as well as on subsurface oxygen atoms. Upon the formation of the polarons, a sharp peak appears below the Fermi level (occupied levels). Likewise, we observe a relative increase in the PDOS at the bottom of the conduction band. The unoccupied states in the gap vanish. Hence, the creation of polarons stabilizes the system and pushes the unoccupied levels into the conduction band. A similar behavior is observed for the OOH covered surface.

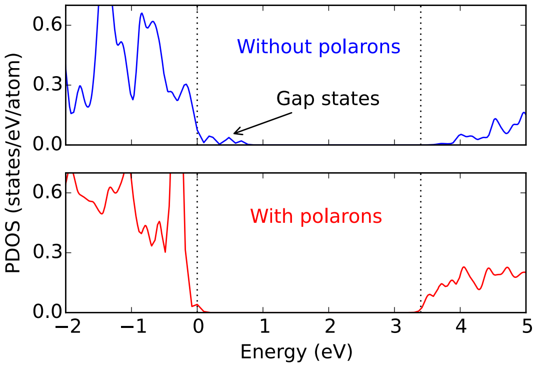

Figure 6.2 – Projected density of states (PDOS) calculated for the OH covered rutile slab without (blue) and with (red) polarons. The density is projected on surface plane oxygen atoms. The projected densities are normalized with respect to the number of surface oxygen atoms. The energies are referred to the highest occupied state.

6.3 Effect on the Free Energy Steps of the OER

By taking into account surface polarons, we can quantify their effect on the energetics of the oxygen evolution reaction. Using the CHE approach, we calculate the free energy differences, ΔG_1 through ΔG_4, corresponding to the four PCET steps in Eqs. (1.2). Our results are given in Table 6.1 and are illustrated in Fig. 6.3. Nozik *et al.* estimated the experimental overpotential of the OER on TiO_2 to lie between 0.9 and 1.1 eV.[127] As seen in the work of Valdés *et al.*,[33] calculations based on the RPBE functional[86] result in overpotentials that agree with the experimental findings. Our results at the RPBE level are consistent with this previous work,[33] demonstrating the reliability of our setup. The small differences on the order of 0.1 eV can be attributed to the different suite of codes adopted and the choice of computational parameters. Next, we recalculate the free energies at the more advanced PBE0 level. As with the RPBE functional, the first step of the OER is the reaction determining step. With the PBE0 functional, the overpotential of this step increases to 1.52 eV, well above the experimental range (0.9–1.1 eV).[127] A similar discrepancy between measured and hybrid-functional overpotentials had been found previously and was attributed to localized charges associated with unidentified defects.[49] Our calculations demonstrate that surface polaron formation indeed reduces the overpotential of the reaction determining step to 0.73 eV, bringing the calculated result back in agreement with experimental observations.[127]

Table 6.1 – Free energy differences corresponding to the four steps of the OER. Energies are given per active site and are in eV.

	Functional	Polarons	ΔG_1	ΔG_2	ΔG_3	ΔG_4
Previous (Ref. [33])	RPBE	No	2.20	1.47	1.55	−0.30
Present	RPBE	No	2.09	1.31	1.63	−0.18
Present	PBE0	No	2.75	1.01	2.22	−1.46
Present	PBE0	Yes	1.96	1.80	1.84	−1.09

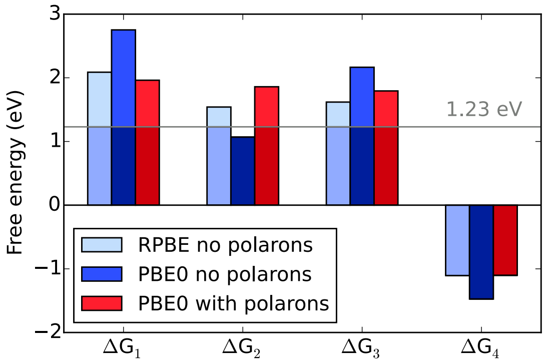

Figure 6.3 – Gibbs free energy steps corresponding to the intermediates of the OER on r-TiO_2. The gray line indicates the standard potential of water splitting.

6.4 Hole Polarons at the TiO_2/Water Interface

We now address the stability of surface polarons at the hydrated surface. To this end, we first carry out two MD simulations of the OH_{ads} intermediate at the hybrid functional level with explicit water solvent starting from different initial configurations. In the first one, the structure does not show any polaron, whereas four of them are present in the second one. The potential energy of the system is shown as a function of time in Fig. 6.4(a). The energy of the structure with polarons is lower by about 1 eV per polaron with respect to the surface without polarons. However, we do not observe spontaneous polaron formation over a MD duration of 3.5 ps. This is consistent with the presence of an energy barrier preventing the formation of the defect on the time scales we are able to sample.

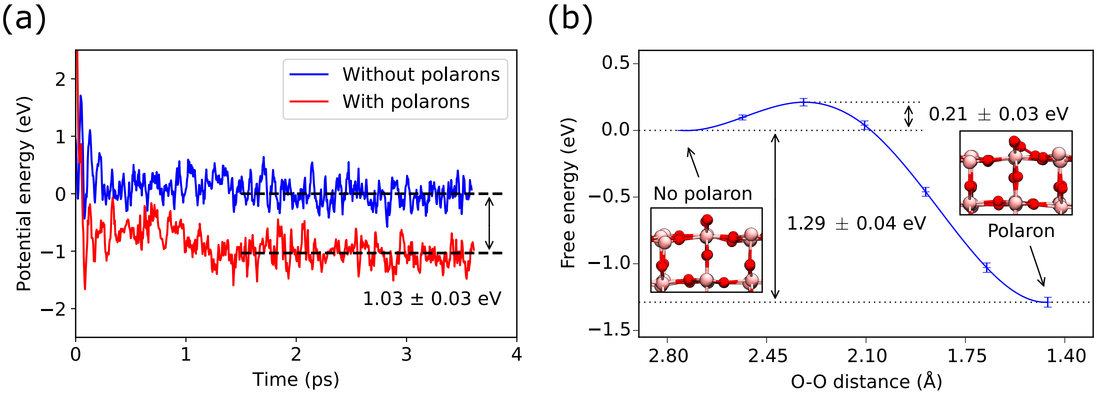

Figure 6.4 – (a) Potential energy of the solvated system with the polaron (red curve) and without the polaron (blue curve) over the duration of the simulation. The average energy in the case without the polarons is chosen as the zero reference. In both cases the average energy is highlighted by a dashed line, and the energies are scaled by a factor of 1/4 so that their difference represents the energy difference per polaron. (b) Free energy profile of the O-O bipolaron formation achieved by the Blue Moon sampling scheme.

To properly assess the relative stability of the two structures, we hence perform a free energy analysis via the Blue Moon sampling scheme[110] described in Sec. 2.4. The distance between the surface oxygen atoms associated with polaron formation is varied between 2.76 Å and 1.46 Å, which corresponds to the case without the polaron and with the polaron, respectively. The initial and final configurations are shown in the insets of Fig. 6.4(b). The reaction coordinate ξ, corresponding to the O-O distance, is sampled with seven values. For each value of ξ, the distance between the involved O atoms is fixed and a constrained MD simulation is carried out. Due to the fast equilibration times, only 0.75 ps worth of trajectory is accumulated. The force acting on the constraint as a function of simulation time is shown in Fig 6.5(a), and Fig 6.5(b) shows the converged forces as a function of the reaction coordinate ξ. The errors on the forces are computed through a blocking analysis.

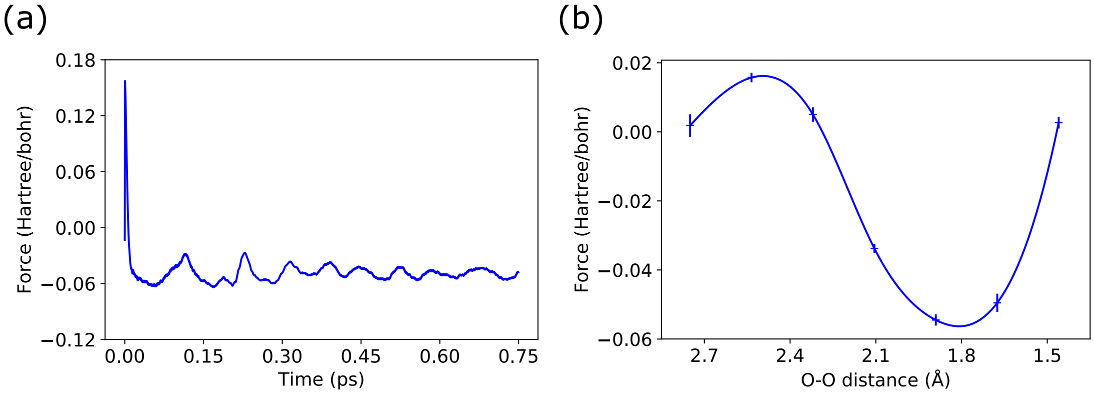

Figure 6.5 – (a) Lagrange coefficient, or force acting on the constraint, as a function of simulation time for the choice of the reaction coordinate $\xi = 1.675$ Å. (b) Average force for each value of ξ. The interpolating spline only acts as a guide to the eye.

By integrating the resulting forces along the reaction coordinate, we obtain the free energy profile in Fig. 6.4(b). The free energy of the structure with the polaron is indeed lower than in the case without the polaron, following the same trend observed for the total energies. We find a free energy difference of 1.29 ± 0.04 eV, to be compared with the value of 1.58 eV obtained above for the surface in vacuum and using the CHE approach. The effect of the water solvent can thus be estimated to be about 0.3 eV. The calculated free energy profile also reveals that there is a barrier of 0.21 ± 0.03 eV for polaron formation at the hydrated surface. This free energy barrier makes spontaneous polaron formation improbable in MD simulations lasting only a few picoseconds, consistent with our observations. However, this barrier is sufficiently low to allow for the thermal generation of surface polarons at room temperature.

6.5 Polaron Energy Level Alignment

As discussed in Chapter 1 and illustrated in Fig. 1.1, a suitable water splitting catalyst must exhibit conduction and valence band edges straddling the redox levels of hydrogen reduction and water oxidation in liquid water. In the context of the OER on rutile TiO_2, the valence band edge is required to be lower in energy than the water oxidation level. Both theoretical calculations[118,188] and experimental studies[182,189,190] lend support to this arrangement of the energy levels. However, the presence of surface defects introduces defect levels inside the band gap. In the case of surface hole polarons, these act as hole traps. If the charge transition level corresponding to the defect lies above the water oxidation redox level, the catalytic efficiency of such a defective material is inhibited.

The charge transition level is calculated via a grandcanonical formalism developed for defects in crystals[191,192] and adapted to interfaces.[57] The charge transition level $\mu(q/q')$ between charge state q and q' of a defect X is given by the Fermi energy E_F for which the formation energies of the two charge states are identical:

$$\mu(q/q') = \frac{E^\mathrm{f}_q[X] - E^\mathrm{f}_{q'}[X] + \Delta E_\mathrm{corr}}{q' - q} - \epsilon_v, \tag{6.1}$$

where $E^\mathrm{f}_q[X]$ and $E^\mathrm{f}_{q'}[X]$ are the formation energies calculated with the Fermi level at the valence band maximum $E_\mathrm{F} = \epsilon_v$, ΔE_corr is the difference between the finite size corrections in each charge state of the system, and ϵ_v is the valence band edge of the pristine material. In the present case, the relevant charge transition is between pristine rutile TiO_2 under neutral charge conditions $q' = 0$ and the system with the bipolaron in charge state $q = +2$:

$$\mu(+2/0) = \frac{E^\mathrm{f}_{+2}[\mathrm{polaron}] - E^\mathrm{f}_0[\mathrm{pristine}] + \Delta E_\mathrm{corr}}{-2} - \epsilon_v. \tag{6.2}$$

Since the formation energy of pristine TiO_2 is zero, $E^\mathrm{f}_0[\mathrm{pristine}] \equiv 0$, the above expression further simplifies to:

$$\mu(+2/0) = \frac{E^\mathrm{f}_{+2}[\mathrm{polaron}] + \Delta E_\mathrm{corr}}{-2} - \epsilon_v. \tag{6.3}$$

Finally, using the valence band maximum as reference for the polaron level position, we find:

$$\mu(+2/0) = \frac{E^{\mathrm{f}}_{+2}[\text{polaron}] + \Delta E_{\text{corr}}}{-2}. \tag{6.4}$$

Here, the formation energy of the polaron is calculated as the difference between the total energy of the system with the polaron and without the polaron in the same charge state +2:

$$E^{\mathrm{f}}_{+2}[\text{polaron}] = E^{\text{tot}}_{+2}[\text{polaron}] - E^{\text{tot}}_{+2}[\text{pristine}]. \tag{6.5}$$

Alternatively, the total energy of the pristine system in the +2 charge state can be obtained from the total energy of the pristine system under neutral conditions with two electrons nominally removed from the valence band:

$$\tilde{E}^{\mathrm{f}}_{+2}[\text{polaron}] = E^{\text{tot}}_{+2}[\text{polaron}] - E^{\text{tot}}_{0}[\text{pristine}] + 2\epsilon_v. \tag{6.6}$$

We will use a tilde to decorate quantities obtained in relation to the above equation instead of Eq. (6.5).

In this section, we determine the position of the charge transition level corresponding to the surface hole bipolaron with respect to the band edges of rutile TiO_2.

6.5.1 Results

The formation energy in Eq. (6.6) is calculated by performing two calculations of the TiO_2 interface model with vacuum at the hybrid functional level of theory. In one of the calculations the total charge is kept neutral and the polaron is absent. In the other, a single polaron is present and a charge state of +2 is enforced. The valence band maximum in Eq. (6.6) is obtained by aligning the average electrostatic potential in the center of the pristine interface with that of the bulk material. The formation energy of the polaron is found to be $\tilde{E}^{\mathrm{f}}_{+2} = 0.17$ eV. The positive value indicates that the polaron should not be stable. An extra calculation of the pristine system in the +2 charge state is performed to calculate the formation energy in Eq. (6.5), and a value of $E^{\mathrm{f}}_{+2} = -1.62$ eV is obtained.

The finite size correction in Eq. (6.3) is computed following the procedure developed by Komsa *et al.*[145] A model dielectric interface is built as shown in Fig. 6.6(a). The static dielectric constant ϵ_0 of TiO_2 is calculated at the hybrid functional level of theory by performing simulations of bulk TiO_2 in the presence of an electric field. A value of $\epsilon_0 = 24.5$ is found, see Fig. 6.7. Even though the experimental values reported in the literature vary greatly (from 31 to 110),[193–195] we here use the calculated one to remain consistent with the adopted computational scheme. The polaron is modeled by a Gaussian charge distribution with charge $q = +2$ and a width of $\sigma = 0.4$ Å. For these values, the model electrostatic potential and the DFT potential are aligned in the vacuum region, see Fig. 6.6(a). Next, the model system is uniformly scaled by a scaling factor α. The finite size correction is obtained as the difference between the dilute limit of the electrostatic energy and the energy of the initial model system, as illustrated in Fig. 6.6(b). The finite size correction term ΔE^{corr} in Eq. (6.3) thus assumes the value $\Delta\tilde{E}^{\mathrm{corr}} = -1.41$ eV. In the case when the charged system is used as a reference, the finite size correction scheme needs to be applied to both the system with and the system without the polaron. In the latter case, a model containing a charge distributed uniformly across the slab is used, see Fig. 6.8. The finite size correction in Eq. (6.4) consists of a contribution from the system with the polaron $\Delta E^{\mathrm{pol}}_{\mathrm{corr}}$, and from the uniformly charged system $\Delta E^{+2}_{\mathrm{corr}}$. We find a value of $\Delta E^{\mathrm{corr}} = -1.41\ \mathrm{eV} + 1.73\ \mathrm{eV} = 0.33$ eV.

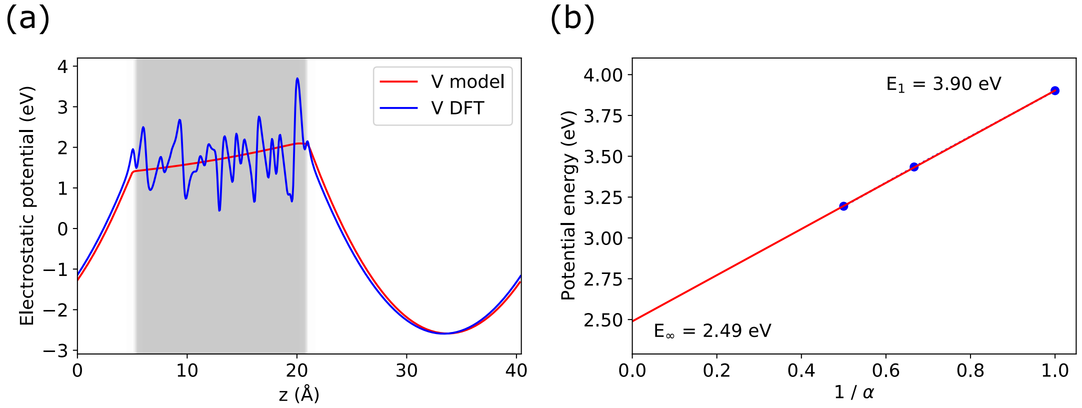

Figure 6.6 – (a) The model electrostatic interface between a TiO_2 slab with $\epsilon_0 = 24.5$ (shown in grey) and vacuum. The electrostatic potential projected along the axis perpendicular to the interface for a Gaussian charge distribution is shown in red. The potential obtained in the DFT simulation of the polaron is shown in blue. (b) The total electrostatic energy of the model system as a function of the inverse scaling parameter α. All dimensions of the model dielectric interface are uniformly scaled by α to obtain the dilute limit E_∞ by extrapolation. A correction of $\Delta E^{\mathrm{pol}}_{\mathrm{corr}} = -1.41$ eV is found.

Using a neutral reference system to calculate the polaron formation energy according to Eq. (6.6), a value of $\tilde{\mu} = 0.62$ eV above the valence band maximum is obtained for

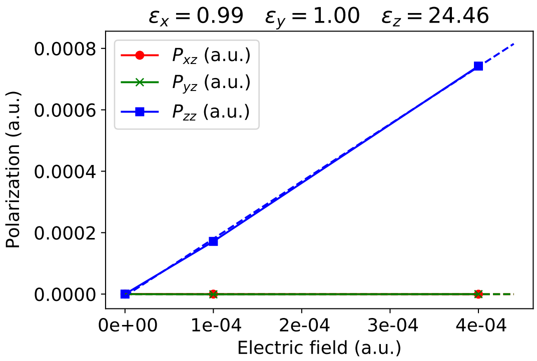

Figure 6.7 – Components of the polarization tensor of bulk TiO_2 under an electric field. The direction of the electric field coincides with the direction perpendicular to the surface in the vacuum interface models. The static dielectric constant is calculated as $\epsilon = 1 + 4\pi\chi$, where the susceptibility χ represents the slope of the dashed line obtained by linear regression.

Table 6.2 – Formation energies and polaron levels obtained for the original and the scaled-up TiO_2 slab, as well as the values in the dilute limit achieved through extrapolation. All values are in eV.

quantity	original	scaled-up	dilute limit
E^{f}_{+2}[polaron] uncorrected	−1.62	−1.82	−2.20
$\tilde{E}^{\mathrm{f}}_{+2}$[polaron] uncorrected	0.17	−0.82	−2.80
E^{f}_{+2}[polaron] corrected	−1.30	−1.60	−2.20
$\tilde{E}^{\mathrm{f}}_{+2}$[polaron] corrected	−1.24	−1.72	−2.80
μ uncorrected	0.81	0.91	1.10
$\tilde{\mu}$ uncorrected	−0.08	0.41	1.40
μ corrected	0.65	0.80	1.10
$\tilde{\mu}$ corrected	0.62	0.88	1.40

the polaron charge transition level. Instead, using the charged reference system through Eq. (6.5), the polaron level is found to be located $\mu = 0.65$ eV above the valence band maximum. While the formation energies calculated using the two different approaches are very different, the account of the finite size corrections leads to near identical polaron energy levels. All relevant values are listed in Table 6.2

An analysis of the charge density obtained from the polaron DFT simulation shows that the charge is not localized exclusively in the vicinity of the polaron. Figure 6.9(a) draws a comparison between the calculated and the model charge distributions. The model adopted in the finite size correction scheme appears to be insufficient to accurately describe the simulated system. Hence, in order to verify the performance

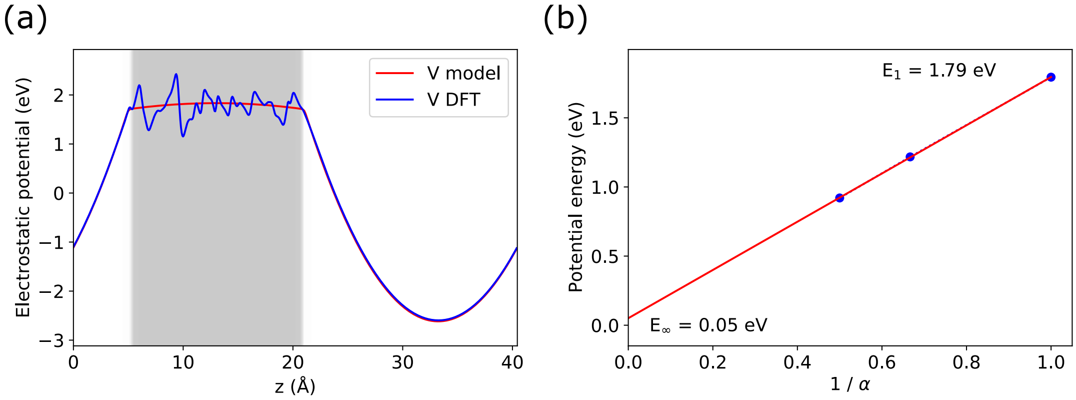

Figure 6.8 – (a) The model electrostatic interface between a TiO_2 slab with $\epsilon_0 = 24.5$ (shown in grey) and vacuum. The electrostatic potential projected along the axis perpendicular to the interface for a uniform charge distribution is shown in red. The potential obtained in the DFT simulation of the charged slab is shown in blue. (b) The total electrostatic energy of the model system as a function of the inverse scaling parameter α. All dimensions of the model dielectric interface are uniformly scaled by α to obtain the dilute limit E_∞ by extrapolation. A correction of $\Delta E^{+2}_{\mathrm{corr}} = -1.74$ eV is found.

of the finite size correction method, and to understand the large difference between the formation energies calculated via the two approaches in Eqs. (6.5) and (6.6), we perform calculations of a scaled-up TiO_2 slab. All dimensions of the slab, as well as the thickness of the vacuum region, are increased by 50%, resulting in a seven layer thick slab with a 4×8 surface repeat cell. The optimized geometries corresponding to the neutral system, and to the charged system with and without polaron, are obtained.

The calculated polaron energy levels obtained using both alternatives of achieving the polaron formation energy are shown in Fig. 6.9(b). Both the results with and without the finite size corrections are shown. The value corresponding to the dilute limit in the two cases is different. In the case of the charged system used as reference, an extrapolated value of $\mu = 1.10$ eV is found. In the case of the neutral reference, we instead find a value of $\tilde{\mu} = 1.40$ eV. In both cases, the corrected and the uncorrected energy levels lead to the same asymptotic values. All relevant quantities are listed in Table 6.2. The finite size effects appear to be insufficiently suppressed by the adopted correction scheme, as the scaling of the energy levels persists despite the corrections. Hence, we rely on the value obtained by extrapolation from the uncorrected polaron levels. A value of $\mu = 1.25 \pm 0.2$ eV is found as the mean of the dilute limits corresponding to the two approaches of calculating the formation energy. The uncertainty is given by the standard error.

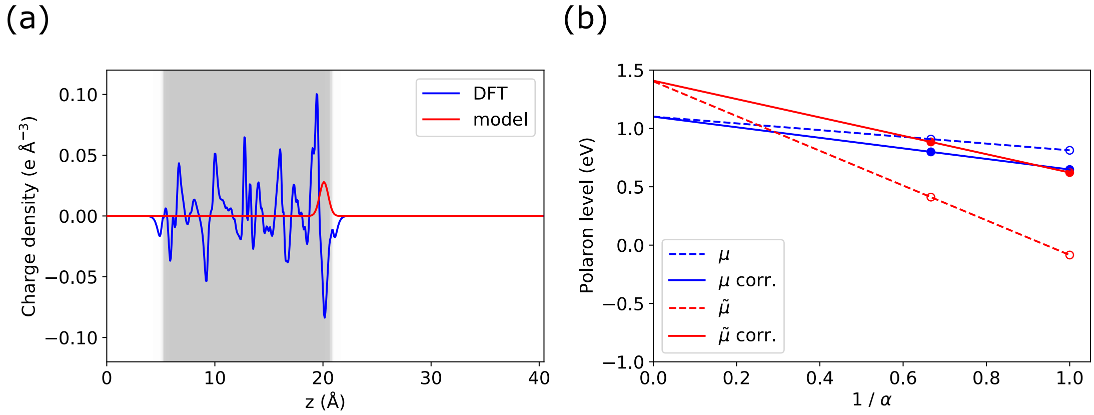

Figure 6.9 – (a) Projection of the charge density along the direction normal to the interface obtained from the DFT calculation and from the electrostatic model. (b) The polaron energy level as a function of the inverse scaling parameter α. The blue and the red color correspond to the case where the charged and the neutral systems are used as the reference to calculate the polaron formation energies, respectively. The full lines correspond to the results obtained with the finite size corrections.

In order to assess the position of the polaron level at the interface with water, we use the dielectric model to obtain total energies corresponding to identical Guassian charge distributions at an interface with a material with $\epsilon = 1$ (vacuum), and with $\epsilon = 78.5$ (water).[196] Due to the superior screening of the model water layer, the charge distribution representing the polaron is stabilized with respect to the vacuum interface by an amount of 1.26 eV in the dilute limit. Hence, we approximate the polaron formation energy at the solvated interface by subtracting 1.26 eV from the value obtained at the vacuum interface. Consequently, as per Eq. (6.4), the defect level moves up by an amount equal to one half of this stabilization, or 0.63 eV, with respect to the valence band edge of TiO_2. Hence, the polaron level at the water interface achieves a value of $\mu = 1.25$ eV $+ 0.63$ eV $= 1.88$ eV above the valence band. To accurately determine the alignment of the polaron energy level with respect to the redox levels of water, we use the valence band edge position obtained using the PBE0(α) functional for the rutile TiO_2/water interface by Guo *et al.*[118] The valence band is located 2.59 eV below the SHE. Figure 6.10 shows the position of the polaron level with respect to the water oxidation and hydrogen reduction levels. Note that the SHE is used as the reference, with the polaron level corrected for the presence of the solvent located 0.71 eV below the SHE. The polaron energy level is thus found to lie above the water oxidation level H_2O/O_2, and should thus act as a hole trap.

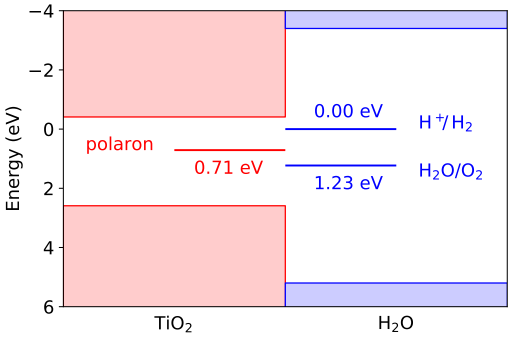

Figure 6.10 – Alignment of the polaron energy level at the TiO_2/water interface with respect to the redox levels of water splitting. The energy scale uses the SHE (H^+/H_2) as reference.

6.6 Conclusion

We have studied the formation of polarons on the surface of rutile TiO_2 under OER conditions. The strongly electronegative reaction intermediates attract electrons from the substrate, generating holes in the vicinity of the surface. These holes can then form surface bipolarons consisting of two surface oxygen atoms. The presence of these polarons stabilizes the corresponding reaction intermediates, and thus affects the free energy steps ΔG calculated in the CHE scheme. Our results also help explaining why previous studies performed at the hybrid functional level have lead to values of ΔG at variance with the experimental evidence. The extra stabilization due to the polarons leads to free energy steps that are in accord with the experimental data.

The stability of the polarons was assessed at the solvated interface at finite temperature. AIMD simulations of the TiO_2/water interface confirmed the existence of the proposed polarons. Further calculations following the Blue Moon sampling scheme have been used to obtain the free energy profile of the polaron formation under realistic conditions. A small energy barrier was found to inhibit the spontaneous polaron formation in the short times available to computational sampling, explaining the absence of these polarons in previous literature.

Finally, the energy level of the polaron was calculated. Through an extrapolation scheme, the formation energy and the polaron level were determined in the dilute limit, and the stability of the polaron was ascertained. Next, the energy levels were aligned with respect to the relevant OER redox level. The level was found to lie above the H_2O/O_2 redox level. Hence, holes may travel to the surface and be trapped in the dimers, disqualifying them from taking part in the water splitting reaction.

In summary, we demonstrated that the intermediates of the oxygen evolution reaction stabilize hole polarons at the rutile TiO_2 surface. When polarons are considered, the calculated overpotential of the reaction determining step is found to be lowered and to agree with experiment. The occurrence of polarons is material specific and affects the binding energies of the adsorbates. This effect is not considered in the linear scaling relationships, which limit the efficiency of the oxygen evolution reaction. Hence, polaron formation could partially overcome such limitations and should be systematically addressed in materials searches for the optimal catalyst.

7 Conclusion

In this work we have studied the oxygen evolution reaction through free energy calculations of the reaction intermediates. First, we presented the current state-of-the art, the computational hydrogen electrode method, and demonstrated the emergence of linear scaling laws between the free energy steps of the OER using a set of materials consisting mainly of transition metal oxides. This linear scaling law was found to be robust with respect to the choice of the energy functional. Calculations performed at the hybrid functional level of theory lead to free energies that exhibit a scaling relationship similar to that observed using semilocal functionals. Nevertheless, the individual free energy steps for a given material evaluated using the hybrid functionals were found to exhibit differences of up to 2.3 eV with respect to the values obtained at the semilocal level of theory. Not only were the free energy steps modified quantitatively, but qualitative changes of the reaction steps were observed as well, highlighting the importance of the adopted level of theory when evaluating potential catalysts.

Despite the strong dependence on the adopted functional, the CHE approach proved to be a helpful tool in conjunction with an explanatory computational method. We have shown that the comparatively straightforward CHE method complements well the computationally more expensive constant Fermi level molecular dynamics scheme. The latter was used to achieve a realistic description of the Pt/water interface under potential bias. The OER was found to take place spontaneously under these conditions. However, the observed reaction mechanism was not the commonly assumed one. The CHE method allowed us to calculate the free energy steps corresponding to both the conventional and the newly observed reaction pathway, and to confirm the viability of the novel reaction mechanism.

While the low computational cost, straightforward formulation, and versatility justify the use of the CHE approach as the state-of-the-art free energy method, the validity of the obtained results is ambiguous on the account of several drawbacks inherent to the standard formulation of the method. Among the most important is the partial or complete neglect of solvent effects. Hence, we have decided to assess the performance of the CHE approach *vis-à-vis* a more advanced formalism that takes the solvent into account. To this end, we have developed a formalism based on thermodynamic integration and Blue Moon sampling that allowed us to evaluate the free energies corresponding to the PCET steps at finite temperatures and in the presence of the explicit solvent. We chose TiO_2 as the benchmark material. The OER free energy steps were calculated using the CHE method in the absence of water molecules, and using the TI approach both in the absence and in the presence of liquid water. The two methods yielded practically identical free energy steps for the vacuum interface, with minor differences on the order of 0.1 eV. In contrast, the inclusion of the solvent was found to modify the second free energy step, associated with the formation of O_{ads}, by more than 0.5 eV.

To understand the effect of the solvent on the OER energies, we have performed a structural analysis of the trajectories corresponding to all reaction intermediates. The examination based on hydrogen bond counting has proved to be inconclusive. While each intermediate was stabilized by a different number of hydrogen bonds, only O_{ads} was found to be greatly affected by the solvent. Unlike the other reaction intermediates (OH_{ads}, OOH_{ads}, H_2O_{2ads}), the adsorbed oxygen atom attracted two electrons instead of one. Hence, an explanation based on electrostatic effects was proposed, and several supplemental tests were carried out. First, a Wannier function analysis revealed that, indeed, an extra electron is localized in the O_{ads} intermediate as compared to the other adsorbates. Next, the oxygen atom in the O_{ads} intermediate was replaced by a fluorine atom. Given the electronic configuration of fluorine, only a single electron from the TiO_2 slab was localized in the adsorbate. As a consequence, the solvent stabilization in the case of F_{ads} was found to be lower than in the case of O_{ads} by 1.4 eV. Finally, we performed electrostatic simulations of a model dielectric interface with a Gaussian charge distribution representing the various OER intermediates in the presence and absence of the solvent. Again, the extra stabilization of a +2 charge distribution at the solvated interface with respect to a +1 charge amounted to 1.5 eV, in accord with the previous test. These results corroborate the hypothesis that the effect of the solvent on the OER free energies can be understood mainly through electrostatic effects. Overall, this work supports the viability of applying the CHE method to the OER at solvated interfaces, provided proper attention is given to the charge states of the reaction intermediates.

Having validated the method, we applied the CHE in order to investigate a bifunctional mechanism for the OER. The regular OER mechanism relies on a single active site, leading to the emergence of linear scaling laws due to the relations between the binding energies of the reaction intermediates. In particular, the sum of the second and third free energy steps remains constant across large sets of materials, and assumes a value which imposes an overpotential on at least one of the two reaction steps involved. At variance, the bifunctional mechanism relies on two close but qualitatively different active sites. The formation of the OOH_{ads} intermediate, the third reaction step of the regular mechanism, and often the reaction limiting step, is avoided through the formation of H_{ads} on the second active site. This makes it possible to search for pairings of catalysts that exhibit efficiencies above the limitations imposed by the linear scaling relationships. We first studied the bifunctional mechanism for a set of materials consisting of rutile TiO_2, anatase TiO_2, SnO_2, RuO_2, IrO_2, Ni_2P, and $BiVO_4$. Instead of investigating the detailed reaction mechanism for realistic configurations of the two active sites, we focused on general trends to gain a better understanding of the bifunctional scheme.

First, we analyzed how the adoption of anodic conditions affects the reaction intermediates of the bifunctional mechanism. We modeled the anode by removing electrons from the simulated system, creating valence band holes. While the electronegative adsorbates present in the regular mechanism were affected to a minimal degree, the binding energy of the H_{ads} intermediate specific to the bifunctional mechanism was greatly modified by the adoption of anodic conditions. We rationalized this in terms of the propensity of the H atom to give up its electron upon adsorption. While in neutral conditions this electron accommodates in the conduction band of the substrate, under anodic conditions this electron recombines with a valence band hole, conferring an extra stabilization commensurate to the band gap of the system. Hence, to properly address the anodic conditions in further calculations, we reduced the total energy of the H_{ads} by the band gap of the substrate.

Next, for each catalyst in the studied set acting as the first active site, we considered every other material as a possible hydrogen acceptor representing the second active site in the bifunctional mechanism. A total of 49 pairings was investigated both at the semilocal and the hybrid functional level of theory. Using the semilocal functional, we found that several combinations lead to OER overpotentials lower than those associated with the regular mechanism. However, the hybrid functional results did not confirm any of these favorable pairings. While the use of hybrid functionals prevented the need for *ad-hoc* corrections to the calculated free energy steps, it generally resulted in an overestimation of the band gap, and by extension, of the binding energy of H_{ads} under anodic conditions. This finding highlights the importance of the choice of energy functional in the investigation of the bifunctional mechanism.

While none of the studied pairings produced overpotentials above the volcano imposed by the linear scaling relationships, the existence of such favorable combinations of catalysts cannot be ruled out. Our investigation culminated in the formulation of the following criteria for the bifunctional mechanism to be favored. First, the reaction limiting step in the regular mechanism must be the third one (OOH_{ads} formation), and the first and second steps should have as low overpotentials as possible. Second, the hydrogen acceptor must bind the hydrogen such that its binding energy is around 1.23 eV. Given the correlation between the valence band edge position and the hydrogen binding energy, a suitable hydrogen acceptor should exhibit a valence band edge around 6.5 eV below the vacuum level. These findings support the viability of the bifunctional mechanism and can be used in future searches for highly efficient bifunctional catalysts.

These general findings were then applied to the case of the highly efficient nickel/iron catalyst implicated in overcoming the linear scaling laws in conjunction with the bifunctional OER mechanism. Several configurations of both γ-FeOOH and NiOOH were investigated separately, and the approach adopted previously was used to identify the highest performing pairings. For these combinations, fully atomistic interfaces between the two materials were built and the OER free energy steps were re-evaluated. Several structures were found to lead to overpotentials superior to those of conventional catalysts. A specific configuration exhibited an overpotential of only $\eta = 0.26$ eV not only in connection with the bifunctional reaction mechanism, but also following the conventional reaction pathway, thereby further supporting the excellent catalytic performance of nickel/iron based catalysts.

In addition to the bifunctional mechanism, we investigated a second avenue of breaking the linear scaling relationships. Unlike the universal linear scaling relationships, polarons are material specific. Hence, we studied surface hole polarons in rutile TiO_2 and evaluated their effect on the OER free energy steps. The strongly electronegative OER intermediates attract electrons from the bulk of the substrate, leaving behind holes. These holes were found to trap on the surface, where they formed hole bipolarons in the form of O-O dimers. The formation of the dimers was observed for all reaction intermediates. Taking these polarons into account, the free energy steps evaluated at the hybrid functional level of theory were modified by up to 0.7 eV, reducing the reaction overpotential to a value in accord with the experimental reference.

These O-O dimers were found to be stable at the interface with water at finite temperature through MD simulations with explicit water molecules. We also performed Blue Moon calculations to obtain the free energy profile of the polaron formation. A small barrier of 0.2 eV was found to prevent the spontaneous polaron formation on the short time scales achievable using hybrid functional MD. However, the relatively small size of the barrier enables the spontaneous formation of the polarons at room temperature. We obtained a value of 1.4 eV for the formation free energy of the O-O dimers.

While these results were encouraging, finite size effects related to simulation cell size needed to be taken into account as well in order to establish the stability of the polaron. We calculated the position of the polaron level with respect to the band edges of TiO_2. We used both a finite size correction scheme, as well as an extrapolation scheme employing a scaled up simulation cell. Whereas the adopted finite size correction scheme proved insufficient, the extrapolation procedure enabled us to determine the location of the polaron level with respect to the valence band maximum. This, in turn, allowed us to align the position of the level relative to the redox levels of water splitting. We found that due to the polaron level lying above the H_2O/O_2 level in liquid water, the polaron likely acts as a hole trap, capturing holes at the surface but preventing them from participating in the OER.

In conclusion, this work addressed the issue of linear scaling relationships limiting the catalytic efficiency of the OER. We used computational methods to gain insight into the emergence of the linear scaling relationships, and subsequently investigated means of overcoming them. On the one hand, polarons were investigated in terms of their effect on the free energy steps corresponding to the OER. On the other hand, a bifunctional OER mechanism involving two functionally different active sites was studied on account of its potential to completely avoid the linear scaling relationships inherent to the commonly adopted reaction mechanism. Since the presence of polarons is material specific, it is difficult to account for them *a priori* when searching for novel catalysts. Nevertheless, once a detailed model of the active interface is known, the stability of polarons and their effect on the OER should be carefully investigated. At variance, the bifunctional reaction scheme opens up a new avenue in the ongoing search for highly efficient OER catalysts by enabling rapid evaluation of material pairings which can achieve unconventionally low OER overpotentials. We are hopeful that the results presented here may help guiding the discovery of novel catalysts for water splitting, and contributing in this way to the vision of renewable and clean energy in the future.

Several points of interest remain to be addressed in the future, broadly falling into two categories. The first is related to the methodology. While the linear scaling relationships were found to be functional independent, the actual OER free energy steps, and therefore the predicted catalytic performance of any specific material, show a critical dependence on the choice of the density functional and thus limit the predictive power of DFT calculations. Moreover, the inclusion of the solvent in the state-of-the-art free energy method is problematic, and further investigations of the solvent effect on the OER are necessary before the findings presented here can be generalized. The second category is associated with the endeavors to break the linear scaling relationship. The detailed reaction mechanism under realistic conditions is still a matter of discussion even in the case of well studied materials. In the case of the bifunctional mechanism, we presented several promising configurations that can be closely investigated in the future. Likewise, the dynamics of protons and charge carriers throughout the bifunctional reaction pathway are of interest. Finally, while polaronic defects were found to affect the OER free energies within the adopted computational schemes, their multifarious their multifarious role in the actual water splitting process certainly deserves further attention.

Bibliography

(1) BP, *BP Statistical Review of World Energy*, 2019.

(2) Dai, A. *Wiley Interdiscip. Rev. Clim. Change* **2011**, *2*, 45–65.

(3) James, R.; Washington, R. *Clim. Change* **2013**, *117*, 859–872.

(4) Mendelsohn, R.; Dinar, A.; Williams, L. *Environ Dev Econ.* **2006**, *11*, 159–178.

(5) Directive 2009/28/EC of the European Parliament and of the Council of 23 April 2009 on the promotion of the use of energy from renewable sources and amending and subsequently repealing Directives 2001/77/EC and 2003/30/EC (Text with EEA relevance)., en, Code Number: 140 Library Catalog: EUR-Lex, 2009.

(6) EUR-Lex - 52011PC0809 - EN - EUR-Lex.

(7) Agency, I. E., *World Energy Balances 2019*, 2019.

(8) Nielson, E. G.; Goodman, D. *Reuters* **2018**.

(9) McDonald, J. *The Independent* **2017**.

(10) Sheridan, D. *The Telegraph* **2020**.

(11) Solomon, S. *The Times of Israel* **2018**.

(12) Moriarty, P.; Honnery, D. *Int. J. Hydrog. Energy* **2019**, *44*, 16029–16037.

(13) Ausfelder, F.; Bazzanella, A. *Hydrogen Science and Engineering : Materials, Processes, Systems and Technology* **2016**, 19–40.

(14) Holladay, J.; Hu, J.; King, D.; Wang, Y. *Catal.* **2009**, *139*, Hydrogen Production - Selected papers from the Hydrogen Production Symposium at the American Chemical Society 234th National Meeting & Exposition, August 19-23, 2007, Boston, MA, USA, 244–260.

(15) Seh, Z. W.; Kibsgaard, J.; Dickens, C. F.; Chorkendorff, I.; Nørskov, J. K.; Jaramillo, T. F. *Science* **2017**, *355*, eaad4998.

(16) McCrory, C. C. L.; Jung, S.; Peters, J. C.; Jaramillo, T. F. *J. Am. Chem. Soc.* **2013**, *135*, 16977–16987.

(17) Walter, M. G.; Warren, E. L.; McKone, J. R.; Boettcher, S. W.; Mi, Q.; Santori, E. A.; Lewis, N. S. *Chem. Rev.* **2010**, *110*, 6446–6473.

(18) Tentu, R. D.; Basu, S. *Curr. Opin. Electrochem.* **2017**, *5*, 56–62.

(19) Suen, N.-T.; Hung, S.-F.; Quan, Q.; Zhang, N.; Xu, Y.-J.; Ming Chen, H. *Chem. Soc. Rev.* **2017**, *46*, 337–365.

(20) Montoya, J. H.; Seitz, L. C.; Chakthranont, P.; Vojvodic, A.; Jaramillo, T. F.; Nørskov, J. K. *Nature* **2017**, *16*, 70–81.

(21) Maeda, K.; Domen, K. *J. Phys. Chem. C* **2007**, *111*, 7851–7861.

(22) Maeda, K.; Domen, K. *Chem. Lett.* **2010**, *1*, 2655–2661.

(23) Man, I. C.; Su, H.-Y.; Calle-Vallejo, F.; Hansen, H. A.; Martínez, J. I.; Inoglu, N. G.; Kitchin, J.; Jaramillo, T. F.; Nørskov, J. K.; Rossmeisl, J. *ChemCatChem* **2011**, *3*, 1159–1165.

(24) Rossmeisl, J.; Qu, Z.-W.; Zhu, H.; Kroes, G.-J.; Nørskov, J. *J. Electroanal. Chem.* **2007**, *607*, 83–89.

(25) Oberhofer, H. In *Handbook of Materials Modeling: Applications: Current and Emerging Materials*, Andreoni, W., Yip, S., Eds.; Springer International Publishing: Cham, 2018, pp 1–33.

(26) Lu, F.; Zhou, M.; Zhou, Y.; Zeng, X. *Small* **2017**, *13*, 1701931.

(27) Bligaard, T.; Nørskov, J. K.; Dahl, S.; Matthiesen, J.; Christensen, C. H.; Sehested, J. *J. Catal* **2004**, *224*, 206–217.

(28) Koper, M. T. M. *J. Electroanal. Chem.* **2011**, *660*, 254–260.

(29) Ramakrishnan, P.; Im, H.; Baek, S.-H.; Sohn, J. I. *Isr. J. Chem.* **2019**, *59*, 708–719.

(30) Viswanathan, V.; Hansen, H. A.; Rossmeisl, J.; Nørskov, J. K. *ACS Catal.* **2012**, *2*, 1654–1660.

(31) Nørskov, J. K.; Rossmeisl, J.; Logadottir, A.; Lindqvist, L.; Kitchin, J. R.; Bligaard, T.; Jónsson, H. *J. Phys. Chem.* **2004**, *108*, 17886–17892.

(32) Christensen, R.; Hansen, H. A.; Dickens, C. F.; Nørskov, J. K.; Vegge, T. *J. Phys. Chem.* **2016**, *120*, 24910–24916.

(33) Valdés, Á.; Qu, Z.-W.; Kroes, G.-J.; Rossmeisl, J.; Nørskov, J. K. *J. Phys. Chem.* **2008**, *112*, 9872–9879.

(34) A. Peterson, A.; Abild-Pedersen, F.; Studt, F.; Rossmeisl, J.; K. Nørskov, J. *Energy Environ. Sci.* **2010**, *3*, 1311–1315.

(35) Sha, Y.; Yu, T. H.; Liu, Y.; Merinov, B. V.; Goddard, W. A. *J. Phys. Chem. Lett.* **2010**, *1*, 856–861.

(36) Li, Y.-F.; Liu, Z.-P.; Liu, L.; Gao, W. *J. Am. Chem. Soc.* **2010**, *132*, 13008–13015.

(37) Fortunelli, A.; Iii, W. A. G.; Sementa, L.; Barcaro, G. *Nanoscale* **2015**, *7*, 4514–4521.

(38) Ping, Y.; Nielsen, R. J.; Goddard, W. A. *J. Am. Chem. Soc.* **2017**, *139*, 149–155.

(39) Skúlason, E.; Karlberg, G. S.; Rossmeisl, J.; Bligaard, T.; Greeley, J.; Jónsson, H.; Nørskov, J. K. *Phys. Chem. Chem. Phys.* **2007**, *9*, 3241–3250.

(40) Skúlason, E.; Tripkovic, V.; Björketun, M. E.; Gudmundsdóttir, S.; Karlberg, G.; Rossmeisl, J.; Bligaard, T.; Jónsson, H.; Nørskov, J. K. *J. Phys. Chem. C* **2010**, *114*, 18182–18197.

(41) Gauthier, J. A.; Dickens, C. F.; Chen, L. D.; Doyle, A. D.; Nørskov, J. K. *J. Phys. Chem.* **2017**, *121*, 11455–11463.

(42) Hansen, M. H.; Rossmeisl, J. *J. Phys. Chem. C* **2016**, *120*, 29135–29143.

(43) Ludwig, T.; Gauthier, J. A.; Brown, K. S.; Ringe, S.; Nørskov, J. K.; Chan, K. *J. Phys. Chem. C* **2019**, *123*, 5999–6009.

(44) Frenkel, D.; Smit, B. In *Understanding Molecular Simulation (Second Edition)*, Frenkel, D., Smit, B., Eds., Second Edition; Academic Press: San Diego, 2002, pp 167–200.

(45) Costanzo, F.; Sulpizi, M.; Valle, R. G. D.; Sprik, M. *J. Chem. Phys.* **2011**, *134*, 244508.

(46) Cheng, J.; Liu, X.; Kattirtzi, J. A.; VandeVondele, J.; Sprik, M. *Angew. Chem. Int. Ed.* **2014**, *53*, 12046–12050.

(47) Patel, A. M.; Ringe, S.; Siahrostami, S.; Bajdich, M.; Nørskov, J. K.; Kulkarni, A. R. *J. Phys. Chem. C* **2018**, *122*, 29307–29318.

(48) Ambrosio, F.; Wiktor, J.; Pasquarello, A. *ACS Appl. Mater. Interfaces* **2018**, *10*, 10011–10021.

(49) Oberhofer, H.; Reuter, K. *Chem. Phys.* **2013**, *139*, 044710.

(50) Gono, P.; Pasquarello, A. *J. Chem. Phys.* **2020**, *152*, 104712.

(51) Cheng, J.; Sulpizi, M.; VandeVondele, J.; Sprik, M. *ChemCatChem* **2012**, *4*, 636–640.

(52) Ji, Y.; Wang, B.; Luo, Y. *J. Phys. Chem.* **2012**, *116*, 7863–7866.

(53) Varley, J. B.; Janotti, A.; Franchini, C.; Van de Walle, C. G. *Phys. Rev. B* **2012**, *85*, 081109.

(54) Salvador, P. *J. Phys. Chem.* **2007**, *111*, 17038–17043.

(55) Wang, D.; Wang, H.; Hu, P. *Chem. Phys.* **2015**, *17*, 1549–1555.

(56) Gono, P.; Wiktor, J.; Ambrosio, F.; Pasquarello, A. *ACS Catal.* **2018**, *8*, 5847–5851.

(57) Ambrosio, F.; Wiktor, J. *J. Phys. Chem. Lett.* **2019**, *10*, 7113–7118.

(58) Wiktor, J.; Ambrosio, F.; Pasquarello, A. *ACS Energy Lett.* **2018**, *3*, 1693–1697.

(59) Wiktor, J.; Pasquarello, A. *ACS Appl. Mater. Interfaces* **2019**, *11*, 18423–18426.

(60) Cen, J.; Li, S.; Zheng, J.; Pan, F. *RSC Advances* **2019**, *9*, 819–823.

(61) Di Valentin, C.; Selloni, A. *Chem. Lett.* **2011**, *2*, 2223–2228.

(62) Imanishi, A.; Okamura, T.; Ohashi, N.; Nakamura, R.; Nakato, Y. *J. Am. Chem. Soc.* **2007**, *129*, 11569–11578.

(63) Valentin, C. D. *J. Phys.: Condens. Matter* **2016**, *28*, 074002.

(64) Qiu, W.; Xiao, S.; Ke, J.; Wang, Z.; Tang, S.; Zhang, K.; Qian, W.; Huang, Y.; Huang, D.; Tong, Y.; Yang, S. *Angew. Chem* **2019**, *131*, 19263–19271.

(65) Pastor, E.; Park, J.-S.; Steier, L.; Kim, S.; Grätzel, M.; Durrant, J. R.; Walsh, A.; Bakulin, A. A. *Nat Commun* **2019**, *10*, 1–7.

(66) De Lile, J. R.; Kang, S. G.; Son, Y.-A.; Lee, S. G. *ACS Omega* **2019**, *4*, 8056–8064.

(67) Shibuya, T.; Yasuoka, K.; Mirbt, S.; Sanyal, B. *J. Phys.: Condens. Matter* **2012**, *24*, 435504.

(68) Erhart, P.; Klein, A.; Åberg, D.; Sadigh, B. *Phys. Rev. B* **2014**, *90*, 035204.

(69) Huang, Z.-F.; Wang, J.; Peng, Y.; Jung, C.-Y.; Fisher, A.; Wang, X. *Adv. Energy Mater* **2017**, *7*, 1700544.

(70) Hansen, H. A.; Shi, C.; Lausche, A. C.; Peterson, A. A.; Nørskov, J. K. *Phys. Chem. Chem. Phys.* **2016**, *18*, 9194–9201.

(71) Yamada, I.; Fujii, H.; Takamatsu, A.; Ikeno, H.; Wada, K.; Tsukasaki, H.; Kawaguchi, S.; Mori, S.; Yagi, S. *Adv. Mater* **2017**, *29*, 1603004.

(72) Frydendal, R.; Busch, M.; Halck, N. B.; Paoli, E. A.; Krtil, P.; Chorkendorff, I.; Rossmeisl, J. *ChemCatChem* **2015**, *7*, 149–154.

(73) Bendtsen Halck, N.; Petrykin, V.; Krtil, P.; Rossmeisl, J. *Phys. Chem. Chem. Phys.* **2014**, *16*, 13682–13688.

(74) Busch, M.; Halck, N. B.; Kramm, U. I.; Siahrostami, S.; Krtil, P.; Rossmeisl, J. *Nano Energy* **2016**, *29*, 126–135.

(75) Fan, K.; Ji, Y.; Zou, H.; Zhang, J.; Zhu, B.; Chen, H.; Daniel, Q.; Luo, Y.; Yu, J.; Sun, L. *Angew. Chem. Int. Ed.* **2017**, *56*, 3289–3293.

(76) Song, F.; Busch, M. M.; Lassalle-Kaiser, B.; Hsu, C.-S.; Petkucheva, E.; Bensimon, M.; Chen, H. M.; Corminboeuf, C.; Hu, X. *ACS Cent. Sci.* **2019**, *5*, 558–568.

(77) Hutter, J.; Iannuzzi, M.; Schiffmann, F.; VandeVondele, J. *Science* **2014**, *4*, 15–25.

(78) Hohenberg, P.; Kohn, W. *Phys. Rev.* **1964**, *136*, B864–B871.

(79) Perdew, J. P.; Wang, Y. *Phys. Rev. B* **1992**, *45*, 13244–13249.

(80) Perdew, J. P.; Zunger, A. *Phys. Rev. B* **1981**, *23*, 5048–5079.

(81) Cole, L. A.; Perdew, J. P. *Phys. Rev. A* **1982**, *25*, 1265–1271.

(82) Vosko, S. H.; Wilk, L.; Nusair, M. *Can. J. Phys.* **1980**, *58*, 1200–1211.

(83) Perdew, J. P.; Yue, W. *Phys. Rev. B* **1986**, *33*, 8800–8802.

(84) Perdew, J. P.; Burke, K.; Ernzerhof, M. *Phys. Rev. Lett.* **1996**, *77*, 3865–3868.

(85) Patton, D. C.; Porezag, D. V.; Pederson, M. R. *Phys. Rev. B* **1997**, *55*, 7454–7459.

(86) Hammer, B.; Hansen, L. B.; Nørskov, J. K. *Phys. Rev. B* **1999**, *59*, 7413–7421.

(87) Becke, A. D. *J. Chem. Phys.* **1993**, *98*, 1372–1377.

(88) Perdew, J. P.; Ernzerhof, M.; Burke, K. *J. Chem. Phys.* **1996**, *105*, 9982–9985.

(89) Adamo, C.; Barone, V. *Chem. Phys.* **1999**, *110*, 6158–6170.

(90) Heyd, J.; Scuseria, G. E.; Ernzerhof, M. *J. Chem. Phys.* **2003**, *118*, 8207–8215.

(91) VandeVondele, J.; Krack, M.; Mohamed, F.; Parrinello, M.; Chassaing, T.; Hutter, J. *Comput. Phys. Commun* **2005**, *167*, 103–128.

(92) VandeVondele, J.; Iannuzzi, M.; Hutter, J. In *Computer Simulations in Condensed Matter Systems: From Materials to Chemical Biology Volume 1*, Ferrario, M., Ciccotti, G., Binder, K., Eds.; Lecture Notes in Physics; Springer: Berlin, Heidelberg, 2006, pp 287–314.

(93) VandeVondele, J.; Hutter, J. *Chem. Phys.* **2007**, *127*, 114105.

(94) Guidon, M.; Hutter, J.; VandeVondele, J. *J. Chem. Theory Comput.* **2009**, *5*, 3010–3021.

(95) Ernzerhof, M.; Perdew, J. P. *J. Chem. Phys.* **1998**, *109*, 3313–3320.

(96) Heyd, J.; Peralta, J. E.; Scuseria, G. E.; Martin, R. L. *Chem. Phys.* **2005**, *123*, 174101.

(97) Guidon, M.; Hutter, J.; VandeVondele, J. *J. Chem. Theory Comput.* **2010**, *6*, 2348–2364.

(98) Fletcher, R. In *Practical Methods of Optimization*; John Wiley & Sons, Ltd: 2013, pp 44–79.

(99) Pfrommer, B. G.; Côté, M.; Louie, S. G.; Cohen, M. L. *J. Comput. Phys* **1997**, *131*, 233–240.

(100) Grotendorst, J., *Modern methods and algorithms of quantum chemistry: Winterschool, 21-25 February 2000, Forschungszentrum Jülich, Germany: proceedings*; NIC series 1; John von Neumann Inst. for Computing: Jülich, 2000.

(101) Tuckerman, M. E.; Parrinello, M. *J. Chem. Phys.* **1994**, *101*, 1302–1315.

(102) Hoover, W. G. *Phys. Rev. A* **1985**, *31*, 1695–1697.

(103) Martyna, G. J.; Klein, M. L.; Tuckerman, M. *J. Chem. Phys.* **1992**, *97*, 2635–2643.

(104) Blumberger, J.; Tavernelli, I.; Klein, M. L.; Sprik, M. *J. Chem. Phys.* **2006**, *124*, 064507.

(105) Wereszczynski, J.; McCammon, J. A. *Q Rev Biophys* **2012**, *45*, 1–25.

(106) Kirkwood, J. G. *J. Chem. Phys.* **1935**, *3*, 300–313.

(107) Cheng, J.; Sulpizi, M.; Sprik, M. *J. Chem. Phys.* **2009**, *131*, 154504.

(108) Carter, E. A.; Ciccotti, G.; Hynes, J. T.; Kapral, R. *Chem. Phys. Lett* **1989**, *156*, 472–477.

(109) Ciccotti, G.; Ferrario, M. *J. Mol. Liq.* **2000**, *89*, 1–18.

(110) Sprik, M.; Ciccotti, G. *Chem. Phys.* **1998**, *109*, 7737–7744.

(111) Ryckaert, J.-P.; Ciccotti, G.; Berendsen, H. J. C. *J. Comput. Phys* **1977**, *23*, 327–341.

(112) Bouzid, A.; Gono, P.; Pasquarello, A. *J. Catal* **2019**, *375*, 135–139.

(113) Fujii, K. In *Solar to Chemical Energy Conversion: Theory and Application*, Sugiyama, M., Fujii, K., Nakamura, S., Eds.; Springer International Publishing: Cham, 2016, pp 7–34.

(114) Bard, A. J.; Faulkner, L. R., *Electrochemical Methods: Fundamentals and Applications*, 2nd ed.; Wiley: 2000.

(115) Jones, G.; Jakobsen, J. G.; Shim, S. S.; Kleis, J.; Andersson, M. P.; Rossmeisl, J.; Abild-Pedersen, F.; Bligaard, T.; Helveg, S.; Hinnemann, B.; Rostrup-Nielsen, J. R.; Chorkendorff, I.; Sehested, J.; Nørskov, J. K. *J. Catal.* **2008**, *259*, 147–160.

(116) Cramer, C. J., *Essentials of Computational Chemistry: Theories and Models*, 2nd ed.; Wiley, Chichester: 2004, pp 355–366.

(117) Giordano, L.; Han, B.; Risch, M.; Hong, W. T.; Rao, R. R.; Stoerzinger, K. A.; Shao-Horn, Y. *Catal. Today* **2016**, *262*, 2–10.

(118) Guo, Z.; Ambrosio, F.; Chen, W.; Gono, P.; Pasquarello, A. *Chem. Mater.* **2018**, *30*, 94–111.

(119) Li, Y.-H.; Gong, X. G.; Wei, S.-H. *Phys. Rev. B* **2006**, *73*, 245206.

(120) Goedecker, S.; Teter, M.; Hutter, J. *Phys. Rev. B* **1996**, *54*, 1703–1710.

(121) Hu, J.; Zhao, X.; Chen, W.; Su, H.; Chen, Z. *J. Phys. Chem. C* **2017**, *121*, 18702–18709.

(122) Krukau, A. V.; Vydrov, O. A.; Izmaylov, A. F.; Scuseria, G. E. *J. Chem. Phys.* **2006**, *125*, 224106.

(123) Santos, E. J. G.; Nørskov, J. K.; Vojvodic, A. *J. Phys. Chem. C* **2015**, *119*, 17662–17666.

(124) Vydrov, O. A.; Van Voorhis, T. *J. Chem. Phys.* **2010**, *133*, 244103.

(125) Sabatini, R.; Gorni, T.; de Gironcoli, S. *Phys. Rev. B* **2013**, *87*, 041108.

(126) Miceli, G.; de Gironcoli, S.; Pasquarello, A. *Chem. Phys.* **2015**, *142*, 034501.

(127) Nozik, A. J. *Nature* **1975**, *257*, 383–386.

(128) Li, Y.-F.; Selloni, A. *ACS Catal.* **2016**, *6*, 4769–4774.

(129) Balajka, J.; Aschauer, U.; Mertens, S. F. L.; Selloni, A.; Schmid, M.; Diebold, U. *J. Phys. Chem. C* **2017**, *121*, 26424–26431.

(130) Bandura, A. V.; Sykes, D. G.; Shapovalov, V.; Troung, T. N.; Kubicki, J. D.; Evarestov, R. A. *J. Phys. Chem. B* **2004**, *108*, 7844–7853.

(131) Berardo, E.; Zwijnenburg, M. A. *J. Phys. Chem. C* **2015**, *119*, 13384–13393.

(132) Cheng, J.; Sprik, M. *J. Chem. Theory Comput.* **2010**, *6*, 880–889.

(133) Cheng, J.; Sprik, M. *J. Phys. Condens. Matter* **2014**, *26*, 244108.

(134) Shirai, K.; Fazio, G.; Sugimoto, T.; Selli, D.; Ferraro, L.; Watanabe, K.; Haruta, M.; Ohtani, B.; Kurata, H.; Di Valentin, C.; Matsumoto, Y. *J. Am. Chem. Soc.* **2018**, *140*, PMID: 29325412, 1415–1422.

(135) Fazio, G.; Selli, D.; Ferraro, L.; Seifert, G.; Di Valentin, C. *ACS Appl. Mater. Interfaces* **2018**, *10*, PMID: 29950088, 29943–29953.

(136) Zheng, T.; Wu, C.; Chen, M.; Zhang, Y.; Cummings, P. T. *J. Chem. Phys.* **2016**, *145*, 044702.

(137) Gono, P.; Ambrosio, F.; Pasquarello, A. *J. Phys. Chem. C* **2019**, *123*, 18467–18474.

(138) Del Ben, M.; Hutter, J.; VandeVondele, J. *J. Chem. Theory Comput.* **2012**, *8*, 4177–4188.

(139) Del Ben, M.; Hutter, J.; VandeVondele, J. *J. Chem. Phys.* **2015**, *143*, 054506.

(140) VandeVondele, J.; Mohamed, F.; Krack, M.; Hutter, J.; Sprik, M.; Parrinello, M. *Chem. Phys.* **2004**, *122*, 014515.

(141) Cheng, J.; Sprik, M. *Phys. Chem. Chem. Phys.* **2012**, *14*, 11245–11267.

(142) Ambrosio, F.; Miceli, G.; Pasquarello, A. *Chem. Phys.* **2015**, *143*, 244508.

(143) Flyvbjerg, H. In *Advances in Computer Simulation*, 1st ed.; Lect. Notes Phys. Vol. 501; Springer, Berlin, Heidelberg: 1998, pp 88–103.

(144) Soper, A. K.; Bruni, F.; Ricci, M. A. *J. Chem. Phys.* **1997**, *106*, 247–254.

(145) Komsa, H.-P.; Pasquarello, A. *Phys. Rev. Lett.* **2013**, *110*, 095505.

(146) Dau, H.; Limberg, C.; Reier, T.; Risch, M.; Roggan, S.; Strasser, P. *ChemCatChem* **2010**, *2*, 724–761.

(147) Zaffran, J.; Toroker, M. C. *ChemElectroChem* **2018**, *4*, 2764–2770.

(148) Fidelsky, V.; Toroker, M. C. *Phys. Chem. Chem. Phys.* **2017**, *19*, 7491–7497.

(149) García-Mota, M.; Vojvodic, A.; Metiu, H.; Man, I. C.; Su, H.-Y.; Rossmeisl, J.; Nørskov, J. K. *ChemCatChem* **2011**, *3*, 1607–1611.

(150) Wu, X.-P.; Gong, X.-Q. *J. Am. Chem. Soc.* **2015**, *137*, 13228–13231.

(151) Klein, A.; Körber, C.; Wachau, A.; Säuberlich, F.; Gassenbauer, Y.; Schafranek, R.; Harvey, S. P.; Mason, T. O. *Thin Solid Films* **2009**, *518*, 1197–1203.

(152) Jarzebski, Z. M.; Morton, J. P. *J. Electrochem. Soc.* **1976**, *123*, 333C–346C.

(153) Reimann, K.; Steube, M. *Solid State Commun.* **1998**, *105*, 649–652.

(154) Böttcher, A.; Niehus, H. *Phys. Rev. B* **1999**, *60*, 14396–14404.

(155) Schierbaum, K. D.; Fischer, S.; Torquemada, M. C.; de Segovia, J. L.; Román, E.; Martín-Gago, J. A. *Surf. Sci.* **1996**, *345*, 261–273.

(156) Tang, H.; Prasad, K.; Sanjinès, R.; Schmid, P. E.; Lévy, F. *J. Appl. Phys.* **1994**, *75*, 2042–2047.

(157) Crespo-Otero, R.; Walsh, A. *J. Phys. Chem. Lett.* **2015**, *6*, 2379–2383.

(158) Cooper, J. K.; Gul, S.; Toma, F. M.; Chen, L.; Glans, P.-A.; Guo, J.; Ager, J. W.; Yano, J.; Sharp, I. D. *Chem. Mater.* **2014**, *26*, 5365–5373.

(159) Gong, M.; Dai, H. *Nano Res.* **2015**, *8*, 23–39.

(160) Conesa, J. C. *J. Phys. Chem. C* **2016**, *120*, 18999–19010.

(161) Zaffran, J.; Caspary Toroker, M. *J. Chem. Theory Comput.* **2016**, *12*, 3807–3812.

(162) Zaffran, J.; Toroker, M. C. *ChemPhysChem* **2016**, *17*, 1630–1636.

(163) Huang, Z.; Han, F.; Li, M.; Zhou, Z.; Guan, X.; Guo, L. *Comput. Mater. Sci* **2019**, *169*, 109110.

(164) Munshi, M. Z. A.; Tseung, A. C. C.; Parker, J. *J. Appl. Electrochem.* **1985**, *15*, 711–717.

(165) Tichenor, R. L. *Ind. Eng. Chem.* **1952**, *44*, 973–977.

(166) Corrigan, D. A. *J. Electrochem. Soc.* **1987**, *134*, 377.

(167) Trotochaud, L.; Ranney, J. K.; Williams, K. N.; Boettcher, S. W. *J. Am. Chem. Soc.* **2012**, *134*, 17253–17261.

(168) Trotochaud, L.; Young, S. L.; Ranney, J. K.; Boettcher, S. W. *J. Am. Chem. Soc.* **2014**, *136*, 6744–6753.

(169) Bode, H.; Dehmelt, K.; Witte, J. *Electrochim. Acta* **1966**, *11*, 1079–1087.

(170) Hunter, B. M.; Winkler, J. R.; Gray, H. B. *Molecules* **2018**, *23*, 903.

(171) Kim, J.; Li, W.; L. Philips, B.; P. Grey, C. *Energy Environ. Sci* **2011**, *4*, 4298–4305.

(172) Tang, M.; Ge, Q. *Chinese J. Catal.* **2017**, *38*, 1621–1628.

(173) Oesten, R.; Wohlfahrt-Mehrens, M.; Ströbele, S.; Kasper, M.; Huggins, R. A. *Ionics* **1996**, *2*, 293–301.

(174) Li, Y.-F.; Selloni, A. *ACS Catal.* **2014**, *4*, 1148–1153.

(175) Nørskov, J. K.; Bligaard, T.; Logadottir, A.; Bahn, S.; Hansen, L. B.; Bollinger, M.; Bengaard, H.; Hammer, B.; Sljivancanin, Z.; Mavrikakis, M.; Xu, Y.; Dahl, S.; Jacobsen, C. J. H. *J. Catal.* **2002**, *209*, 275–278.

(176) Yang, S.; Brant, A. T.; Giles, N. C.; Halliburton, L. E. *Phys. Rev. B* **2013**, *87*, 125201.

(177) Morgan, B. J.; Watson, G. W. *Phys. Rev. B* **2009**, *80*, 233102.

(178) Di Valentin, C.; Pacchioni, G.; Selloni, A. *Phys. Rev. Lett.* **2006**, *97*, 166803.

(179) Ji, Y.; Wang, B.; Luo, Y. *J. Phys. Chem. C* **2014**, *118*, 1027–1034.

(180) Mom, R. V.; Cheng, J.; Koper, M. T. M.; Sprik, M. *J. Phys. Chem.* **2014**, *118*, 4095–4102.

(181) Spreafico, C.; VandeVondele, J. *Chem. Phys.* **2014**, *16*, 26144–26152.

(182) Kavan, L.; Grätzel, M.; Gilbert, S. E.; Klemenz, C.; Scheel, H. J. *J. Am. Chem. Soc.* **1996**, *118*, 6716–6723.

(183) Tezuka, Y.; Shin, S.; Ishii, T.; Ejima, T.; Suzuki, S.; Sato, S. *J. Phys. Soc. Jpn.* **1994**, *63*, 347–357.

(184) Miceli, G.; Chen, W.; Reshetnyak, I.; Pasquarello, A. *Phys. Rev. B* **2018**, *97*, 121112.

(185) Chen, S.; Wang, L.-W. *Phys. Rev. B* **2014**, *89*, 014109.

(186) Århammar, C. et al. *Proc. Natl. Acad. Sci.* **2011**, *108*, 6355–6360.

(187) Guo, Z.; Ambrosio, F.; Pasquarello, A. *Appl. Phys. Lett.* **2016**, *109*, 062903.

(188) Hörmann, N. G.; Guo, Z.; Ambrosio, F.; Andreussi, O.; Pasquarello, A.; Marzari, N. *Npj Comput. Mater.* **2019**, *5*, 1–6.

(189) Nakamura, R.; Ohashi, N.; Imanishi, A.; Osawa, T.; Matsumoto, Y.; Koinuma, H.; Nakato, Y. *J. Phys. Chem. B* **2005**, *109*, 1648–1651.

(190) Matsumoto, Y.; Yoshikawa, T.; Sato, E.-i. *J. Electrochem. Soc.* **1989**, *136*, 1389.

(191) Komsa, H.-P.; Rantala, T. T.; Pasquarello, A. *Phys. Rev. B* **2012**, *86*, 045112.

(192) Freysoldt, C.; Grabowski, B.; Hickel, T.; Neugebauer, J.; Kresse, G.; Janotti, A.; Van de Walle, C. G. *Rev. Mod. Phys.* **2014**, *86*, 253–305.

(193) Traylor, J. G.; Smith, H. G.; Nicklow, R. M.; Wilkinson, M. K. *Phys. Rev. B* **1971**, *3*, 3457–3472.

(194) Berberich, L. J.; Bell, M. E. *J. Appl. Phys.* **1940**, *11*, 681–692.

(195) Busani, T.; Devine, R. A. B. *Semicond. Sci. Technol.* **2005**, *20*, 870–875.

(196) Uematsu, M.; Frank, E. U. *J. Phys. Chem. Ref. Data* **1980**, *9*, 1291–1306.

Patrick Gono

Personal Information

Date of Birth: 31/08/1993
Place of Birth: Lucenec, Slovakia
Nationality: Slovak

Education

PhD: Ecole Polytechnique Fédérale de Lausanne 2016 – 2020
Physics
Lausanne, Switzerland

MSc: Masaryk University 2014 – 2016
Condensed Matter Physics
Brno, Czechia

List of Publications

Z. Guo, F. Ambrosio, W. Chen, P. Gono, A. Pasquarello
Alignment of redox levels at semiconductor–water interfaces
Chemistry of Materials **30** (1), 94-111, (2018)
https://doi.org/10.1021/acs.chemmater.7b02619

P. Gono, J. Wiktor, F. Ambrosio, A. Pasquarello
Surface polarons reducing overpotentials in the oxygen evolution reaction
ACS Catalysis **8** (7), 5847-5851, (2018)
https://doi.org/10.1021/acscatal.8b01120

P. Gono, F. Ambrosio, A. Pasquarello
Effect of the Solvent on the Oxygen Evolution Reaction at the TiO2–Water Interface
The Journal of Physical Chemistry C **123** (30), 18467-18474, (2019)
https://doi.org/10.1021/acs.jpcc.9b05015

A. Bouzid, P. Gono, A. Pasquarello
Reaction pathway of oxygen evolution on Pt (1 1 1) revealed through constant Fermi level molecular dynamics
Journal of catalysis **375**, 135-139, (2019)
https://doi.org/10.1016/j.jcat.2019.05.025

P. Gono, A. Pasquarello
Oxygen evolution reaction: Bifunctional mechanism breaking the linear scaling relationship
The Journal of Chemical Physics **152** (10), 104712, (2020)
https://doi.org/10.1063/1.5143235